Precipitation, gelation and mechanical properties of Calcium- Silicate-Hydrate gels

Aikaterini Ioannidou

Precipitation, gelation and mechanical properties of Calcium-Silicate-Hydrate gels

Author(s):
Ioannidou, Aikaterini

Publication Date:
2014

Permanent Link:

https://doi.org/10.3929/ethz-a-010223054 →

Defense Date:
25 February 2014

Diss. ETH No. 21801

Precipitation, gelation and mechanical properties of Calcium-Silicate-Hydrate gels

A dissertation submitted to
ETH Zurich

for the degree of
Doctor of Sciences

presented by
Aikaterini Ioannidou
MSc in Theoretical Physics, Utrecht University
born 6.5.1985
citizen of Greece

accepted on the recommendation of
Prof. Dr. E. Del Gado, ETH Zürich, examiner
Prof. Dr. R. Flatt, ETH Zürich, co-examiner
Prof. Dr. H. Van Damme, co-examiner

2014

Summary

The way materials form in real conditions influences their function and performance. A material such as cement is an example of how the environmental and chemical conditions determine its structure and mechanics. Cement is not only a complex material, challenging to study, but also of huge importance for civil engineering. In this thesis, I have investigated the development of calcium-silicate-hydrate (C-S-H) gels under out-of-equilibrium conditions, which form during cement hydration and are the main responsible for cement mechanical strength. I have proposed a new model and numerical approach, based on soft matter, to follow the gel formation upon precipitation and aggregation of nano-scale hydration products. This enabled me to systematically connect the formation protocol to the material microstructure and mechanics at all stages. In particular, I use Grand Canonical Monte Carlo to mimic precipitation events during Molecular Dynamics simulations, with their rate corresponding to the hydrate production rate set by the chemical environment. The particle effective interactions are consistent with forces measured between the nano-scale hydrates in experiments at fixed lime concentrations. I have explored the influence of the out-of-equilibrium aggregation to the C-S-H densification and mechanics by analyzing the microstructure morphology and local packing. Moreover, I studied the equilibrium phases and metastable states of the effective interactions without precipitation in order to determine the effect of the underlying thermodynamics into the structure of C-S-H gels. Finally, I achieved a good qualitative agreement with chemical, structural and mechanical experimental data of cement.

Sommario

Funzioni e prestazioni dei materiali sono influenzate dal processo di formazione degli stessi. Il cemento rappresenta un esempio di come le condizioni ambientali e chimiche determinino meccanica e struttura dei materiali. Esso è non soltanto un materiale complesso, il cui studio presenta quindi notevole interesse e difficoltà, ma è anche di grande importanza per l'ingegneria civile. Nel presente lavoro di tesi ho studiato lo sviluppo dei gel di silicati idrati di calcio (C-S-H) in condizioni di non equilibrio. Essi si formano durante l'idratazione del cemento e sono i principali responsabili della sua resistenza meccanica. Usando un approccio proprio della fisica della materia soffice, ho proposto un nuovo modello numerico per seguire la formazione del gel per precipitazione e aggregazione di prodotti di idratazione nanoscopici. Ciò mi ha permesso di collegare sistematicamente ogni stadio di tale processo alla microstruttura e alla meccanica del materiale. In particolare, ho usato il metodo Montecarlo Gran Canonico per simulare eventi di precipitazione durante simulazioni di Dinamica Molecolare, con un tasso corrispondente a quello di produzione di idrati determinato dal particolare ambiente chimico. L'interazione efficace tra le particelle nella simulazione è consistente con quella sperimentalmente misurata tra i nano-idrati a concentrazioni di idrossido di calcio fissate. Analizzando la morfologia della microstruttura e l'impaccamento locale, ho quindi studiato come l'aggregazione fuori dall'equilibrio influenzi la densificazione e la meccanica del C-S-H. Inoltre, al fine di determinare l'effetto della loro termodinamica sulla struttura dei gel di C-H-S, ho analizzato le fasi e gli stati metastabili corrispondenti alle interazioni efficaci all'equilibrio in assenza di precipitazione. Infine, ho ottenuto proprietà chimiche, strutturali e meccaniche che sono in buon accordo con i risultati sperimentali sul cemento.

Acknowledgements

I would like to thank all the people that contributed directly or indirectly to the accomplishment of this thesis.

I wish to express my gratitude to Emanuela Del Gado for all the opportunities that generously she gave me. I was fortunate to have a supervisor who gave me the freedom to explore new ideas and taught me how to materialize them. Thank you for sharing your enthusiasm and passion for science. Discussing with you it's an inexhaustible source of inspiration and motivation. Thank you also for your prompt insightful feedback, kindness, patience and for "kicking me out of the well" whenever I got stuck.

I would like to thank my examiners Robert Flatt and Henri van Damme for accepting to be part of the committee and for their insightful comments on my thesis. In addition, I thank all my collaborators and/or co-authors for their patience, stimulating discussions and constructive feedback: Matej Kanduc, Enrico Masoero, Mathieu Bauchy, Lunna Li, Jure Dobnikar, Daan Frenkel, Pierre Levitz, Roland Pellenq, Franz Ulm, Sidney Yip, Jos Zwanikken and Rene van Roij.

Many thanks to all the people of the IfB and in particular: to the members of the micro group and officemates Konrad, Jader, Nikita, Klara and Vishwas for being patient with me whenever I was disturbing the quiet atmosphere of the office, letting the curtains open and switching off the lights. Special thanks to Jader for his scientific and graphic advices and help. To the guys of the comphys group Alessandro, Felipe, Fabrizio, Ilia, Gautam, Julian, Vitor, Roman, Trivik, Marcus, Thomas, Tobias, Miller, Nuri, Nuno, Norbert and Kornel for their good vibes, discussions, drinks and laughs. Guys, keep the spirit up and don't let the hurricanes get you down. I especially thank Norbert for his understanding, positiveness, enthusiasm, support and help during these years. A big thank you goes to Kornel for his daily IT and not only support, for not letting me RTFM and other times for forcing me to RTFM. To the PCBM group for their hospitality and for inviting us to their events. To the secretaries Carmen, Anke, Marco, Elise, Andrea for keeping things running.

My life would have been so miserable without my incredible long-standing

friends Dimitra, Sillia, Katerina, Andrea, Antoni, Alexandro, Mark, Christo and Dimitri. Thank you for the uncountable discussions, pondering over life, inspiration and continuous support.

Last but not least, I deeply thank my family Thomai, Panagioti and Anesti for giving me the freedom of choice, their unconditional support and caring and for always being there.

Katerina

Contents

Introduction

Concrete is extensively used in the modern world for infrastructure and buildings due to its mechanical performance and low price. Because of the widespread usage of concrete and the CO_2 emission associated with the nature of the material, the manufacturing process needs to be reconsidered. Ideally the concrete production should generate less CO_2 emission, while the strength and durability of concrete are maintained or further improved. The production of Portland cement, the main binder of concrete, contributes $5-7\%$ of all man made CO_2, as it represents the largest volumes of building binder material. Even small modifications in the production of cement will reduce substantially the environmental impact of concrete. The underlying scientific questions in cement, where the physics of the microstructure emerge, go far beyond concrete technology.

Cement is the main binding agent of concrete and is produced from limestone and clay, which upon high temperature processing form hard nodules (clinker phase). The clinker is then grounded in presence of calcium sulphates to give the final cement. Calcium-Silicate-Hydrate (C–S–H) is the primary hydration product of Portland cement paste, and it precipitates upon mixing it with water, as nano-scale clusters with an associated internal pore system. These form a gel, i.e. an interconnected disordered structure, which glues together the concrete and is responsible for strength development. Mechanical and viscoelastic behavior of concrete crucially depends on the C–S–H gel and on its own creep behavior due to the evolution (aging) of the local composition and morphology. It has become now clear that the design of high performance and more environmentally friendly cement demands a deeper understanding of physical processes underlying the hydration process, when the calcium-silicate-hydrate (C–S–H) gel develops, and cement sets. In fact, chemical modifications interfere with the formation of the C–S–H gel structure in a way that is not understood and this, in turn, changes also its mechanics.

The understanding of the physics that dominate the first stages of development of mechanical strength in cement, is probably the most significant step towards controlling its properties. The setting, during which the material is transformed from a liquid paste to a soft and finally hard solid, is intimately connected to the hydration process, during which the C–S–H gel is formed. The complicated

evolution with time indicates that the C–S–H gel can have very different cohesion and space filling properties, not only due to initially different chemical composition but also due to the interplay between aggregation and arrested kinetics through the hydration and setting process. The early stages have important effects on the final mechanical behaviour of the solid material but they are very poorly understood. In particular, at present there is no quantitative or qualitative investigation able to account, from the nano-scale components, for the microstructure formation and all the way up to the mechanical response of the material.

This thesis focuses on investigating the hydration and setting of cement at the nano-scale level, using statistical physics models and methods, specifically developed for amorphous materials. Investigating the microstructure formation, its evolution and the arising of mechanical strength of C–S–H hydrate gel over length scales ranging between nm and μm is crucial for the early stages of hydration and setting but is still mainly unexplored. Here, we present a new coarse-grained, particle-based model for cohesive materials, featuring nano-scale components (particles) and specific effective interactions. Moreover, we developed a new numerical approach, a combination of Monte Carlo and Molecular Dynamics numerical simulations, to mimic the precipitation of the C–S–H hydrates and study the development of the microstructure and of the mechanical strength. It is the first time that this type of approach is applied to cement hydration and setting and allow us to address questions as: how does the precipitation rate and/or the cohesive interactions of the nm particles affect the resulting micro-structure of the C–S–H gel? How does the micro-structure of C–S–H gel evolve with time? How does the elastic modulus of the C–S–H gel develop, to what extent is it controlled by the micro-structure and how does it evolves during the hydration?

In particular, our minimal model has few input parameters, such as the effective interaction, the chemical potential and the kinetic rate (which can be though as a production rate of C–S–H). The last two parameters represent the chemical environment during cement hydration and in our model control the out-of-equilibrium conditions of precipitation. The resulting C–S–H gel microstructure is not preimposed but arises from the interplay of effective interactions and chemical conditions through the use of statistical mechanics. Moreover, this approach allow us to compute directly the mechanical properties of the C–S–H gels formed in our simulations and obtain both the time evolution of their microstructure and of their mechanical properties.

This type of approach made it possible to connect the time dependence of C–S–H production to the aggregation process and in addition to investigate the influence of the underlying thermodynamically stable and metastable states to the out-of-equilibrium process of precipitation. We have shown that the evolution of the microstructure of the simulated C–S–H gels displays an accelerating and

a decelerating regime similar to the experimental observations. The former is associated to the formation of thin elongated aggregates that grow and branch or impinge into each other to create a gel, whereas the latter corresponds to the densification of the gel branches that is favored by the underlying thermodynamics. The local packing and the structure organization of the C-S-H particles under precipitation are intimately linked to the equilibrium phase dictated by the effective interactions and by the kinetically arrested states. For this reason, we have also studied systematically the different effective interactions without precipitation and identified their impact in the structure and mechanics of the C-S-H gels under precipitation. Finally, we have been able to compare our results for the evolution of microstructure and mechanics to different experiments. The comparison allow us to rationalize a few aspects of the physics of C–S–H gels and opens new interesting questions.

The thesis is organized as follows. In Chapter 1, we give a brief overview on the main concepts in concrete and cement research that are of interest here. This overview focuses on the coupling of cement hydration with the development and evolution of the microstucture and mechanics of C–S–H gel. In Chapter 2, we briefly describe the phenomenology of colloidal gels, starting from the effective interactions and the equilibrium phases underlying the gelation mechanisms and the kinetically arrested states. These two first chapters provide the background for the soft matter perspective that we used to develop our model for growth of C–S–H gels under precipitation. In Chapter 3, we present our model for C–S–H gel formation during the early stages of cement hydration and we discuss the main results of the hydrate precipitation curves, the evolution of the gel morphology and the local packing. We explore further the underlying equilibrium phases and kinetically arrested states with respect to the effective interactions used in our model in Chapter 4, where we analyze this class of interaction potentials on a more general ground. We provide the phase diagrams and discuss how the morphology of the gels changes upon changing the competing attractive and repulsive interactions. In Chapter 5, we attempt a qualitative and quantitative comparison of the model gels with experiments on C–S–H by computing the pore size distribution, the scattering intensity, the evolution of the shear modulus and the nanoindentation modulus. Finally, we summarize the main results and give an outlook for possible future expansions of this work.

Chapter 1

From concrete and cement to calcium-silicate-hydrate gels

Concrete is the most used manufactured material as it is the cheapest, and has outstanding mechanical performances. Cement is the binder of concrete and C–S–H is the main hydration product of cement which acts as the glue of the material. Understanding the formation of the microstructure of C–S–H is important for controlling the micro- to macro- scale structure and mechanics of cement. In this thesis, we propose a new model and numerical approach to investigate the formation and evolution of the structure of C–S–H in the meso-scale using experimentally measured forces. In this first chapter, an overview of concrete, cement and mostly C–S–H is presented, focusing on how the hydration kinetics influence the evolution of mechanics, which is the mesoscale and subnano structure of C–S–H and what types of forces act at the nanoscale level of C–S–H.

1.1 Introduction to concrete and cement

The Romans used extensively concrete to build roads, aqueducts and temples that are still holding up remarkably well. The highlight of their construction projects is Pantheon that has the world's largest unreinforced concrete dome. However, after the end of the Roman empire, the use of concrete became rare until it was re-pioneered in the mid-18th century. In the modern world, concrete is the most used man-made material for infrastructure and buildings, as it is cheap and durable. The remarkable mechanical behavior of concrete is due to its binder, the cement and in turn cement's mechanical strength is due to Calcium-Silicate-Hydrate (C–S–H) gel [1].

Concrete is an artificial building material composed of water, a binding agent, sand and aggregates such as gravel, chunks of stone, crushed rocks and rubble. The most common binding agent is cement which mixed with aggregates and water eventually solidifies, or "sets". In the beginning the concrete mix

is workable, even fluid and easily shaped or poured into molds, and later it solidifies and hardens through a chemical process called hydration. The cement reacts with the water producing a paste that binds the aggregates together into a robust solid material. In addition to these three main components, chemical admixtures may be used to speed or slow down the hardening rate of cement, or reinforcements as steel may be included in concrete to increase its tensile strength [1].

5 billion metric tons of concrete are consumed each year in the world and these numbers are at the moment only foreseen to increase. From a point of view of natural resources, ecology and economy, it is not possible to imagine substituting concrete by any other material. Despite of the benefits of well-planned concrete usage, the colossal production of Portland cement, the main binder of concrete, has also negative environmental impact as it contributes to $5 - 7\%$ of all man-made CO_2. A more sustainable cement production, with less CO_2 emission, that is able to retain or even enhance the main properties of concrete like strength and durability is the present challenge of cement research. CO_2 production is mostly due to cement processing and to the chemical decomposition of limestone (clinkering). The forefront of research now is therefore towards devising strategies to reduce the CO_2 production within a "do more with less" strategy.

Cement is the most crucial component of concrete as it is responsible for sticking and holding together the aggregates. When cement is mixed with water it rapidly forms a gel which is initially fluid and workable but as the cement sets the gel densifies and becomes rigid, keeping the aggregates in place [2]. Cement paste continues to hydrate for many days after the initial setting. By the end of the curing period concrete achieves the desired mechanical strength. There are also cements that work in a different way and harden by reacting with CO_2 in atmosphere (non-hydraulic binders, e.g. slaked limes), but here we will deal only with hydraulic binders that harden by reacting with water, in particular Portland cement [1].

To produce cement, limestone (calcium carbonate) and clay (alumino-silicate) go through high temperature and through sintering form hard nodules of clinker. Initially, the mixture of limestone and clay is ground in a fine powder and then it is placed in a cement kiln, a type of oven that heats up to temperatures of 1450 °C. In the kiln, several processes, such as decarbonation of the limestone, production and transformation of the first calcium silicate and calcium aluminate phases and quenching, take place and finally lead to the clinker [1, 2]. The clinker is ground in presence of calcium sulphates (e.g. gypsum) into a fine powder to give the "Ordinary Portland Cement" (OPC), the most commonly used type of cement. The gypsum ($CaSO_4 \cdot 2H_2O$) has a significant effect on cement hydration as it stops the rapid reaction of calcium aluminates, preventing the early hardening.

Cement is not only the most important ingredient of concrete but also the most energetically expensive. Most of the CO_2 associated with cement manufacture is produced from decarbonation of limestone and fuel combustion. In modern cement kilns many advanced features are used to lower the fuel consumption per ton of clinker produced. Cement kilns are extremely large, complex, and polluting industrial installations, with many undesirable emissions. Even advanced and efficient kilns have large energy requirements to produce a ton of clinker and then grind it into cement [1]. The main strategies to reduce the environmental impact of cement consist in using cement in less quantity, more efficiently or in developing smart mixtures. The design of such high performance and more environmentally friendly cements demands a deeper understanding of the hydration process, because this is when the mechanical properties of cement are developed.

The hydration process begins soon after the mixing of cement with water. The clinker is rich in calcium silicates (mainly tricalcium silicate $3CaO \cdot SiO_2$) and reacts with water to form calcium-silicate-hydrate (C–S–H), calcium hydroxide and minerals (AFm and AFt phases) [2]. The hydration products can be categorized into polycrystalline, fully dense pore products (e.g. calcium hydroxide) and into amorphous products growing from the unreacted cement particles and forming a connected network (C–S–H). The amorphous C–S–H is the most abundant hydration product, accounting for the 70% of the cement paste volume and it is the most important as it is responsible for the remarkable mechanical properties of cement. More specifically, the percolation of the C–S–H gel through the clinker particles determines the rigidity threshold of cement. It is speculated that the early hydration stages of cement, when the primary C–S–H develops till it percolates through the clinker paste, have dramatic consequences on strength and durability of concrete.

1.2 Cement hydration

In Table 1.1 we summarize the main reacting and hydrated phases of cement mentioning also their name in cement chemistry notation (CCN). Please note that if there is a second name in the first column it refers to the mineral phase. The first four phases are the main reacting phases contained in clinker or non-hydrated cement with C_3S being more abundant and the lower part of the table contains the hydration products, all of which apart of C–S–H are crystalline.

1.2.1 The hydration process

The transformation of the liquid cement paste into a soft and finally hard solid, is intimately connected to the hydration of cement. During the process of hydration, a number of chemical reactions with multiple steps take place and different hydration products are formed. Cements (without admixtures) are transformed by 50% into hydrates within 24 hours and by 80% after 28 days. The hydration

Table 1.1 Nomenclature of the main reacting and product phases of cement. The last column is the cement chemistry notation (CCN).

Name	Molecular formula	CCN
Tricalcium silicate or Alite	$3CaO \cdot SiO_2$	C_3S
Dicalcium silicate or Belite	$2CaO \cdot SiO_2$	C_2S
Tricalcium aluminate or Aluminate	$3CaO \cdot Al_2O_3$	C_3A
Tricalcium alumino ferrite or Ferrite	$4CaO \cdot Al_2O_3 \cdot Fe_2O_3$	C_4AF
Calcium silicate hydrate	$(CaO)_x(SiO_2)(H_2O)y$	C–S–H
Calcium hydroxide or Portlandite	$Ca(OH)_2$	CH
Aluminate trisulfate or Ettringite	$(CaO)_6(Al_2O_3)(SO_3)_3 \cdot 32\ H_2O$	AFt
Aluminum monosulfate	$3CaO \cdot (Al, Fe)_2O_3 \cdot CaSO_4 \cdot n\ H_2O$	AFm
Hydrogarnet	$3CaO \cdot Al_2O_3 \cdot 6\ H_2O$	C_3AH_6

reactions can be described as dissolution of the reactive species contained in the clinker and precipitation of hydration products.

The reacting phases of cement are alite C_3S, belite C_2S, aluminate C_3A and ferrite C_4AF. The hydration of alite is the main reaction responsible for strength development during the first 24 hours. Alite reacts fast with water so that after 28 days 70% of it has been replaced by hydration products [2]. On the contrary belite hydrates much slower, only 30% has reacted by the end of 28 days. Tricalcium aluminate reacts very fast with water, causing flash setting which reduces the workability of cement paste and obstructs the mixing of cement with water. To avoid this retarders as gypsum is added to clinker. The main hydration products of the clinker are C–S–H and calcium hydroxide, whereas the reaction of calcium aluminate, with gypsum and water produces calcium sulphoaluminates, initially mainly ettringite.

The hydration process can be monitored by techniques ranging from conductimetry or calorimetry to nuclear magnetic resonance(NMR) and X-Ray

diffraction [2]. In Fig. 1.1, it is shown a typical curve of the heat flow evolution during C_3S hydration measured by isothermal calorimetry. From the changes of the heat curve, the hydration can be divided into four periods: the initial reaction, the slow reaction, the acceleration and the deceleration period. Sometimes a fifth period of slow on going hydration is added for times longer than one day. The initial reaction period is characterized by a first peak of heat flow followed by a period of low heat activity called slow reaction period. The heat flow increases until it reaches the maximum rate. This period is called acceleration period and the one following the maximum is the deceleration period [1, 2].

Initial reaction period. The first stage of hydration is characterized by the rapid dissolution of clinker

$$Ca_3SiO_5 + 3H_2O \rightarrow 3Ca^{2+} + 4OH^- + H_2SiO_4^{2-} \tag{1.1}$$

immediately after the wetting of the clinker powder. In calorimetry measurements, (see Fig. 1.1), a large exothermic signal is measured due to wetting and dissolution of clinker. The wet clinker releases ions such as calcium, silicate and hydroxide to the solution. From the evolution of these ion concentrations the dissolution rate of clinker can be evaluated. The dissolution rate shows an immediate decrease that coincides with the first peak of the calorimetry curve [3]. Moreover, a sharp peak in silicate concentration is also observed, which is followed by a sharp decrease due to the formation of C–S–H nuclei. On the contrary, the calcium and hydroxide concentrations increase as the C–S–H has a lower Ca/Si ratio than the clinker. The pH of the solution increases due to the continuous release of calcium and hydroxide. In addition, ettringite crystals appear due to the dissolution of C_3A but portlandite does not precipitate in this stage because the solution is not supersaturated with calcium and hydroxide. Overall, the hydration process shows complex coupling of the chemical reactions and the growth of different crystalline phases.

Period of slow reaction. At the next stage the reactions slow down and the cement paste retains its workability for few hours. There are different hypothesis for what is happening during this period. One is that a metastable layer of precipitates (C–S–H or C–S–H like) is formed around the clinker grains and inhibits further dissolution [3, 4]. However, such a layer has never been observed by direct surface examination, whereas experiments have detected clumps of precipitates on smooth or pitted surface of C_3S [3, 5]. Another hypothesis proposes a steady state between slow dissolution of clinker and slow grow of C–S–H [3, 4]. Some experiments also support this hypothesis showing that by addition of C–S–H seeds the slow reaction period can be nearly eliminated and the system proceeds immediately to the accelerating period [6, 7]. The larger the number of C–S–H

nuclei or seeds the faster the hydration reaction proceeds.

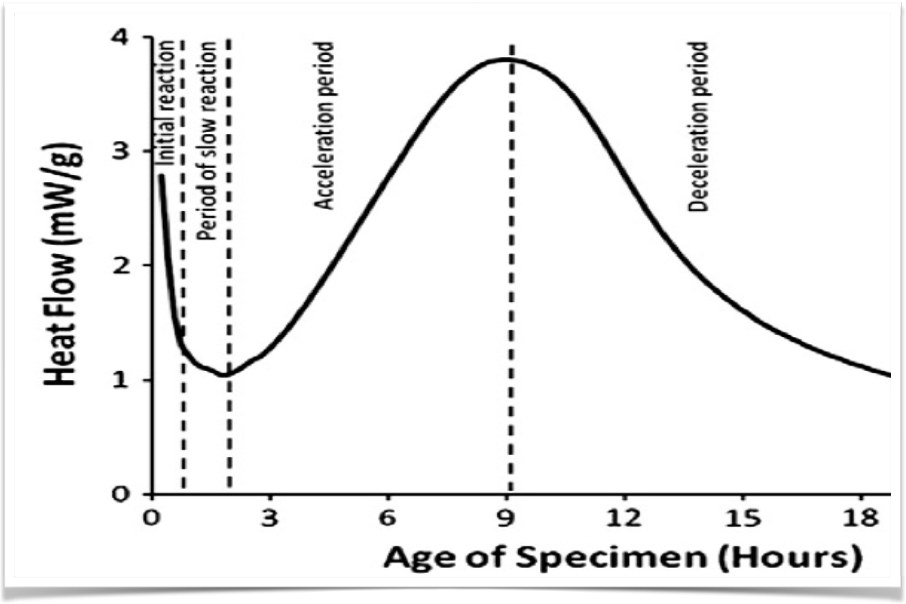

Fig. 1.1 Heat flow of alite hydration versus the hydration time of the specimen, measured by isothermal calorimetry. The characteristic periods of hydration are indicated.

Acceleration period. After the initial dissolution of clinker leads to a supersaturated solution with respect to the C–S–H and to a sufficient amount of C–S–H nuclei, fast precipitation of C–S–H occurs at the onset of the acceleration period:

$$xCa^{2+} + 2(x-1)OH^- + H_2SiO_4^{2-} \rightarrow (CaO)_x(SiO_2)(H_2O)y \qquad (1.2)$$

where x is the calcium to silicon ratio and y can vary. Reaction 1.2 shows that the stoichiometry of C–S–H is not fixed. The second hydration product is calcium hydroxide (portlandite) which precipitates according to the follow reaction:

$$Ca^{2+} + 2OH^- \rightarrow Ca(OH)_2 \qquad (1.3)$$

C–S–H is less soluble than portlandite, therefore it precipitates faster. Especially at high solution volume (high w/c) portlandite precipitates after the acceleration period.

As the ions in the solution are consumed by the hydration products, the dissolution is accelerated again, increasing the heat release. The C–S–H gel keeps growing, filing the space between the clinker grains when the heat release is maximum [2]. This is the cohesion point and corresponds to what is usually considered the end of the setting.

Deceleration period. The last stage is the deceleration which begins after the peak of the heat rate and continues until the end of the reaction. By the end of a day the heat rate drops and after 24 hours the hydration continues very slowly. The decrease of the heat rate is associated with the decrease of the C–S–H surface and the thickening of the C–S–H gel around the clinker particles. Scattering experiments showed that the hydration rate is associated with the roughness and the thickness of the hydration products [4, 8].

There are two main hypothesis for the onset of the deceleration period. One suggests that it is controlled by diffusion and the other that is limited by the space filling [3, 4]. According to recent experimental evidence, if the former was true the deceleration should happen at the later ages of hydration and not within the first 24 hours [9]. SEM observations of the microstucture suggest the C–S–H grows in an anisotropic way and forms aggregates with different packing densities. More specifically by AFM examination it is observed that the aggregation of C–S–H occurs mostly perpendicular or parallel to the clinker surface [10]. The impingement of the C–S–H aggregates and the formation of a interconnected network in between the clinker grains reduces the available space for new hydrates [9].

1.2.2 Mechanical properties of cement during hydration

The development and setting of C–S–H change significantly the rheology and the mechanics of the cement paste, initially fluid and eventually hardened. Controlling the rheology of cement is crucial for several applications such as casting and transportation of cement. One of the most demanding applications for cement rheology is the oil- and gas- well cementing, where cement is pumped thousands meters deep into the earth to seal the well and keep in place the casing. In this case, cement should remain pumpable for several hours under high temperature and pressure, while still should set within a reasonable time to allow resumption of operations. Rheological measurements of the viscous properties of cement paste such as flow curves (shear rate versus shear stress), yield stress and viscosity versus shear rate, are very useful for devising the pumping of fresh cement paste. Although fresh cement behaves as a viscous liquid, the hardened cement paste is a solid material with remarkable mechanical strength. To probe the elastic properties of the hardened cement paste, experimental techniques ranging from macroscopic mechanical tests to nanoindentation can be used.

During setting, cement is a viscoelastic material, exhibiting characteristics of both solids and viscous fluids. In particular the way the mechanical strength develops and the crossing from the fluid-like properties to solid-like behaviour are intimately connected to the hydration process. The complex time-dependent rheological response of cement during the hydration is usually monitored by dynamic mode rheometry where the shear modulus versus the hydration time is obtained, as shown in Fig. 1.2 [11]. Three different regimes are observed in the

measurement of the shear modulus of cement without admixtures (dashed line of Fig. 1.2): the first increase of stiffness, a dormant period where the change of the elastic modulus is much weaker and the second increase of stiffness.

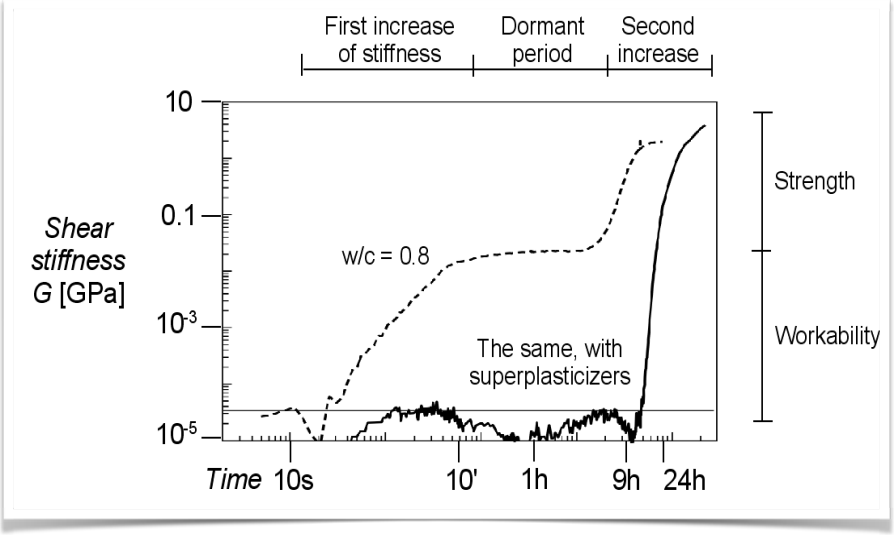

Fig. 1.2 Time evolution of the shear modulus of cement paste with w/c = 0.8 [11]. Dashed and solid line correspond to sample without and with superplasticizers respectively. The horizontal line indicates the minimum significant detection level.

Almost immediately after cement is mixed with water, the shear modulus increases to 10^7Pa, which corresponds to the first increase of stiffness of Fig. 1.2 and it is a clear sign of an initial gelation. At this point the degree of hydration is zero [12] but the cement paste has a measurable yield stress. This first increase occurs during the initial reaction period of the hydration when the clinker particles are sticking together and form a weak network, due to high ionic strength of the interstitial solution. The aluminates have also an important role in this stage [2]. The gel structure is relatively weak and is easily destroyed by vibration, although, if not disturbed, it does not change during the next hours [13]. After this first weak gelation the shear modulus stays at the plateau of 10^7Pa for nearly five hours, which correspond to the dormant period of Fig. 1.2. The length of this period coincides with the period of slow reaction and the first two hours of the acceleration period. The addition of admixtures avoids this initial plateau and makes the cement retain its fluidity.

The second increase of stiffness signals the setting of cement and its transformation into a solid material. During the dormant period the nuclei of C–S–H increase in number, preparing the right conditions for fast growth of C–S–H during the acceleration period. The second increase of the shear modulus happens at the same time as the acceleration period of the hydration, when the initial network of

clinker particles gets reinforced with C–S–H. The densification of the C–S–H layers around the clinker particles continues and by the end of the second increase, when the acceleration period also finishes, the shear modulus has reached the range of GPa due to the mechanical percolation of the C–S–H gel among what is left of the clinker particles. Finally, further hardening occurs over periods from weeks to years due to further hydration and long term rearrangements of the structure over different length scales.

It is clear that cement hydration influences directly the rheology and the development of mechanical strength of cement. Although cement hydration has been the subject of extensive investigation, there are still many issues that are controversial or poorly understood. A particular interesting open question is the linking of the chemical kinetics to the microstucture of the C–S–H and to the evolution of the mechanical properties of cement [4]. The complicated evolution of the microstructure with time indicates that the C–S–H gel can have very different cohesion and space filling properties, not only due to different chemical composition but also due to the interplay between aggregation and arrested kinetics through the hydration and setting process. In particular, at present there is no quantitative or qualitative investigation able to account, from the nano-scale components, for the microstructure formation and all the way up to the mechanical response of the material.

1.3 Stucture of cement and C–S–H

The microstructure that C–S–H forms, the way it evolves and the cohesive forces that hold it together are very important for the mechanical response of the final material. An important unresolved issue in cement research is how to rationalize the formation and structure of C–S–H gel from the molecular scale to the macroscopic scale. As we mentioned before, cement paste itself has a complex structure from the macroscale to the nanoscale. It is composed by different phases of crystalline hydrated products such as Portlandite, AFm and AFt phases, unhydrated clinker particles polydisperse in size, all bound together by the amorphous C–S–H. The initial network, that the clinker particles form as soon as they are mixed with water, provides an initial heterogeneous structure around which hydrates of different sizes and structure grow. In this section, the main characteristics of the C–S–H structure as seen from the macro, meso and nanoscale are presented in more detail.

Looking at the cross section of a concrete block, two phases are distinguished: the aggregates of polydisperse size and shape and the binder, the cement matrix. At the level of few centimetres the cement matrix is fairly homogeneous compared to the aggregates, however a closer look at the level of millimetres reveals the

heterogeneous structure of cement. For example pores of diameter $0.1 - 5$mm can be observed which maybe caused due to trapped air and loss of water during the hydration.

The porosity in cement is usually measured by two types of experimental techniques: one type involves the intrusion of a fluid into the pore system (mercury intrusion, pyknometry, gas sorption isotherms) and the other use particles or fields to probe the material (small-angle neutron scattering (SANS), NMR). The latter techniques can be used even on non dried samples. To achieve more microscopic information on the structure other common techniques used to image the cement structure are electron microscopy techniques such as scanning electron microscopy (SEM) and transmission electron microscopy (TEM), atomic force microscopy (AFM) and scattering techniques such as SANS and small-angle X-ray scattering (SAXS). The mineralogical composition can be identified by X-ray diffraction (XRD) and the chemical composition can be identified by X-ray fluorescence (XRF) and energy-dispersive X-ray spectroscopy (EDS). Using these techniques a more detailed picture of the structure of cement at smaller scales is obtained [1, 14].

1.3.1 Mesoscale structure of cement paste and C–S–H

Cement has a rich multi-phase composition at the scale below millimeter. One can distinguish the microscale ($\mathrm{mm} - \mu\mathrm{m}$) from the nanoscale ($\mu\mathrm{m} - \mathrm{nm}$) domains. At the level of the microscale many crystalline phases are observed together with the amorphous C–S–H. The most common crystal is the portlandite which can grow up to several micrometers in the pore solution and close to the particle surface. The size of the portlandite crystals depends on the temperature and w/c ratio. The ones growing in the pore solution under ideal conditions form hexagonal plates, whereas the ones growing close to the clinker surface are not perfectly shaped. Other crystal phases are the AFm and AFt, which form needles of around one micrometer close to the clinker particles [14].

In the beginning of the hydration, C–S–H grows loosely around the clinker phase starting from nuclei, later it densifies and glues together also the crystalline phases. Fig. 1.3a shows a TEM picture of a hydrating particle of alite, surrounded by C–S–H and portlandite. The morphology of C–S–H can vary from globules, to fibril or foil-like depending on the initial conditions and the hydration stage [15]. The initial composition of cement powder, the w/c ratio, the relative humidity are some of the parameters that influence the C–S–H structure. The fibril growth has been suggested to rise from increased osmotic pressure that ruptures the pre-existing C–S–H layer [15, 16]. Jennings and co-workers investigated the size and diameter of the needles formed under different conditions of relative humidity [17]. The ESEM picture of Fig. 1.3c shows such fibrillar outer product of a rapidly dried sample after three days of hydration. Different growing directions

of the C–S–H are also found in microscopy pictures. C–S–H grows both outwards and inwards the clinker particles, forming the so called inner and outer product respectively. The inner product occupies the space of the hydrating grain and its structure is more compact and amorphous. The outer product is formed in the pore solution and it is reported to form bumps, needles or foils. In the TEM image of Fig. 1.3b, the features of inner and outer foil-like C–S–H can be distinguished [18].

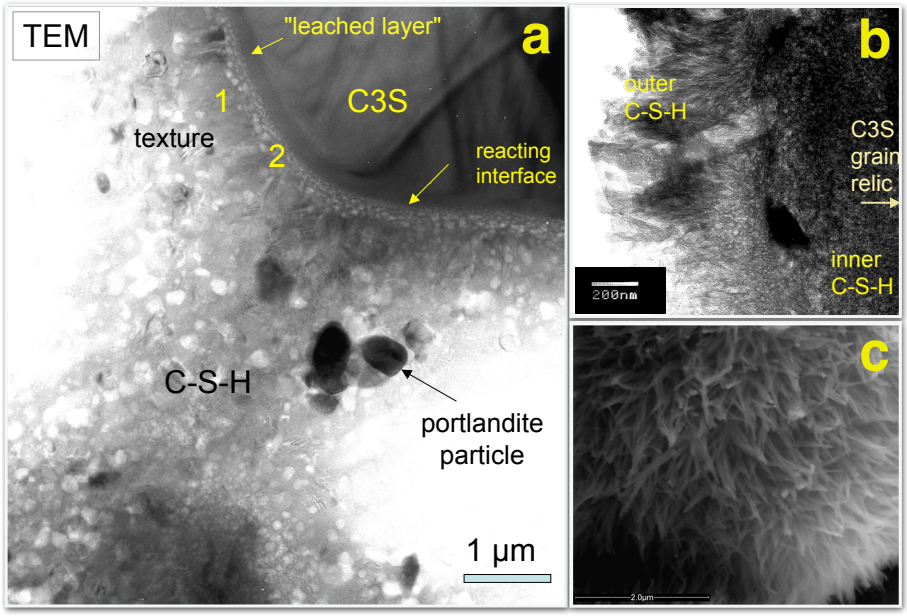

Fig. 1.3 a) TEM image of alite hydration, transforming into C–S–H. Portlandite crystals have also precipitated [18]. b) TEM image of inner, compact and outer, foil-like C–S–H [18] c) ESEM image of fibrillar C–S–H produced during 3 days hydration of alite and then rapidly dried from 100% relative humidity to 33% [17]

A complementary way to examine the structure of cement is by the characterization and distribution of the void space in the material. The initial amount of water influences significantly the overall porosity of the material, the higher the w/c ratio the more porous the material. Initially the voids in cement are big and connected, however as the hydration proceeds and the solid structure percolates, the pores reduce in size and get disconnected. Initial big capillary pores of few μm are replaced by pores of few decades of nm at the later stages or in the cured paste. Proton NMR spectroscopy is a powerful tool to identify location and chemical environment of water in a complex matrix [19]. Its recent application to cement has given interesting insight into the pore size distribution [20–24]. More specifically, the experiments indicate the presence of pores of $2-5$nm and $14-30$nm, both associated with the C–S–H gel.

Observing the structure of C–S–H at the level of nanoscale is challenging. From the current experimental techniques the nanoscale stucture of C–S–H is

not completely elucidated. However, there are some features that are commonly accepted and observed with different techniques. These are the existence of an interconnected network, basic units of characteristic length of few nm with ordered inner structure, pores of few nm and the high specific surface of the C–S–H. In order to interpret the experimental findings of the C–S–H structure, models were developed based either on the hypothesis of the planar grow of natural occurring minerals of tobermorite, jennite and portlandite or on the aggregation of colloidal particles to form a gel. [14]

According to the hypothesis of natural minerals, the C–S–H gel is formed by interconnected layers that are similar to mineral crystals [25, 26]. A schematic representation of the picture proposed by Feldman and Sereda is shown in Fig. 1.4a, where the layers are irregularly stacked and water is trapped in between them or adsorbed in the free surfaces. This hypothesis could explain some properties of the nanostructure such as the observed variable composition of Ca/Si ratio, the crystalline regions and the amorphous layers and they were validated by gas sorption properties, porosity and shrinkage. Gartner described the layers as narrow ribbon-like with random defects that make them wavy and cause them to separate and branch. The growth rate of these ribbons was considered exponential assuming that, due to the kinetics of the hydration, nucleation and growth of the new material happens at the extremities of the ribbons. The flat areas of the ribbon layers form nanocrystalline regions [27]. Gartner suggested that the growth of the ribbons and their branching or impingement could correspond to the acceleration and deceleration regime respectively of the kinetics hydrations (see Fig. 1.1) [27].

A picture that is considered complimentary to the one just described is the so called "colloidal model" [28–30] where the basic building blocks of the gel are solid particle of few nm that form aggregates. The interstices among these particle are the gel pores at the size of few nm and are different from the larger capillary pores that are due to the space which is not yet filled by hydration products. The C–S–H particles have an inner crystalline structure and peculiar shape. This first description by Powers and Brownyard in the 50s was based on evidence from water sorption isotherms and total and non-evaporable water [28].

The main indication of the colloidal nature of C–S–H came with the SANS experiments of Allen in the 80s. The scattering data of a hydrating cement paste showed a characteristic length of $\sim$ 5nm after the induction time and a correlation length $\sim$ 40nm developing due to aggregation [29]. Based on these scattering measurements and sorption data, Jennings proposed a hybrid model of globules with peculiar shape and inner structure. According to his first colloidal model (CM-I), these particles form aggregates with two different packing densities: high density (HD) C–S–H and low density (LD) C–S–H [30]. A further refinement of

Jenning's model (CM-II) accounted for the smallest pores of the C–S–H arising from the internal structure of the globules, that like in the picture proposed by Feldman and Sereda, are composed of tobermorite and/or jennite sheets and water. Therefore, the CM-II combines a layer-like structure into the colloidal-like description and achieves to interpret the adsorption isotherm experiments and processes like creep and shrinkage [31]. Fig. 1.4c shows a schematic representation of the colloidal C–S–H particles forming a gel structure with large gel pores (LGP) of $3 - 12$nm and small gel pores (SGP) of $1 - 3$nm due to the defective stacking of the globules. The globules itself are made of horizontal crystalline layers and intra-globular gel pores (IGP) smaller than 1nm are also present.

The aggregation of C–S–H particles was also investigated by AFM imaging of a hydrating surface of alite [32, 33]. An AFM image with C–S–H nanoparticles of dimensions $60 \times 30\text{nm}^2$ and 5nm thick that compose the C–S–H gel is shown in Fig. 1.4b. The crystalline structure of these small lamellae results to a defined diffraction pattern with broadened diffraction lines either due to the small size of coherent domains and/or due to defects. Recent SANS experiments confirmed the lamellar structure and determined the thickness of calcium silicate layers and of the water [34].

1.3.2 Subnano structure of C–S–H

Many experimental techniques have been used to elucidate the structure of C–S–H. The main findings of the subnano structure of C–S–H comes from models trying to interpret the experiments of X-ray diffraction (XRD), sorption, shrinkage, NMR and AFM. In the 50s based on XDR evidence Bernal [36] suggested that C–S–H has a layered structure related to a crystalline mineral, $1.1 -$ nm tobermorite ($C_5S_6H_5$) and called it tobermorite gel.

In general one observes different types of amorphous C–S–H with variable stoichiometry characterized by the water content and the calcium to silicon ratio (Ca/Si) that ranges from 1.2 to 2.3. C–S–H is usually described as amorphous due to its X-ray diffraction (XRD) patterns that show few broad and weak maxima. However, it has structural similarities with jennite and tobermorite mineral crystals [37]. These minerals have a lamellar structure of calcium oxide layers connected on both sides by silicate chains following Dreierketten arrangement [38]. The main difference of C–S–H that forms during cement hydration is the smaller Ca/Si ratio. Hence, the first atomistic models randomly substituted silicate ions in the mineral with hydroxide groups, with the interlayer space containing strongly absorbed water and additional calcium atoms [39–41]. These models could qualitatively describe gas sorpion and shrinkage but failed to describe the viscoelastic response (creep) of C–S–H and the relative humidity changes (drying shrinkage). In addition, they do not capture the Ca/Si ratio and the density of C–S–H.

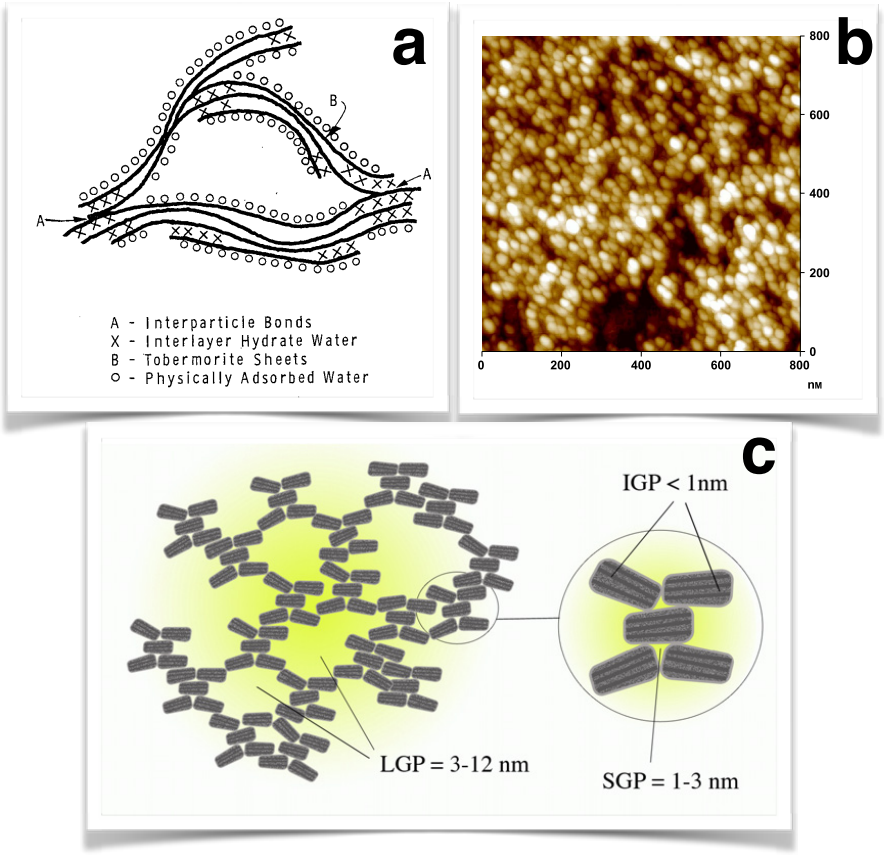

Fig. 1.4 a) Schematic representation of the Feldman and Sereda model of C–S–H forming interconnected layers [25]. b) AFM image of the surface of hydrated cement, where nanoparticles are clearly identified [32] c) Schematic diagram of C–S–H gel nanostructure according to CM-II [31] (picture taken from [35])

Experiments of NMR and SANS together with molecular modeling of C–S–H have improved the understanding of its subnano structure. Initially, NMR experiments provided important information on the pore size distribution of C–S–H and especially the existence of pore of $2-3$nm. Recent SANS measurements have determined the Ca/Si ratio at 1.7 and the density of C–S–H at 2.6g/cm^3 [42]. These values cannot be attained by tobermorite (Ca/Si=0.83, $\rho = 2.18$g/cm^3) or jennite (Ca/Si=1.5, $\rho = 2.27$g/cm^3). Pellenq et al. proposed a model that accounts for such values of Ca/Si ratio and density. This model is based on a bottom-up atomistic simulation approach where starting from a $1.1-$nm of tobermorite they tried to create structures with higher Ca/Si ratio by shortening the silicate chains [43]. The final structure is obtained after energy minimization and suggests that C–S–H has crystalline ordering at the level of interlayer spacing but is glassy at very short distances. The model was validated by comparison with extended X-ray absorption fine structure spectroscopy (EXAFS), XRD, infrared spectroscopy and nanoinden-

tation. More experimental findings for the chemical composition of C–S–H arose by Nonat et al. when they performed alite hydration with a special setting that allowed them to control the calcium hydroxide of the solution [10, 32, 44, 45]. They found that the calcium hydroxide concentration determines the Ca/Si ratio of the C–S–H and the formation of the C–S–H network. The evolution of the stoichiometry of C–S–H can be linked to the lime concentration of the solution. According to this, Nonat categorized C–S–H into three classes with different Ca/Si ratios and developed a predictive thermodynamic equilibrium model based on bulk and surfaces mass laws that might be reliable at local equilibrium conditions [32].

1.4 Forces in C–S–H

Investigating the structure of C–S–H at very small length scales should give insight of how its cohesion arises, which is important for building. In fact the preference for cement over clays or other earthen materials for high performance building structures arises from its strong cohesion which allows for better response to more demanding conditions, like in large structures, high humidity or even building underwater. In clay the particles can stick together and give some cohesion to the material thanks to capillary bridges. Silica colloidal particles can form gels thanks to van der Waals forces. It is clear by considering the tremendous strength of cement with respect to clay or silica gels that the origin of its cohesion must be quite different. In cement, in fact, the hydration reaction produces the C–S–H particles, that have a different and much stronger cohesive nature. In this section, we explore how the cohesion of the C–S–H phase arises. Looking to the subnano structure of C–S–H, its cohesion is still a mystery, but nevertheless minimal coarse-grained approaches were developed to explore the cohesion of C–S–H particles using the physical concepts developed for charged suspensions.

1.4.1 The origin of the cohesion in C–S–H

During cement hydration, cement paste has unusual high ionic concentration of OH^- ions resulting to pH in the range of $10 - 13$. These ions interact with the surface of C–S–H particles giving them surprisingly high surface charge, of the order of one electron charge per 0.35nm^2 for fully ionized C–S–H. To compensate the highly negatively charged C–S–H surfaces, Ca^{2+} counterions gather in the vicinity of C–S–H surfaces forming an ionic cloud. These two characteristics of highly charged particle surface and divalent surrounding counterions make the interactions of C–S–H particles different than other colloidal systems.

The distribution of the ionic cloud of monovalent counterions is described in mean-field theory by the Poisson-Boltzmann equation and DLVO-theory, which predict repulsive forces between the charged surfaces due to the osmotic

pressure of the counterions [46]. However, electrokinetic experiments show that the C–S–H particles behave as negatively charged at low lime concentration when pH < 11.6, whereas they behave as positively charged at high lime concentrations (pH > 11.6 inversion point). The Poisson-Boltzmann equation cannot explain this charge reversal, because it is based on a mean-field theory that fails in systems that are highly charged and/or have multivalent ions. In this case ion-ion correlations should be considered explicitly. Excess of counterions near a spot of the C–S–H surface may be correlated with a lack of counterions in the opposite C–S–H surface and give rise to attractive ion-ion correlation forces. These correlations give rise to a van der Waals type of attractive force, in the same way as correlations between electronic dipoles give rise to London dispersion forces.

This non-classical feature of the double layer, inducing an attraction between two similarly charged surfaces, has been explored within the theory of equilibrium electric double layer, where two regimes can be distinguished [47]. The first regime is the van der Waals regime that occurs at small separation distances and in presence of multivalent ions. The forces in this case change from repulsive to attractive as the surface charge and pH increase. The second regime occurs at larger separations, and especially in case of multivalent ions, the force is alternately attractive and repulsive.

The idea that C–S–H particles interact through surface forces was confirmed by AFM experiments [33, 45]. Measuring the forces of C–S–H nanoparticles by AFM was challenging due to the small size of the particles. The solution came by growing a small amount of C–S–H on the AFM tip and scan the C–S–H grown on flat substrate [33]. By immersing the tip in a salt solution, only repulsive forces were observed as it is expected by the DLVO theory. However, when the tip was immersed in a lime solution an attractive force much stronger than van der Waals forces was detected at separation $2 - 5$nm.

In order to explore the origin of the non-DLVO surface forces, AFM experiments were conducted in solutions with different lime concentrations, pH and ionic strength. Fig. 1.5a shows the forces in C–S–H measured by AFM varying the lime concentration [45]. By increasing the lime concentration in the solution, the calcium concentration, the pH and the ionic strength increases, too. The rise of the pH results in an increase of the surface charge, whereas the rise of the ionic strength leads to the decrease of the Debye length, i.e. the range of the electrostatic interactions becomes shorter. The DLVO theory predicts that an increase of the pH, and consequently of the surface charge, causes stronger repulsion between the surfaces, whereas an increase of the ionic strength condenses the ionic cloud next to the surface therefore inducing an attraction. The total force between the two planes can vary from a purely repulsive regime to a purely attractive one through an intermediate attracto-repulsive regime. To decouple the

influence of pH and ionic strength, AFM experiments in solution of fixed conditions were performed. When the ionic strength was maintained constant, the rise of the pH increased the attraction, in contrast to the DLVO theory. By inverting the constant and varying parameters (keeping the pH constant and rising the ionic strength), it was found that the attraction does not depend on the variation of the ionic strength. The increase of calcium concentration in solution with fixed pH made the attraction stronger. Therefore the most important parameter of the pore solution that influences the attraction of the C–S–H particles is the pH and the second most important is the calcium concentration. This points to the fact the the ionic concentrations next to the C–S–H surfaces cause the attraction and that the DLVO theory fails to explain these results. It is worth noting that under realistic hydration condition the lime concentration of the solution depends on the dissolution process and hence changes during the hydration. This could be the reason of the different observed packing densities of the C–S–H gel in conditions where lime concentration is not fixed, as the interaction forces among the C–S–H particles result to different aggregation processes.

1.4.2 Computing effective interactions in C–S–H

Cohesive forces due to electrostatic and ion correlations are important over different length scales. At the subnanoscale, atomistic simulations have been performed recently within the C–S–H globules to evaluate the cohesion between the layers of tobermorite-like C–S–H using Hartee-Fock, DFT or force field methods [48–50]. The atomistic simulations have elucidated the role of interlayer calcium ions and have been used to compute the hydrogen bonding scheme of crystals as jennite and tobermorite [51] or to investigate the cohesion of tobermorite layers by strong ion-covalent forces [48–50]. The mechanical properties and several spectral of the subnano structure of C–S–H could also be obtained [43, 52].

Although at the subnano scale static ionic correlations are most important, at the mesoscale dynamic correlations are dominant due to the charge fluctuations. For highly charged surfaces and divalent counterions, simulations and theory predict strong attractive forces, more than one order of magnitude larger than Van der Waals forces. It's worth mentioning the high ion concentrations near the C–S–H particle surfaces. The bulk ionic concentrations at pH $>$ 11.6, when charge reversal occurs and hence the forces become attractive, are of the order of 10^{-3}M. In these conditions the average separation of the ions is 10nm and their electrostatic energy is much lower than their thermal energy. The range of electrostatic interactions in the solution is given by the Debye screening length which in this case is 4nm and the Gouy-Chapman length, which indicates the width of the confinement layer next to the surface, is of the order of 0.1nm [49, 53, 54]. Hence most counterions are confined in the vicinity of the surfaces and this layer around the surface has a much higher ionic concentration than the bulk.

Model that treat ions explicitly, in order to account for the ion-ion correlations consider two parallel walls with smeared surface charge representing the opposite charged surfaces of C–S–H particles. The water between the two surfaces is treated as a dielectric continuum and the Ca^{2+} and OH^- ions as point charges. All ions interact solely with Coulomb interactions and satisfy electroneutrality within the simulation cell. A schematic sketch of this double layer model of C–S–H with the solution ions is depicted in Fig. 1.5b from Ref. [50]. Monte Carlo simulations in the canonical ensemble of this model have been used to calculate the ionic distributions, the forces between the two planes and the osmotic pressure [49, 53–55].

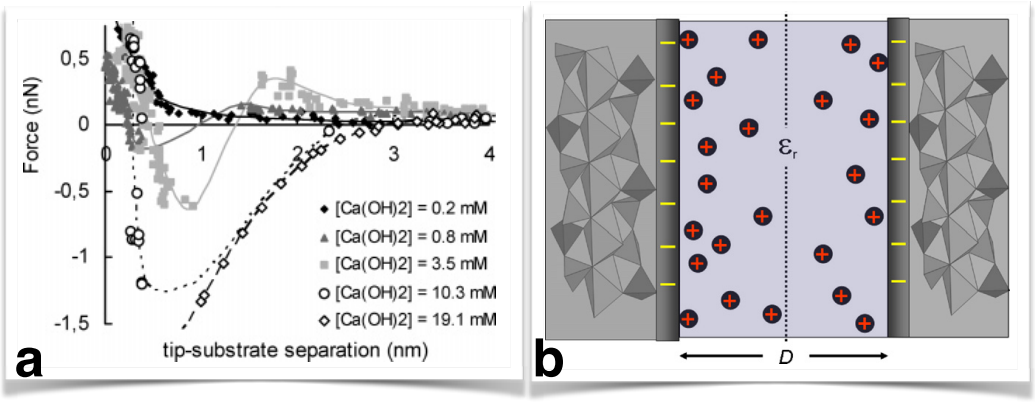

Fig. 1.5 a)Forces in C–S–H measured by AFM in solutions with varying lime concentration [45]. The forces range from a repulsive to an attractive regime, through an attracto-repulsive one. The attractive well gets deeper by increasing the lime concentration. b) Schematic diagram of the double layer model used to evaluate the force between two C–S–H surfaces from Monte Carlo simulation [50]. The C–S–H surfaces are represented by charged planes, the water by a dielectric continuum in which the ions are moving.

The main findings of these simulations confirm the results of the AFM experiments, i.e. that strongly cohesive forces appear in between the C–S–H particles. The range of the attractive force increases with the surface charge density. In the intermediate regime, short-range attractive and longer range repulsive forces are found. It's worth noticing that during cement hydration the pH of the solution and the surface charge density vary through time, therefore the mesoscale forces can get stronger and act on a shorter range over time, providing additional strength and density to the paste. In addition the simulations suggest that the charge reversal is due to the high surface charge density and not due to chemical binding of Ca^{2+} ions to C–S–H surfaces.

Experiments and simulations have established ion correlation forces as the main

reason for cement cohesion and attempted to measure and compute the arising effective interactions in C–S–H. The specific characteristics of the effective interactions in C–S–H depend on the chemical composition of the sample and the hydration conditions. For commercial cement paste under environmental conditions, the effective interactions in the C–S–H formed during hydration are more complex than in model experimental systems [33, 45]. In fact, the concentration of lime and more specifically of the Ca^{2+} ions can be spatially heterogeneous due to the formation of different hydration products and due to the inhomogeneous ion diffusion through the complex pore network of the cement paste. Moreover, C–S–H forces may also be time dependent, due to the progressive clinker dissolution.

1.5 Computational approaches for microstructural evolution of cement

Over the past twenty years few computational approaches have been developed in order to predict the properties of cement paste. Some of them focused more on the hydration kinetics, whereas others on the microstructure of cement. In general the development of models and computation tools for understanding the evolution of the microstructure and mechanics of the cement paste is necessary not only for predicting the performance of concrete but also for designing new cementitious materials. In this section, the computational tools and their main ingredients are described briefly.

Early kinetic models of cement hydration start from one grain of alite and the hydrates are assumed to grow in concentric layers around the grain and the rate of grow is based on various reaction rates and on diffusion [9, 56]. Evolutions of these first models are based on nucleation and growth mechanisms to follow the formation rate of C–S–H as the rate controlling process of cement hydration. In nucleation and growth approaches, the drive for the formation of a new phase is the minimization of the free energy of the system. While the free energy of the new solid phase and the final solution is lower than that of the initial solution, the system has first to overcome an energy barrier associated to the work needed to form an interface between the two phases. After the formation of the nucleus, the solid phase starts to grow and continues to grow as long as it is favourable. The reacted volume fraction is described by the Avrami equation which assumes that nuclei are randomly distributed in the solution [57].

These single grain models were successful on predicting some aspects of hydration kinetics such as the degree of hydration, the heat production and the total amount of bound water. Their downside is that they are based on empirical fitting of parameters and a recalibration of the parameters is needed for each new system. Moreover they do not account for particle-particle interactions

and impingement of the hydrate products, that grow in the pore solution from different alite particles. The Avrami-equation can fit the calorimetry curve until the maximum hydration rate but the fitted parameters have limited physical meaning and do not provide structural information on the hydrated phases [58].

Simple models such as the single grain and the nucleation and growth models captured some features of the kinetics but could not provide information on the development of the microstructure, mechanical strength and porosity of the cement paste. For this purpose computational tools have been developed based on the previous models. Jennings and Johnson proposed a model for cement microstructure that was based on the single-particle approach but using more particles and polydispersity in sizes [59]. This model was an off lattice approach similar to DLA or DLCA where particles or clusters undergo a random walk due to Brownian motion [60]. The HYMOSTRUC model was a follow-up which approached cement microstructure in a statistical way rather than following the hydration of each particle [61]. The most recent development in this category is μic which could efficiently reduce the computational power needed and therefore simulate more particles [62]. Other approaches such as CEMHYD3D and HYDRATICA use a lattice and are based on digital images of cement paste to simulate the microstructure [63, 64]. CEMHYD3D digitalises pictures of cement paste microstructure into a cubic lattice. Each volume element is assigned to a different phase of the paste such as alite, water, C–S–H, portlandite or void. The microstructure evolves locally by applying rules that mimic dissolution, random walk diffusion of the dissolved species and nucleation and growth of hydration products. The most recent lattice tool is HYDRATICA which is based on a stochastic simulation approach for 3D microstructure of cement paste [64, 65]. The basic processes such as dissolution, nucleation, precipitation and diffusion occur due to local probabilistic rules.

The output of CEMHYD3D can be used in finite elements methods to calculate properties as elastic moduli, liquid permeability, etc. However, the disadvantage of CEMHYD3D is that it has no intrinsic time scale for the evolution of the microstructure but for each system the time should be calibrated from experimental measurements of the time evolution of the non evaporable water, chemical shrinkage or heat release. HYDRATICA contains more and precise information on the kinetics, hence it can accurately simulate the reaction rates, ion diffusion and the influence of temperature on kinetics and equilibrium reactions. Moreover, the approach of HYDRATICA tries to highlight that the hydration process and the evolution of the microstructure are governed by the same fundamental principles, hence the two should be treated together. These type of computational tools are able to reproduce cement structures from few micrometers till few mm and they have been proven extremely useful.

Nevertheless the recent use of atomistic simulations for C–S–H reflects the need of a deeper understanding of the nanostucture of the hydration products, to control and design better cementitious materials. The computational challenge of cement is that its structural complexity spans to multiple length scales. Although computational models exist at length scale either larger than μm, simulating the transformation of clinker particles into hydration products or at length scale smaller than the nm, using atomistic simulations to elucidate the subnano structure of the C–S–H globules and of other crystalline phases, no computational approaches exist that address the mesoscale, i.e. the range of length between nanometers and microns. The goal of this thesis was to develop such an approach to investigate the gelation of C–S–H. Atomistic simulations that start from first principles in fact they do not allow to reach system sizes and time scales that would be relevant for the mesoscale. To overcome this, a coarse grained model was developed and is thoroughly presented in Chapter 3. Before getting to describe our new approach, we would like to connect the problem of gelation of C–S–H to the gelation phenomena observed elsewhere, and in particular in colloidal systems.

Chapter 2

Colloidal gels

Gels and amorphous solids are ubiquitous in soft matter and typically form through an interplay between the underlying thermodynamics, dictated by local interactions and the physico-chemical environment, and slow kinetics that may arise through a variety of phenomena, ranging from aggregation, phase separations or glass transition, to strongly out-of-equilibrium conditions imposed by thermodynamics gradients and external fields [66–70]. This combination leads indeed to an impressive range of complex microstructures and material properties. In colloidal suspensions, gels can form even in extremely dilute systems via irreversible aggregation of the particles into thin, fractal structures, but in the vast majority of cases gelation arises due to the arrest of micro- or macro-phase separation where a complex meso-scale organization, typically characterized by very slow dynamics, may emerge from growing aggregates [71–74]. As a result, the microstructure of these metastable states is amorphous at the level of the meso-scale structure and yet intimately controlled by the underlying thermodynamics, that typically determines the local packing and the extent of medium range order. Whereas this interplay adds a further degree of complexity to the physics of these soft materials, it also offers an additional handle to control and design material properties. We have used this perspective to investigate and gain new insight on calcium-silicate-hydrate (C–S–H) gels, that are not usually thought of as belonging to the class of soft matter systems just described. The aim of this chapter is to describe which are the effective interactions and equilibrium phases of a colloidal suspension, how gels may form and what are their main features.

2.1 Colloidal suspensions and effective interactions

A colloidal suspension is made of small particles, ranging between 1 and 1000 nm, dispersed in a continuous medium. Both the dispersed particles and the continuous medium can be gas, liquid or solid; this thesis deals with solid particles dispersed in a liquid medium, the so-called sols. There are multiple examples of colloidal systems in everyday life such as milk, creme, paint, ink, blood, ointments, foam,

etc. Colloidal science not only plays a major role in biology, food, pharmaceutical and agricultural industry but also in building industry. Examples are aerogels that can be formed from colloidal suspensions of silica and are one of the most efficient solutions for thermal and sound insulation or cement is cohesive due to the formation of C–S–H gels.

Gelation occurs in a wide range of systems when attractive interactions are present. The underlying thermodynamics, the strength and the range of the attraction provide different routes to gelation. For example, when attraction is much stronger than k_BT, particles form permanent bonds and grow as fractal clusters that span the system as a gel, even at very low volume fraction. In this section, we give an overview of the main mechanisms leading to different effective interactions in colloidal suspensions [46].

At close contact the particles experience strong repulsion when they touch and this hard-core steric potential can be simply described as

$$V_{steric} = \begin{cases} \infty & \text{if} \quad |\mathbf{r}_1 - \mathbf{r}_2| < \sigma \\ 0 & \text{if} \quad |\mathbf{r}_1 - \mathbf{r}_2| \geq \sigma \end{cases} \tag{2.1}$$

where $\mathbf{r}_1$ and $\mathbf{r}_2$ are the particle positions and σ the particle diameter. Eq. 2.1 corresponds to hard spheres that are impenetrable and cannot overlap in space. Out-of-equilibrium, amorphous glassy states may appear with such a purely repulsive interaction [75], however a gel phase cannot exist without attraction.

Van der Waals forces stem from the correlations between the fluctuations of instantaneous electric dipole moment that can arise even in neutral atoms and molecules. Their strength is much weaker than other chemical (covalent, metallic, etc.) or physical (hydrogen bonds, electrostatic, etc.) forces but they are more ubiquitous as they exist even in uncharged system or in colloidal particles. Different contributions to van der Waals interactions can arise from interactions between rotating dipoles (Keesom forces), between a permanent dipole and an induced one (Debye forces), and between two instantaneously induced dipoles (London dispersion forces). In case of neutral or apolar atoms and molecules the Keesom and Debye forces are zero and the main contribution comes from the London forces. The resulting van der Waals interaction potential is

$$V_{vdW} = -\frac{A}{6}\left(\frac{2R_1R_2}{r^2-(R_1+R_2)^2} + \frac{2R_1R_2}{r^2-(R_1-R_2)^2} + \ln\left[\frac{r^2-(R_1+R_2)^2}{r^2-(R_1-R_2)^2}\right]\right) \tag{2.2}$$

where r is the center-to-center distance between two spheres of radii R_1 and R_2 and A is the Hamaker constant that depends on material properties and on the polarizability of both the colloidal particles and the surrounding solvent. For monodisperse particles of radius R and for particle separation $r \ll R$, the van der Waals interactions reduce to

$$V_{vdW} \approx -\frac{A}{12}\frac{R}{r} \tag{2.3}$$

The Hamaker constant depends on the optical refractive indices of the colloids and the solvent in such a way that by index matching the two materials, the van der Waals attraction can be strongly suppressed [46]. For unmatched indices, Eq. 2.3 shows that when the particles approach the van der Waals interaction diverges negatively leading to particle coagulation. Colloids are forbidden to overlap due to Born repulsion and this is usually modeled by hard sphere (Eq. 2.1) or soft sphere potentials [76].

If the colloids are charged, electrostatic forces arise and attract free counterions around the particles. Some of them get bound to the surface of the colloids forming the so-called Stern layer of condensed counterions which can be accounted for by suitably renormalizing the colloid charge. The remaining free counterions may screen the renormalized colloidal charge and the resulting electrostatic interaction between two colloidal particles is

$$V_C = Z^2 \left(\frac{\exp(\kappa R)}{1+\kappa R} \right)^2 \frac{\exp(-\kappa r)}{\epsilon r} \tag{2.4}$$

where Z is the bare charge of colloids with radius R, r is the interparticle distance, ϵ the dielectric constant of the solvent and κ^{-1} is the screening length

$$\kappa = \sqrt{\frac{4\pi\rho_c}{\epsilon k_B T}} \tag{2.5}$$

where ρ_c is the density of free counterions. The screened potential V_C is computed using the Poisson-Boltzmann equation which gives a mean-field description of the electrical double layer and depicts the charge of the colloids as screened by the cloud of counterions. The validity of this approach is limited to colloidal systems with monovalent counterions, dilute solutions and low surface charges.

The theory developed by Derjaguin-Landau-Verwey-Overbeek (DLVO) gives the total interactions between charged colloids as the sum of the hard-core repulsion (Eq. 2.1), the van der Waals attraction (Eq. 2.2) and the double-layer repulsion (Eq. 2.4) terms

$$V_{DLVO} = \begin{cases} \infty & \text{if} \quad r < \sigma \\ V_{vdW} + V_C & \text{if} \quad r \geq \sigma \end{cases} \tag{2.6}$$

In Fig. 2.6 a schematic diagram of the DLVO potential versus interparticle distance is shown together with the corresponding van der Waals and electrostatic double layer interactions. The specific shape of the DLVO interaction is tuned by the choice of the solvent, as its dielectric constant affects both the Hamaker constant and the V_C, by thermodynamic quantities as density and temperature, that may explicitly change the screening length, by the addition of salt, or finally by increasing the counterions valence, that decreases the electrostatic repulsion. The combination of attraction and repulsion may result in an overall interaction

potential with a deep primary minimum, an energy barrier and a secondary minimum [77].

As mentioned before, the electrostatic double layer term of the DLVO potential stems from a mean-field treatment of the counterions through the Poisson-Boltzmann equation and hence its applicability is limited to monovalent counterions and low surface charges. When ions with higher valence or strongly charge particle surfaces are involved, forces due to ion-ion correlations may arise. This may give rise to a strong short range attraction on top of the van der Waals attraction and to a long range repulsion. This is actually the case for clays and cement as it has been discussed in Section 1.4.

Another mechanism of colloidal attraction stems from the presence of additional particles in the suspension, the so called depletants, which are usually non-adsorbing small particles, such as polymers or micelles. As soon as the large colloidal particles come closer to each other, the available volume for the small-sized depletants is reduced and the result is an entropic attractive force among the large colloids that brings them together in order to maximize the available volume for the depletants. This phenomenon results in a net interaction that can be described in terms of an attractive potential well [77]. The range of the potential in case of polymers can be tuned by the length of their chains, whereas the depletant concentration and solubility increases the strength of repulsion among the depletant and hence the net attraction between the colloidal particles. In combination with electrostatics these interactions can lead to a scenario qualitatively similar to Fig. 2.1 [78].

2.2 Equilibrium phases and arrested states

Colloidal gels are typically formed through an interplay between the underlying thermodynamics, dictated by effective interactions of the types just discussed and the physico-chemical environment. In many cases gelation occurs due to the arrest of micro- or macro-phase separations. The attractive interactions induce a phase separation into a colloid-rich and colloid-poor phases and the growing aggregates develop into a complex mesoscale organization, typically characterized by very slow dynamics. This may lead to a variety of arrested states that may vary with the volume fraction ϕ (typically the fraction of total volume occupied by the particles) and the strength of the attraction. The development and properties of gels formed under weak attractions or weak attractions and repulsion have been intensively investigated in the last few years. In this section, we present the phase diagrams and the properties of few such cases.

In Fig. 2.2a the phase diagram of monodisperse hard spheres colloidal sus-

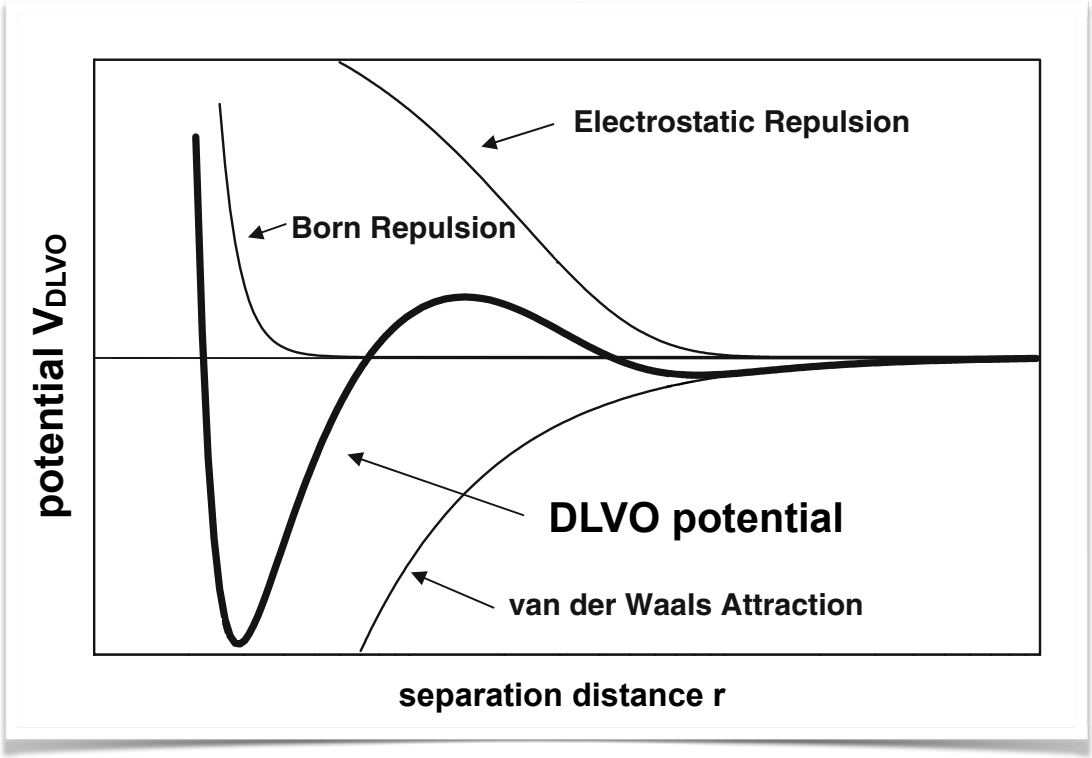

Fig. 2.1 Schematic plot of the DLVO potential, showing the contributing terms of Born repulsion, van der Waals attraction and electrostatic repulsion. The overall DLVO interaction has a short-range attractive well and a repulsive shoulder.

pensions is shown [71]. The phase transition of such suspensions is driven purely by configurational entropy which leads to different packings due to the fact that particles are impenetrable at high densities. Increasing the volume fraction, the system goes through two first order phase transitions: one occurs above the freezing volume fraction $\phi = 0.494$ where the system from a pure fluid (F) phase goes into a coexistence of fluid and crystal (F+C) and the second occurs above the melting volume fraction $\phi = 0.545$ where the system forms a crystal (C) till the maximum crystal close packing $\phi = 0.74$. Apart from the equilibrium phases, an amorphous glass phase is typically found in a range of volume fraction between 0.58 and 0.64 (random close packing) [75].

When attraction is added to the hard spheres interaction, the phase diagram becomes more complex, as shown in Fig. 2.2b, displaying a richer range of phase coexistences and transition lines. If the attraction strength is weak $V \ll k_B T$, thermal fluctuations easily break the bonds and the particles are in a gas phase, whereas if $V/k_B T$ increases (strong attraction) the particles can stick together at low volume fraction and phase separate into a colloid-rich (liquid) and a colloid-poor (gas) domains or get trapped into metastable states, like gels and

glasses. The liquid-solid and liquid-gas transitions (for $T < T_c$) (depicted by lines) are first-order phase transitions, which are accompanied by adsorption or release of energy and change in density. Fig. 2.2c shows in more detail the gas-liquid coexistence region of Fig. 2.2b. The transition through the critical point corresponds to a second order phase transition, where the first derivative of the free energy with respect to a thermodynamic variable is continuous in contrast to the first order phase transitions. Above the critical point the system may continuously pass from gas to liquid. For temperatures below the critical point and volume fractions within the binodal curve (depicted in Fig. 2.2) the system is metastable and spontaneously phase separates into coexisting phases with compositions corresponding to those marked by the binodal line at the same temperature. Many systems also exhibit a spinodal curve which separates the metastable region from an unstable region. Within this unstable region the system separates through a process called spinodal decomposition into a dense and a dilute phase [79].

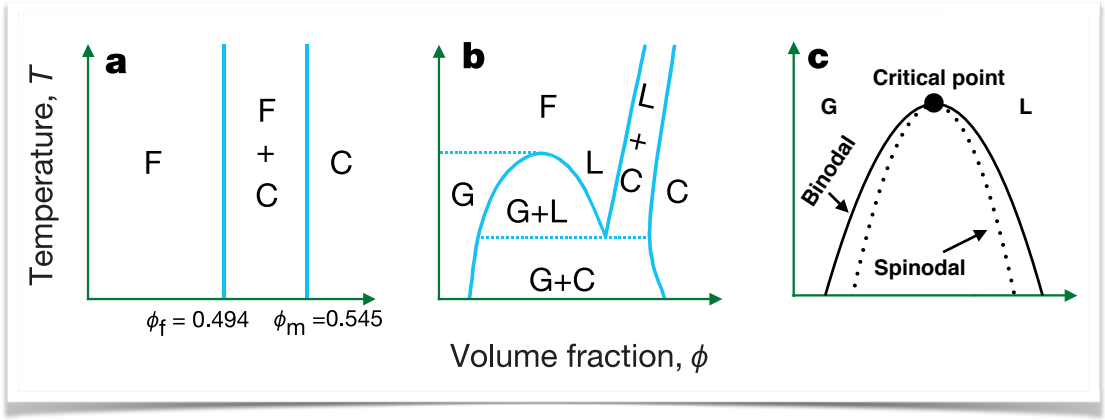

Fig. 2.2 a) Phase diagram for purely hard-sphere system, showing the fluid (F) and crystal (C) phases. The non equilibrium glass phase occur for $0.58 < \phi < 0.64$ [71]. b) Phase diagram for hard spheres with long-range attractions, showing the equilibrium phases of gas (G), liquid (L) and crystal phases [71]. c)Illustration of the binodal region of phase diagram b, showing the spinodal and the upper critical point.

Attractive systems following phase diagrams similar to Fig. 2.2b and Fig. 2.2c may form gel phases through the kinetic arrest of the phase separation. The gel morphology depends on the specific kinetic path followed. In particular the gel morphology can be very different if the aggregation develops through nucleation and growth or via spinodal decomposition, depending on the region of the binodal in which the quench occurs. The nucleation and growth process occurs when the system is in the metastable region under the binodal line. The phase separation by crossing the binodal far from the critical point is a first order transition associated with a discontinuity in the free energy derivative with respect to a thermodynamic variable. In the nucleation and growth mechanism, in order to create an initial

nucleus the system should overcome a free energy barrier that corresponds to the formation of an interface. Density fluctuations may favor the formation of the initial critical nucleus. The nucleus grows until it reaches the composition dictated by the binodal (phase coexistence) curve and that corresponds to the phase separation. The phase separation may be kinetically interrupted, and in many cases this corresponds to the formation of a gel, if the dense phase is arrested into an interconnected network structure that can withstand external stresses. Crystallization can proceed via nucleation and growth as well and interfere with the gelation, as we will also see in Chapter 4 [80]. In most cases, the most stable crystal is face-centred cubic (fcc), although hexagonal close-packing (hcp) is always present even under ideal conditions of equilibration. The hcp may transition to the more stable fcc, but because the energy difference between the hcp and fcc structures is small, the driving force is also small and the transition may be very slow.

In the spinodal decomposition the separation between the colloid-rich and colloid-poor phase occurs uniformly throughout the system and not at discrete nucleation sites. Moreover it arises from periodic modulations of the density rather than from the density fluctuations. As long as the system is within the spinodal region the initial formation of microscopic clusters occurs due to diffusion. These clusters rapidly grow and coalesce until there are two distinct macroscopic phases. The free energy minima determine the equilibrium composition of the binodal, whereas the compositions between the inflection points, where the free energy has negative curvature, correspond to the unstable region where spinodal decomposition may occur. The system may reach the spinodal region of the phase diagram from a transition through the binodal region or the critical point. However, the nucleation mechanism is more often observed than the spinodal decomposition, for which it is needed to quench very rapidly the system below the spinodal [67]. The spinodal decomposition may also be kinetically arrested and in some cases this leads to the formation of gels, characterized by complex bi-continuous network structures that have interesting optical and mechanical properties [81].

When long-range repulsion, that is mainly electrostatic in nature is present in addition to short-range attraction as shown in Fig. 2.1, the scenario just discussed is qualitatively modified. In this case the phase separation is pushed towards higher attraction strength due to the charge stabilization and a microphase separation may occur. The height of the long-range repulsion in the effective interaction potential may act as a stabilizing barrier and increase the lifetime of the particle bonds. The long-range repulsion may stem from specific microscopic characteristics of the system or may also be the effect of residual charge of the colloidal particles. The control parameter of the repulsion range is the Debye screening length and if tuned appropriately together with the attraction strength

may produce an equilibrium cluster phase. The formation of such stable cluster phases occurs in the low density and strong attraction region of the phase diagram and is the indication of a typical modulation length due to the competition of attraction and repulsion [82–84]. In Fig. 2.3, the phase diagram of a system with short-range attraction and long-range repulsion is shown [84]. As the density increases the clusters aggregate into elongated structures preserving the modulation length and modulated phases form, of columnar arrangement (triangles) and of lamellar mesophases (squares) at even higher density. However, in experiments and simulations, metastable gel states are observed, due to the fact that the anisotropic microphases can form a disordered network relatively easily and this leads to a kinetic arrest of the microphase separation. This type of phase diagram is particularly interesting for the C–S–H, as we will see in the next chapters.

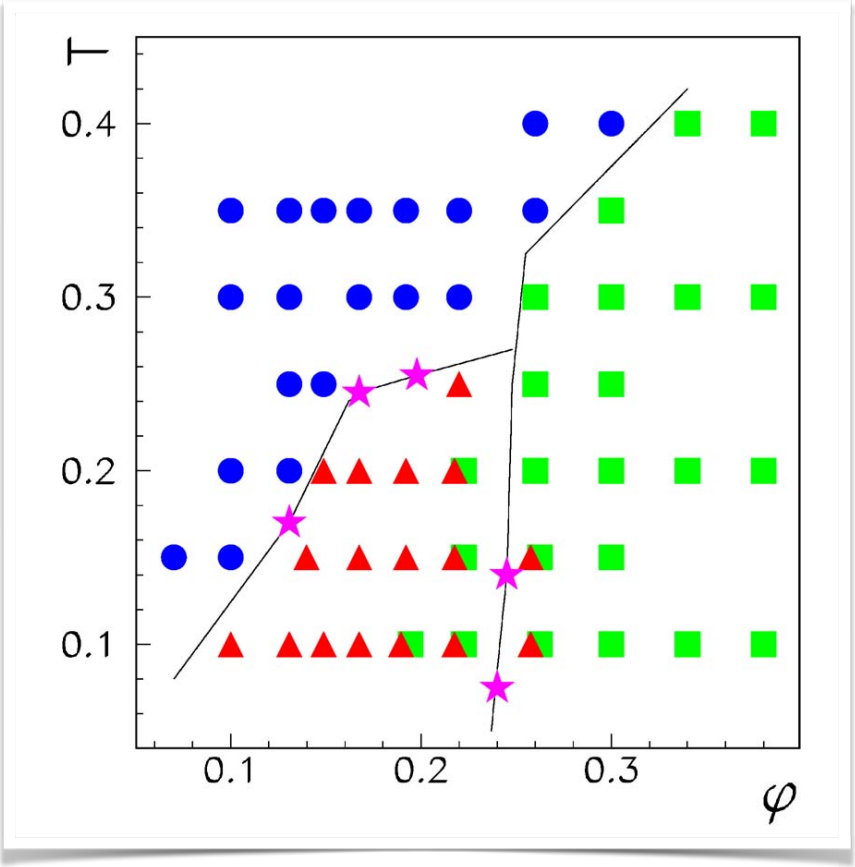

Fig. 2.3 The phase diagram of a system with short-range attraction and long-range repulsion [84]. Circles correspond to the disordered phase, triangles to the columnar phase, squares to the lamellar phase and stars to the points where the free energies of two phases cross.

2.3 Fractal Gels

For the formation of space spanning structures at very low volume fraction, strong attractive interactions are needed. With sufficiently strong attraction, particles may diffuse and stick irreversibly to each other via a process called diffusion limited cluster-cluster aggregation (DLCA) [60]. In this way thin, fractal aggregates are formed (see Fig. 2.4a), grow and eventually fill the space. This is a kinetic mechanism that can form solid-like gels at arbitrarily low particle volume fractions. This requires interactions to be strong enough to avoid any particle rearrangements once they are aggregated. In most cases, particle rearrangements are instead important and the gel formed tend to be denser and locally thicker. The second case is more interesting for the type of gels that we will investigate in the next chapters but here we give a short overview on the main features of fractal gels.

Slow dynamics of the arrested states and stress-bearing properties of the networks that signify the onset of gelation, can be probed experimentally using light scattering and rheology. When particles aggregate, a peak develops at the low-q region of the scattering vector dependence of the scattering intensity that indicates a rather well defined distance between the growth points. The more they grow, they become nearly stationary in space as they diffuse slower than the single particles. That is because the aggregation is diffusion-limited with diffusion coefficient $D = k_B T/6\pi\eta R$ which is inversely proportional to the radius R of the domain. The temporal evolution of the q-dependence of the scattering intensity traces the aggregation; the low-q peak systematically shifts to lower values and its intensity increases reflecting the increase of the size and mass of the growing structures respectively. At larger q the scattered intensity decreases as a power law $I(q) \sim q^{-d}$, with $d = 1.8$ for DLCA and its magnitude remains stationary during the aggregation. Scattering profiles of different time lapses can be collapsed onto a single master curve by rescaling the q axis with the position of the q-peak q_p and the $I(q)$ axis with the q_p^{-d}. This dynamic scaling reflects the self-similarity of the growing blocks [85, 86].

The structure and properties of fractal aggregation and of the resulting gels were extensively studied in the 80s [86, 87]. The number of particles contained in an aggregate and therefore its mass M depends on its linear size R as $M \propto R^{d_f}$, where the exponent d_f is the fractal dimension and $d_f < d$ with d being the euclidean dimension of space. Upon formation of fractal aggregates in a suspension, the system will ultimately form a volume-filling gel. The density of the fractal clusters decreases as their mass increases, $\rho \sim M/R^3 = R^{d_f-3}$ [86].

More complex aggregation processes may be described using a reaction limited cluster aggregation (RLCA) where particles or clusters do not necessarily stick together irreversibly but repeated contacts are needed for the aggregation to take

place. This mechanism may correspond to an energy barrier associated to the aggregation process. RLCA aggregates are more compact (see Fig. 2.4b) and have therefore a higher fractal dimension than DLCA aggregates. The differences in the mass structure correspond to different exponents also for the wave vector dependence of the scattering intensity. DLCA fractal objects correspond to $d_f = 1.8$ and RLCA to $d_f = 2.3$.

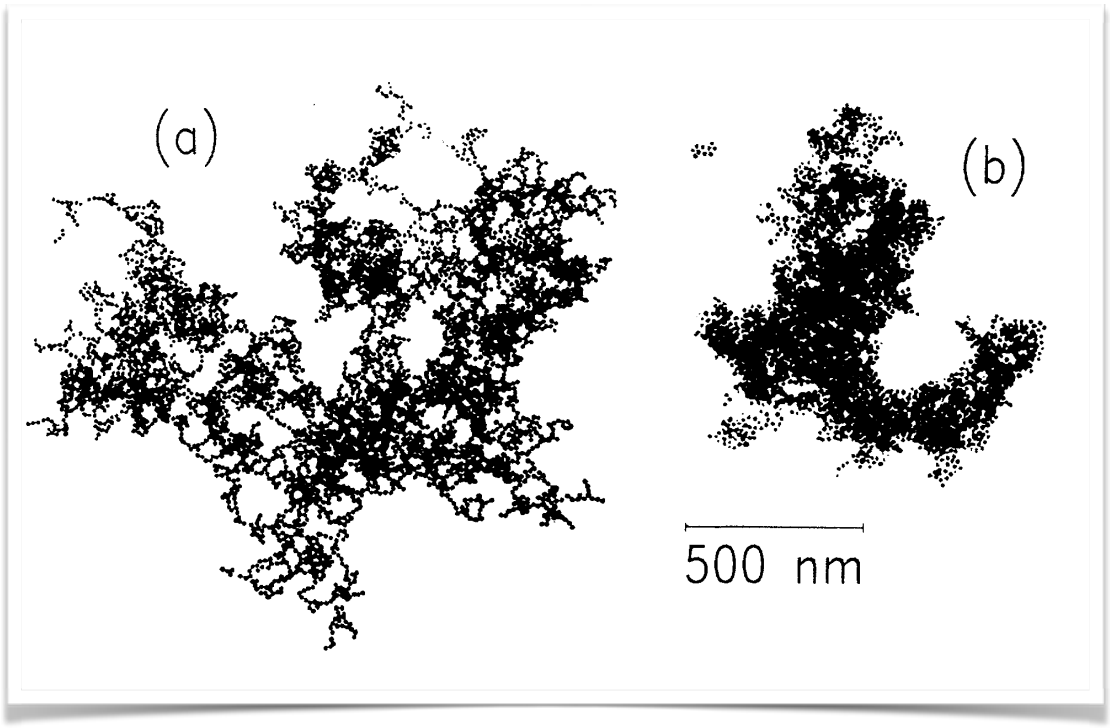

Fig. 2.4 Fractal clusters formed by aggregation of gold colloids a) through the DLCA mechanism and b) though the RLCA [87]. DLCA results to thin and open clusters whereas RLCA produces more compact clusters.

These differences in the aggregation kinetics influence, through the morphology, the linear size of the aggregates R_c. During aggregation, the volume fraction of the fractal clusters ϕ_c decreases until it reaches the volume fraction ϕ of the particles in the overall suspension, hence the characteristic size of fractal clusters scales as

$$R_c \sim \phi^{1/(d_f-3)} \tag{2.7}$$

Therefore, the cluster size decreases as the overall volume fraction increases, or conversely, as the system becomes more dilute, the clusters will grow to larger sizes before they touch. In both cases, this may lead to a fractal gel network spanning the whole system.

2.4 Colloidal gels as glassy or jammed materials

From the discussion in Section 2.2 it is clear that colloidal gels have to be thought of as metastable states, in which the system gets trapped due to a tremendous slowing down of particle kinetics. In this respect colloidal gels can be seen as glassy systems.

It has been proposed that this liquid-solid transition can be seen as part of the phenomenology usually referred to as jamming, similar to the liquid-solid transition that hard sphere systems undergo upon increasing density or dense granular systems may undergo under external load. In the phase diagrams of Fig. 2.2 is shown how the temperature and the volume fraction can influence the formation of a gel. Another parameter that may influence the formation or destruction of gels and glassy states is the external load.

Liu and Nagel used the density as an intrinsic variable to provide a unified description of athermal, thermal and attractive systems [88]. The experiments of Trappe et al. suggested a unifying jamming phase diagram for attractive colloidal particles supporting the idea of jamming for describing the behavior of attractive colloids [68]. In Fig. 2.5, this jamming phase diagram is shown and it has three control parameters, the strength of the attraction with respect to k_BT, expressed as the thermal energy over the interparticle energy k_BT/U, the inverse volume fraction $1/\phi$ and the stress σ/σ_0 where $\sigma_0 = k_BT/R^3$ sets the stress scale in weakly attractive systems [68]. This phase diagram has been proposed on the basis of the fluid-solid transition of a weakly attractive colloidal system that exhibits the same gelation behavior with increasing ϕ and decreasing thermalization or stress. The jammed state is determined by the existence of a low-frequency elastic modulus $G\prime \neq 0$ and the divergence of viscosity η. Moreover, the critical-like behavior of the three controls parameters define the phase boundaries as depicted in Fig. 2.5. The divergences of the transition lines correspond to aforementioned cases. In the limit of very small attractions the system resembles hard-pheres and jams to form a solid close to the random close packing. In the limit of high attractions, instead fractal clusters fill the space and form a gel due to the irreversible bond formation. At high stresses sintered solids can be formed.

If the gels formed in attractive colloidal suspensions can be seen as part of these jammed materials, the properties of these solids (structure and mechanics) will be determined not only by the strength of the interactions and the density, as opposed to crystal, but also by the conditions in which the material is processed. The external load that appears as a control parameter in Fig. 2.5 can be a way to bring in this type of processing conditions. In practical life, realistic processing conditions may be more complicated, implying combined changes of the three control parameters. In the case of C–S–H gels, the evolving chemical environment during gel formation should also be considered, for example, as it emerges in Chapter 1 on cement hydration.

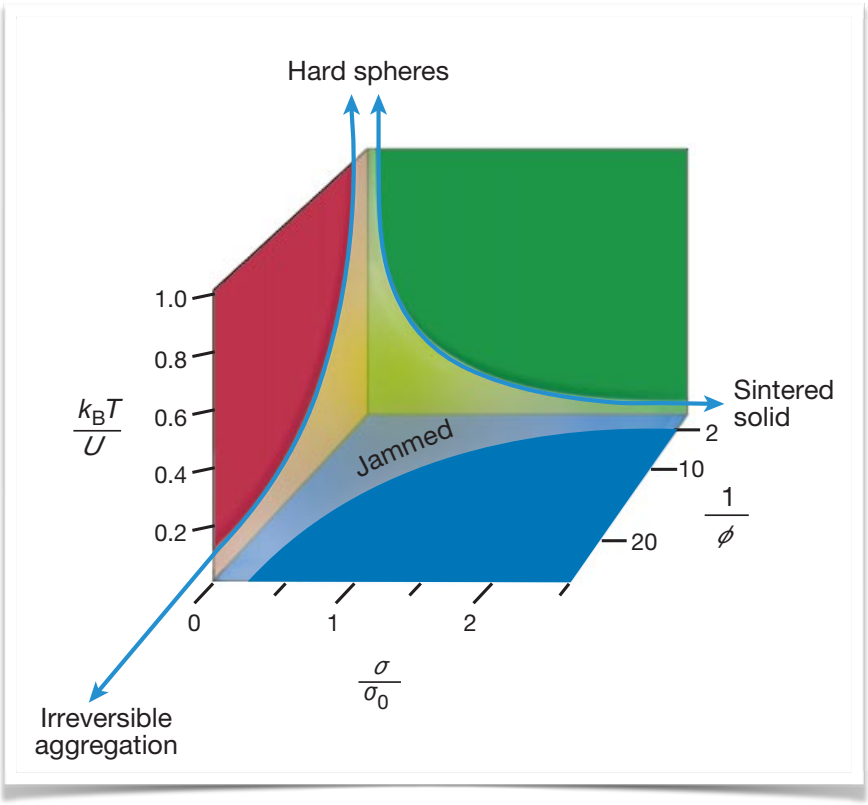

Fig. 2.5 Phase diagram for attractive colloids a jammed region by tuning the thermalization, the volume fraction and the stress. Details of different systems may change the shape of this diagram but not the overall behavior [68].

Out-of-equilibrium systems may continuously evolve with time as they slowly evolve towards their equilibrium configuration by getting trapped to the next local minima. In the case of colloidal gels the system is trapped in a kinetically arrested microscopic configuration but not necessarily a thermodynamically stable one. As a consequence its response, as it can be quantified by stress or strain relaxation, depends not only on time lapsed but also on the age of the system. Usually, the dynamic processes slow down further as the system ages because it is trapped for longer time in metastable states corresponding to deeper local minima of the potential energy landscape. Gels and glasses slow dynamics can be rationalized based on the fact that it is due to the relaxation of internal stresses that were generated due to the gelation process (for example due to unbalanced osmotic pressure exerted by the solvent). The internal stresses can also significantly affect the mechanics, for example enhancing the rigidity of the connecting strands in a gel network [89].

The microstructure of amorphous solids is far more complicated than crystalline

solids, especially at the level of the mesoscopic organization. In crystalline solids, the crystal structure can be linked directly to the elastic constants measured by mechanical tests, as all particles in the microscopic structure follow the macroscopic strain (affine deformation). This is different in the case of amorphous solids, such as gels, which are mechanically stable but do not necessarily fulfil Maxwell's criterion for rigidity, according to which the number of constraints needed for mechanical stability should equal the number of degrees of freedom [89]. In fact gels are rigid even with less mechanical contacts between particles than the ones required by Maxwell's criterion and the ones that the particles would have in the crystal. Moreover, gels may exhibit significant non-affine response under strain: the particles do not necessarily follow the imposed deformations due to the presence of internal stresses. These dynamical processes may be crucial to the mechanical stability of the gel [89].

Chapter 3

C-S-H growth under precipitation

We investigate the development of gels under out-of-equilibrium conditions, such as calcium-silicate-hydrate (C-S-H) gels that form during cement hydration and are the main responsible for cement mechanical strength. We propose a new model and numerical approach to follow the gel formation upon precipitation and aggregation of nano-scale colloidal hydrates, whose effective interactions are consistent with forces measured in experiments at fixed lime concentrations. We use Grand Canonical Monte Carlo to mimic precipitation events during Molecular Dynamics simulations, with their rate corresponding to the hydrate production rate set by the chemical environment. In this chapter, we present our model and the main results. Our results display hydrate precipitation curves that indeed reproduce the acceleration and deceleration regime typically observed in experiments and we are able to correctly capture the effect of lime concentration on the hydration kinetics and the gel morphology. Our analysis of the evolution of the gel morphology indicate that the acceleration is related to the formation of an optimal local crystalline packing that allows for large, elongated aggregates to grow and that is controlled by the underlying thermodynamics. The defects produced during precipitation favor branching and gelation, that end up controlling the deceleration.

3.1 Introduction

As we mentioned in Chapter 2, in this work, we have used a soft matter perspective to investigate and gain new insight on calcium-silicate-hydrate (C-S-H) gels. C–S–H gels form during cement hydration: the reaction of anhydrous cement with water results in the formation of hydrates compounds and C-S-H is the primary hydration product of Portland cement paste, and the main responsible for cement strength [4, 42]. The C-S-H hydrates progressively assemble, as they precipitate in the capillary pore solution, into a structure that has structural complexity on multiple length-scales and literally glues together the final solid product [32, 42, 90, 91]. In spite of many investigation efforts, the growth of the gel structure during hydration and the development of mechanical properties during setting are still the subject of an intense debate. Over the relatively early

stages of the hydration, the C-S-H gel grows over a few hundreds of nanometers, progressively filling the pore space, and is indeed a soft-material. These stages are particularly interesting because they offer a unique possibility to control/modify the material properties at the nanometer scale or at the level of the basic chemical components in a material of such complexity. Nevertheless, how changing chemical components and/or modifying the hydration conditions affect the development of the C-S-H gels is far from being well understood. This is becoming a compelling question to address in cement, since the forefront of research is in more sustainable chemical modifications that would allow to reduce the CO_2 footprint of the material, corresponding to 5-8% of the world man made CO_2 [92, 93].

The structure of C-S-H gels after setting displays a disordered and heterogeneous mesoscale organization built upon structural units of typical size $5 - 10$ nm, as indicated by neutron scattering and AFM experiments [10, 34, 35, 42]. Structural and mechanical aging indicates that such microstructure develops out-of-equilibrium, as it has to be expected in view of the changing chemical and physical environment as the hydration proceeds. On this basis, the gel growth has been thought of in terms of an irreversible aggregation of colloidal nanoparticle, along the line of diffusion-limited aggregation (DLA) or diffusion-limited cluster aggregation (DLCA) [31, 42, 60, 94]. The presence of colloidal nano-scale C-S-H hydrates, mostly platelets with a typical size of $1 - 30nm$ and a complex internal layer structure are indeed reported in a number of experiments performed on tricalcium silicate (the main source of C-S-H in Portland cement and often used as a model system for cement hydration) [4, 10, 32, 34, 42, 95]. This lengthscale gives a good indication for the typical size of locally compact layered calcium-silicate structures [49], whereas there is little direct evidence of a fractal aggregation nor the final gel morphology can be easily related to this type of process [96, 97]. Moreover, a fractal type of growth can not be immediately related to the characteristic non-monotonic dependence of the hydration rate, as measured by calorimetry: the heat flow associated to hydration kinetics typically displays an acceleration and deceleration regime that are expected to be coupled to the development of the gel morphology (and mechanics), although a coherent microscopic picture is still missing [4]. As an alternative to the fractal aggregation of nanoparticles, a growth mechanism based on sheets of rather crystalline C-S-H that would branch because of the defects produced during precipitation, has been proposed [27, 98]. This type of picture is considered complementary to the colloidal one because it is not based on colloidal building blocks but it does capture many features of the final gel morphology (as shown for example in SEM images [97] or indicated by NRM studies [22]), in addition to being consistent with the hydration kinetics: the acceleration can be related to the nucleation and growth of the elongated structures (that are crystalline or semicrystalline), whose steric interactions and impingements would eventually determine the deceleration regime and the final mesoscale amorphous organization of the gel [99, 100]. In spite of grabbing a

few fundamental features of C-S-H growth and morphology specifically coupled to cement hydration, this model has never been translated into an analytical or computational approach that would allow to quantitatively test it.

Here we propose a new model and a computational approach to investigate the development of C-S-H gels under out-of-equilibrium conditions that can be related to cement hydration, via a combination of Monte Carlo and Molecular Dynamics simulations. Our model is based on nano-scale (colloidal) hydrate units [1] that aggregate, upon precipitation, due to effective interactions that are consistent with the ones measured in experiments via AFM [45]. Although we do not capture all the chemical details of the system and our description of C-S-H is coarse-grained, our approach allows us to follow the morphology and the mechanics of the gel during precipitation, in presence of different rates of hydrate productions. The kinetics of hydrate precipitation in our numerical simulations displays the characteristic non-monotonic dependence on time of the hydration rate typically observed in experiments. Upon changing the effective interactions to mimic different lime concentrations as investigated in [10, 45], our simulations predict the same qualitative change in the hydration kinetics and in the gel morphology as the one observed in experiments. It is important to notice that in our study we don't impose a specific growth mechanism for the gel, that developes instead as a result of the interplay between the hydrate production rate, controlled by the chemistry, and the underlying thermodynamics controlled by the effective interactions. We obtain a physical picture for the connection between the hydration kinetics and the development of the gel morphology that is consistent with the picture proposed in [27], in spite of the colloidal nature of our approach. The acceleration can be associated to the nucleation and growth of elongated structures that are crystalline or semi-crystalline (depending on the production rate of hydrates in the system) and tend to branch, due to the presence of defects created during precipitation, into a $3d$ gel network. The deceleration arises during the network formation and densification and it is therefore controlled by the steric interactions among different extended aggregates. We propose that our simple model captures, for the first time, the basic fundamental mechanisms underlying local packing, growth and gelation of C-S-H during cement hydration. The new approach described gives novel insight into outstanding issues for designing novel sustainable cements.

[1] This colloidal hydrate size basically sets the length scale below which we do not account for the detailed C-S-H structure

3.2 Precipitation and gelation of C-S-H gels: a meso-scale model

To model the formation of the C-S-H gel via precipitation and aggregation of C-S-H hydrates, we consider an open system of interacting colloidal particles within a small volume contained in a capillary pore of the wet paste. We mimic the precipitation via a Grand-canonical Monte Carlo (GCMC), where a particle can be inserted or removed from the volume V with a probability given by the Metropolis Monte Carlo scheme [76]

$$P_{ins/del} = \min\left[1, e^{\pm\beta(\mu_{exc}-\Delta U)}\right] \ , \tag{3.1}$$

where k_b is the Boltzmann constant, T is the temperature, μ_{exc} is the excess chemical potential and ΔU is the difference in the total potential energy of the particle configurations due to the insertion or removal of a particle. The idea is that the insertion of a particle with the GCMC procedure corresponds to the precipitation of a C-S-H colloidal hydrate. The chemical potential therefore represents the free energy gain corresponding to the formation of the C-S-H hydrates and its value sets the equilibrium density of C-S-H that can be reached in the pore. Although we cannot simply estimate this value, we consider that during cement hydration and C-S-H precipitation, the pore solution is always supersaturated and densification does not stop [10]. Hence, to reproduce these conditions, we choose values of the chemical potential that favor insertion and drive the system towards progressive densification. To investigate specifically the development of the gel properties under the non-equilibrium conditions created by the precipitation process, we couple the GCMC insertion/removal events to a Molecular Dynamics (MD) simulation. The number of GCMC attempts N_{MC} over the number of MD steps N_{MD} define the kinetic rate $R = N_{MC}/N_{MD}$, i.e., the rate of producing hydrates as determined by the chemical environment. The rate of precipitated particles $\Delta N/\Delta t$ (i.e. successful insertion events in the GCMC) in our *hybrid* simulation scheme will depend on the chemical potential and the kinetic rate as well as on the effective interactions and on the structural organization progressively developed. The MD part of the simulations allows us to follow the aggregation process and the restructuring as the precipitation proceeds.

The nano-scale C-S-H gel is regarded as an aggregated disorder assembly of hydrates, mostly platelets or globules with a typical size of $1 - 30nm$ that have themselves a complex internal layered structure [4, 10, 32, 34, 42, 43]. Because of the high specific area of the hydrates ($\simeq 250m^2/g$ [101]), the characteristics of the surface play an important role in the inter-particle interaction. From the high surface charge (of the order of one electron charge per $0.35nm^2$ for fully ionized C-S-H [49]) and from the presence of divalent counter-ions Ca^{2+}, one obtains a net attraction for the double-layer interactions [49, 50, 54, 102], more than one order of magnitude stronger than the Van der Waals force. Direct force measurements

performed using a C-S-H covered AFM tip and a C-S-H flat surface support the presence of strong non contact attractive forces, arising from the fluctuations of the electrolyte confined between the walls, whose strength increases with the ion coupling, characterized by valence, surface charge and concentration (and in general also dielectric constant and temperature) [53, 54]. The predicted (and measured) interparticle force displays a strong attractive minimum and a secondary maximum, due to the crossover from anionic to cation concentration profiles [47, 54, 103].

Starting from this information, we model C-S-H as a gel of colloidal units of linear size σ, interacting via a short-range attraction and a long-range repulsion with the same characteristics found in AFM experiments and simulations [33, 45, 49, 54]. For simplicity we consider here that the particles are monodisperse in size and spherical in shape. Future work will also include polydispersity and size anisotropy. For the effective interactions, we use a simple form based on a generalized Lennard-Jones (LJ) attraction and a Yukawa repulsion, as often used for colloidal systems

$$V(r) = 4\epsilon \left[\left(\frac{\sigma}{r}\right)^{2\gamma} - \left(\frac{\sigma}{r}\right)^{\gamma} \right] + A\frac{e^{-\kappa r}}{r} \ , \tag{3.2}$$

where r is the inter-particle distance, ϵ is the well depth between two particles with size diameter σ, κ is the inverse screening length and A is a constant [46]. The position of minimum, secondary maximum and strength of the potential are chosen within the range of the experimental values. That is, we have evaluated the range of values, for the parameters of the interaction potential in Eq. 3.2, that are relevant for C-S-H in the early stage of hydration as reported in experiments. The exact characteristics of the interactions will depend on the ionic strength, the pH and the temperature. The screening length can be estimated $\kappa^{-1} \approx 5nm$, for ionic strength smaller than $1mmol/L$ (given by the total ion concentration weighted by the charge number of each ion specie) [53]. In the experiments the position of the attractive minimum and the secondary repulsive maximum of the force are in the range of $[0.5, 1]nm$ and $[1, 4]nm$ respectively [33, 45]. In addition, the strain at rupture of C-S-H has been estimated around 5.5% in atomistic simulations [43]. These facts indicate that the attractive well is fairly narrow. For the range of screening length and ionic strength of interest here, the minimum of the potential (Eq. 3.2) is strongly dictated by the LJ term. Moreover, the potential minimum is at $r_{min} = 2^{1/\gamma}\sigma$, the force minimum at $r_{fmin} = (2+2\gamma/(\gamma+1))^{1/\gamma}\sigma$ and the rupture strain is $(r_{fmin} - r_{min})/r_{min}$. Therefore, we have fixed the LJ exponent to $\gamma = 12$, the screening length to $\kappa^{-1} = 0.5\sigma$ and the particle diameter $\sigma = 1$ in reduced LJ units. We set the reduced temperature in the simulations to $T = 0.15$, such that the maximum force is close to the range of the AFM experimental measurements at room temperature. In the following the time unit for the simulations is the MD unit time $\sqrt{m\sigma^2/\epsilon}$. From the particle number density ρ we estimate the fraction ϕ of the total volume occupied by the colloidal C-S-H hydrates as approximately $\phi \simeq \rho\pi/6\sigma^3$.

The parameters A and ϵ set the repulsion to attraction ratio A/ϵ of the interaction and experimental studies of C-S-H growth kinetics strongly suggest that such ratio is mainly determined by the lime concentration [10, 45], that in general changes with time during cement hydration, therefore changing the effective interparticle potential over time. Here, for simplicity we keep the interaction constant during precipitation and investigate two cases, $A = 12$ and $\epsilon = 2.4$ (S1) and $A = 4$ and $\epsilon = 1.5$ (S2) With these choices we keep the attractive part of the potential fixed and vary the secondary maximum as it happens in the experiments upon increasing lime concentration. Hence, S1 corresponds to lower lime concentration than S2. We use the same screening length κ for both cases because the pH affects more the interparticle forces than the ionic strength [45]. In Fig. 3.1 we have plotted the interaction potentials and the related forces as a function of the distance (S1-continuum line and S2-dashed line).

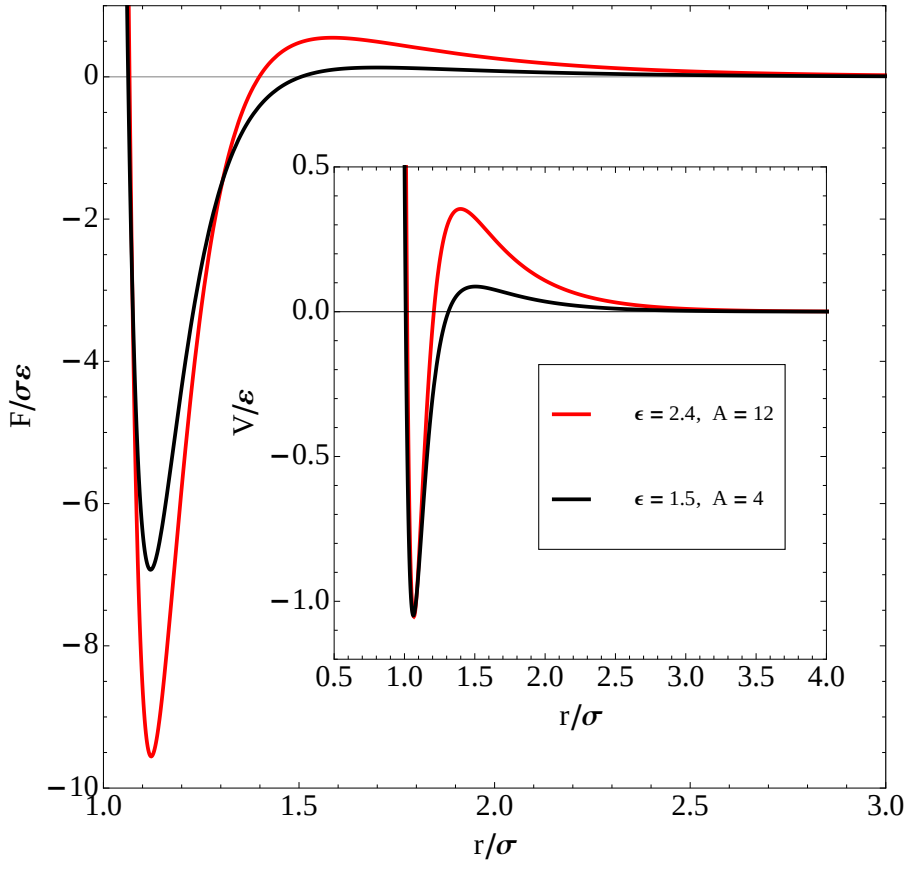

Fig. 3.1 Interparticle forces computed from the choices S1 and S2 for the interaction potential (see inset and Eq. 3.2). The red line (S1) corresponds to low lime concentration in the pore solution and the black-dashed line (S2) corresponds to high lime concentration.

3.2.1 Numerical Simulations

We have performed extensive numerical simulations using the GCMC+MD scheme just described with the interaction potentials S1 and S2. We use a cubic simulation box of size $L = 33.563\sigma$ and periodic boundary conditions. We start with few particles in the simulation box ($\phi = 0.0001$, approximately 32 particle), equilibrated at $T = 0.15$ using MD simulations in the canonical (NVT) ensemble, using a Nosé-Hoover thermostat [76]. A GCMC cycle consists of n_{MC} MC attempts of equal probability to insert or remove a particle. For each insertion/removal attempt a random position/particle is chosen. A successful particle insertion/removal depends on the probability given in Eq. 3.1.

The excess chemical potential values for S1 and S2, for Eq. 3.1, are chosen such that they lead to an equilibrium volume fraction $\phi_{eq} > 0.4$. We used as guide the Table 4.1 of Section 4.5 where the values of the excess chemical potential μ_{exc}/ϵ are listed for equilibrium crystals at $T = 0.15$ and $\phi = 0.6$, as evaluated from free energy calculations described in Section 4.3.2. The values for S1 and S2 are $\mu_{exc}/\epsilon = -0.21$ and $\mu_{exc}/\epsilon = -3.27$ respectively, both for fcc and hcp crystals. Hence, for the precipitation simulation we chose higher values of excess chemical potential, $\mu_{exc}/\epsilon = 3$ and $\mu_{exc}/\epsilon = -1$ for S1 and S2 respectively, to ensure that the system keeps densifying even in out-of-equilibrium conditions.

In every new NVT-MD cycle following a MC one, the velocity of the inserted particle is randomly chosen from a Maxwell-Boltzmann distribution corresponding to $T = 0.15$. We use particle positions computed in the MD to analyze structure and dynamics. We perform a GCMC cycle (each contaning N_{MC} attempts) every $N_{MD} = 100$ MD steps and we investigate the precipitation and the gel development for different R by varying N_{MC}. For these simulations we consider up to 35000 particles and for each set of the parameters we have averaged the results over 5 independently generated samples and used the sample standard deviation to estimate statistical errors. In the following, when not shown in the plots, the error bar is smaller than the symbol size or the line thickness.

We have also investigated the two model systems (S1 and S2) at fix density, i.e. without precipitation. In this case we have performed standard MD simulations in the microcanonical (NVE) and canonical (NVT) ensemble, using a Nosé-Hoover thermostat [76]. Initial configurations of 2048 particles were prepared at different fixed volume fractions by varying the simulation box size, at high relatively temperature ($T = 1$), and slowly cooled to carefully equilibrate them at $T = 0.15$. We have monitored internal energy, kinetic energy and different time correlation functions, that did not show any significant aging up to $\phi \simeq 0.2$. For the largest volume fractions we have used up to 10^7 MD steps for thermalization. For both potentials we used a time step $\delta t = 0.0025$. The same step was used for the standard MD simulations. Most of the simulations were performed with LAMMPS [104].

3.3 Densification: volume fraction and energy

The evolution of the fraction ϕ of the total volume occupied by the colloidal C-S-H hydrates during the GCMC+MD simulations is shown in Fig. 3.2, as a function of the MD time, for respectively S1 (top) and S2 (bottom). The data display a sigmoidal shape and a monotonic dependence on the kinetic rate R: with higher R, the volume fraction attained through precipitation is comparatively higher at the same time. A more detailed analysis, however, allows us to identify some distinctive features. Fig. 3.3 shows the corresponding rate of hydrate volume fraction as a function of time ($\dot{\phi}(t) = d\phi(t)/dt$) during the simulations and indicate clearly an acceleration regime, followed by a deceleration. We can use the maximum of $\dot{\phi}(t)$ to locate the acceleration and deceleration regimes in time. The data indicate that the acceleration and deceleration regimes are qualitatively different between S1 and S2 and depend on R: although precipitation is more effective in S2 where higher volume fractions are reached at earlier times, the acceleration takes place earlier in S1.

In S1 the precipitation rate displays a narrow peak, whose position moves at earlier times upon increasing the kinetic rate. Interestingly, the peak position corresponds to roughly the same volume fraction $\phi_{peak} \simeq 0.15$. We also notice that increasing the kinetic rate R makes the height of the peak decrease slightly, indicating that a slower kinetic rate may allow for a stronger acceleration. Finally in S1 the rate of precipitaton seems to reach a steady state (small but finite) value over the simulation time window. In S2 the precipitation rate displays instead a much wider and smoother maximum, that also moves toward earlier times upon increasing R. Also for S2 the maximum corresponds to reaching roughly the same ϕ for different R, that is $\phi_{peak} \sim 0.28$. The transition into the deceleration regime, in this case, seems to correspond to a complete arrest of the precipitation process within the simulation time window. Overall the data show that the acceleration and deceleration regimes during the hydrate precipitation are ultimately determined by the effective interaction. The maximum precipitation rate is reached at a ϕ_{peak} that is controlled by the effective interactions but is hardly affected by the kinetic rate R: this suggests that the acceleration regime must be strongly correlated to the underlying thermodynamics of the two systems, in spite of the fact that the system is being driven out-of-equilibrium. The deceleration is due to the space filling of the aggregates and not of the single particles: changing interparticle interactions and kinetic rate R may change the morphology of the aggregates and this will change the way they fill the space.

The time dependence of the hydrate volume fraction that we can monitor in the simulations, can be related, at least qualitatively, to the fraction of the clinker that has reacted with water and whose time evolution is measured in the experiments by the degree of hydration [10]. The acceleration and deceleration regimes found in the simulations appear also in the experimental studies of the degree of hydration and have been extensively discussed in the literature [4, 10],

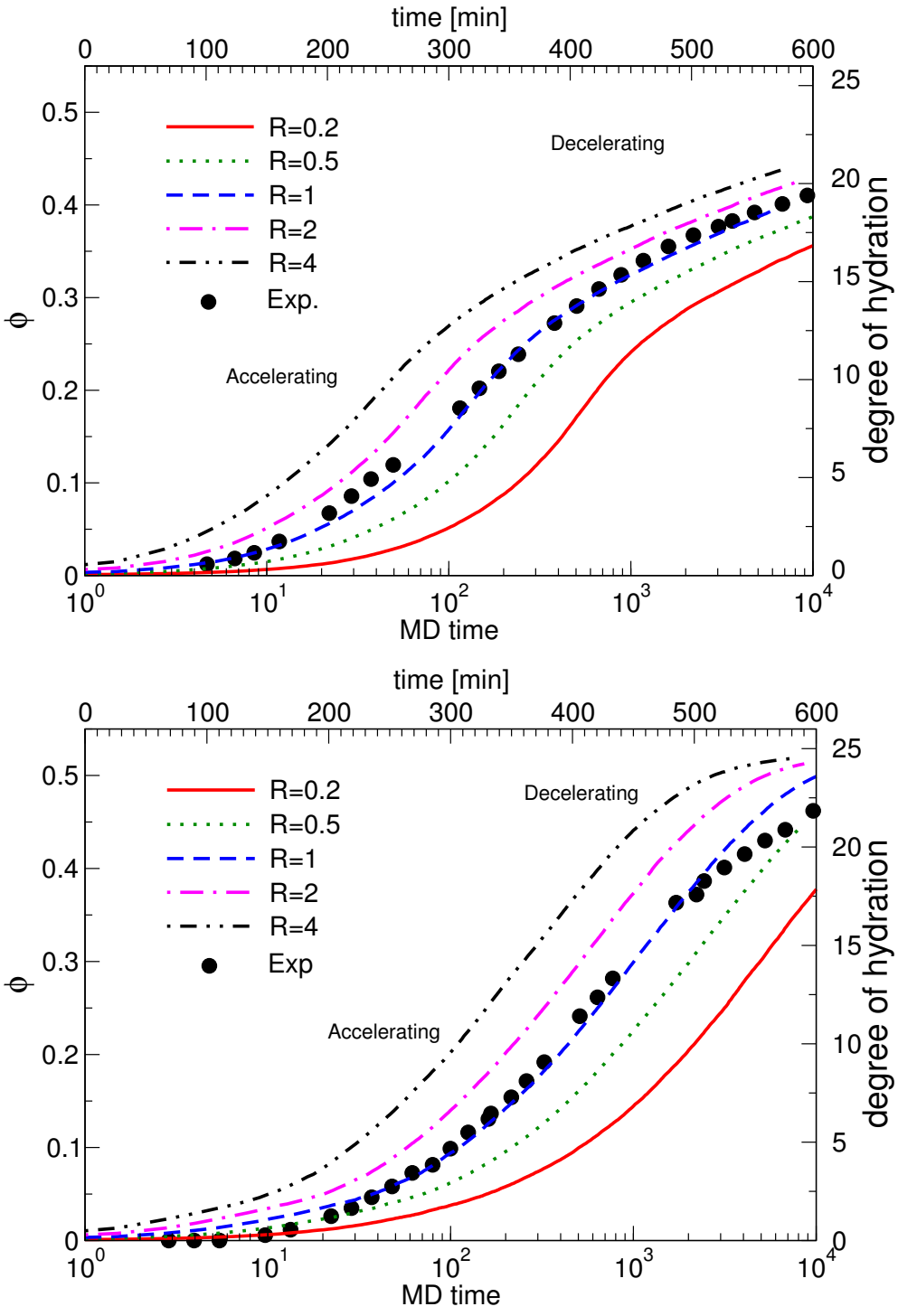

Fig. 3.2 Evolution of volume fraction ϕ for S1 (top) and S2 (bottom) over the simulation time, for different precipitation rates R. The black dots are data from experimental measurements of the degree of hydration in Ref. [10] as explained in the text.

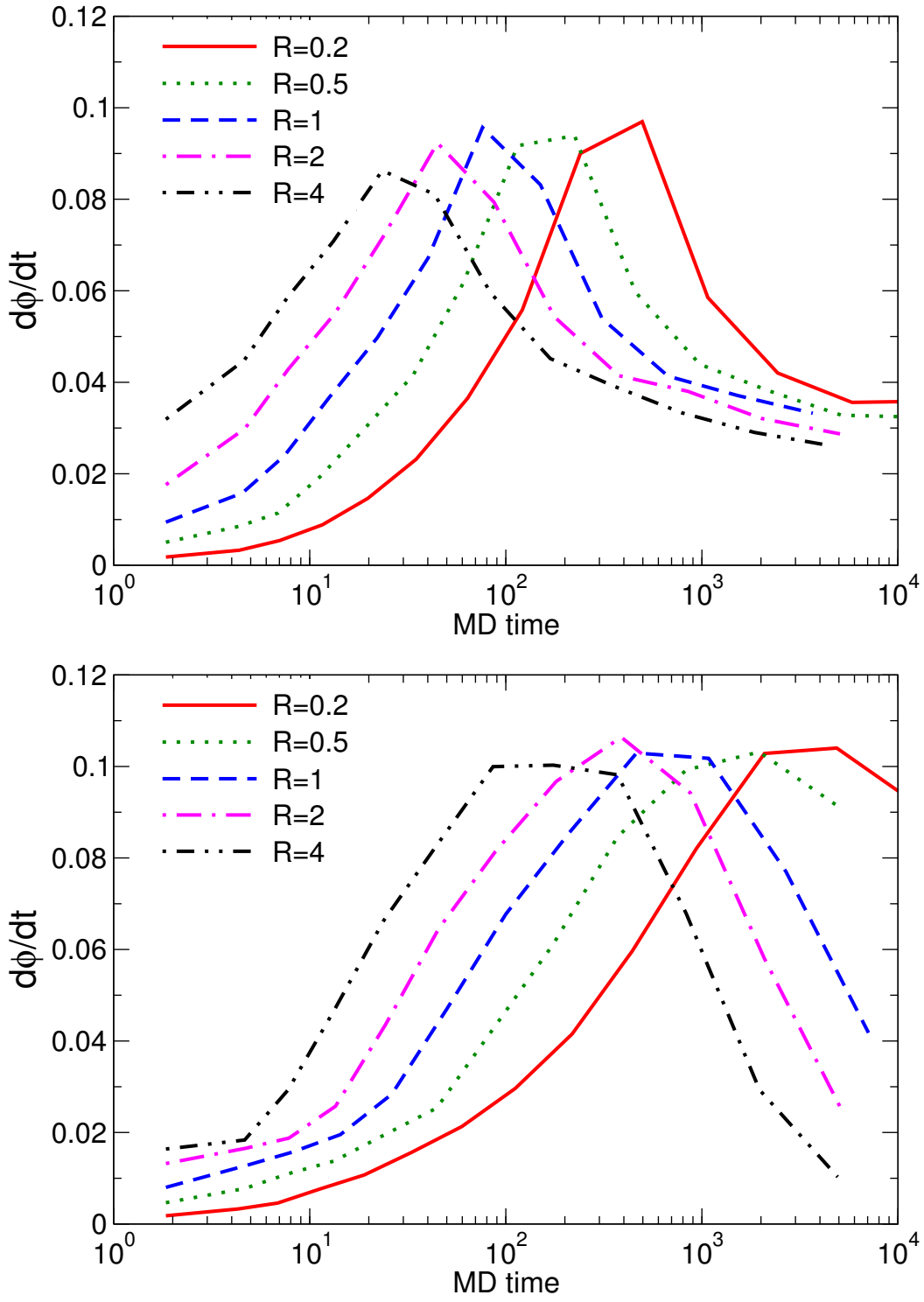

Fig. 3.3 $\dot{\phi}(t)$ as a function of time for S1 (top) and S2 (bottom), for different precipitation rates R.

where they are expected to be related to changes in the gel morphology. The precipitation rate $\dot{\phi}(t)$, quantifying the rate at which hydrates fill the volume, can be related to the heat flow measured via calorimetry during cement hydration and displays indeed its typical non-monotonous time dependence with a well pronounced peak.

We attempt a qualitative comparison with the experimental measurements performed on macroscopic samples, by considering that each Monte Carlo cycle, performed over the duration of the MD simulation time window, does not correspond to an instantaneous process but indeed to the finite time lapse τ_s needed to produce a certain amount of hydrates. Hence an increment in real time of the experiments dt_r should be compared with an increment dt_s/τ_s in the simulation time. The time lapse τ_s is likely to be controlled by ion diffusion in the solution and therefore will increase, as hydration proceeds, with increasing density of ions ρ_i due to the progressive dissolution of the clinker. If for small enough time increments we assume that $\tau_s \propto \rho_i$ and that ρ_i increases linearly with t_s, we obtain that $dt_r \simeq dt_s/t_s$ and that the elapsed real time t_r should be compared with the logarithm of the simulation time lapse $t_r \propto \ln t_s$.

We have used this argument to suitably rescale the real time in comparing the experimental data to the simulation results in Fig. 3.2, where the black symbols have been obtained from data in Ref. [10] (Fig. 7) corresponding to respectively lower (S1) and higher (S2) lime concentration and having a fixed amount of C-S-H nuclei. We use for both S1 and S2 the same arbitrary factors 0.0132 and 2.12 to rescale respectively the x- and y-axis. The figure shows a qualitative agreement between simulations and experiments. Moreover, we find that when changing the effective interactions from S1 to S2 we obtain qualitative changes in the precipitation kinetics and in the gel morphology that are consistent with the changes described in the experiments when increasing the lime concentration: the lower the lime concentration the faster the acceleration onset and the lower the degree of reaction corresponding to the deceleration onset; a higher local volume fraction of the gel corresponds to higher lime concentration, as shown by the simulation data in Fig. 3.2 (lower panel), where the volume fraction of the C-S-H gel in the deceleration period at the end of the simulation window is higher than the one attained in S1 (upper panel).

This comparison is obviously meant to be qualitative, because the experimental data refer to macroscopic samples of C_3S whereas the numerical data refer to nano-scale systems of C-S-H gel in the range of few hundreds of nanometers. Nevertheless, the results obtained for the hydration kinetics and for the dependence on the lime concentration display indeed the same qualitative features reported in the experiments. Moreover this fact supports further the picture that in cement hydration the effective interactions produced in different chemical environments affect

the development of the gel structure and also the evolution of the hydration process.

It is also worth recalling that the simulations performed here and the experimental data of C-S-H precipitation to which we refer are at constant lime concentration and have the same amount of initial C-S-H nuclei in each case, conditions that are not true for cement hydration on the construction sites, but these simplifying assumptions are indeed useful in the scientific investigation to gain insight into the fundamental mechanisms underlying the evolution of the material properties.

To investigate further how different effective interactions in the gel affect the evolution of its physical properties during precipitation, we plot in Fig. 3.4 the potential energy per particle

$$U = \sum_{i=1}^{N} \sum_{\substack{j=1 \\ j>i}}^{N} V(|\mathbf{r_i} - \mathbf{r_j}|)/\mathbf{N} \tag{3.3}$$

as a function of the volume fraction ϕ for different kinetic rates R, computed respectively for S1 (upper panel) and S2 (lower panel). The data show a qualitative difference: for S1 (upper panel) the internal energy displays a non-monotonic evolution upon increasing the volume fraction, whereas for S2 (lower panel), it decreases monotonically with increasing ϕ. One can immediately recognize that these trends are strongly reminiscent of the dependence of the internal energy on volume fraction in absence of precipitation (the asterisk symbols in Fig. 3.4 have been obtained in the standard MD simulations at fixed volume fractions). For S1 we can see that the densification of the system is dominated by the attractive part of the interactions, until the effective longer range repulsion takes over, leading to an increase of the internal energy with volume fraction, and deceleration kicks in. We can see that the decrease of internal energy and the position of its minimum as a function of the volume fraction have a pronounced dependence on the kinetic rate, indicating that the gel structures formed at the same volume fraction must have quite different features depending on R during the acceleration regime. For S2, instead, the decrease of the internal energy with increasing ϕ varies comparatively much less with R, and U keeps decreasing as a function of ϕ even when the rate of densification drops progressively toward zero (see Fig. 3.3). It is worth noticing that for S1 at intermediate volume fractions the internal energy of the systems produced under precipitation is very close to the one of the systems obtained at fixed volume fraction. For S2, instead, the structures formed upon precipitation have an average internal energy that is always significantly different, even at the lowest R investigated here. That is, S2 can be more dramatically driven far from equilibrium upon precipitation, with respect to S1.

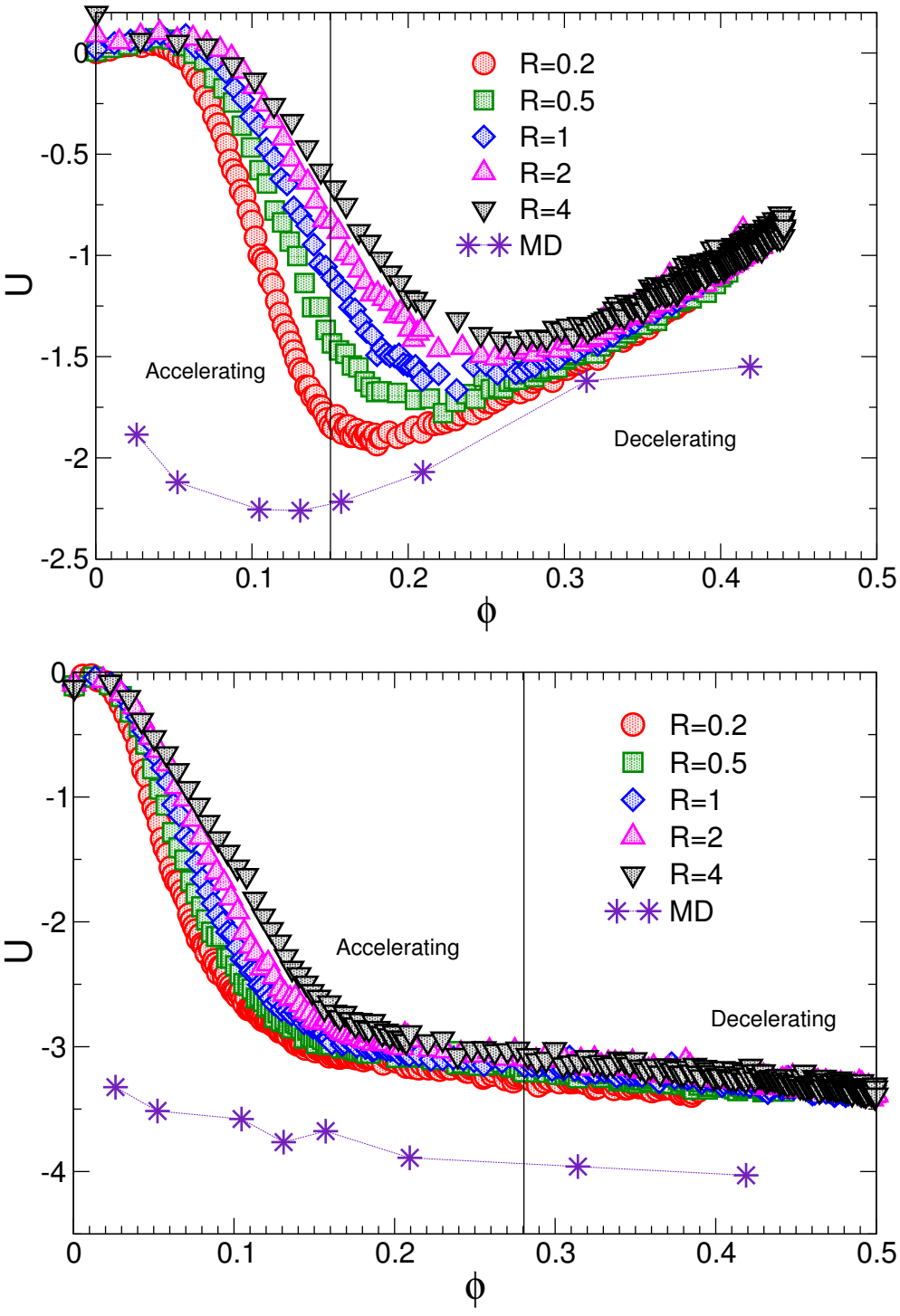

Fig. 3.4 Potential energy per particle as function of volume fraction for S1 (top) and S2 (bottom). The potential energy of the standard MD simulations at fixed ϕ is shown by connected black dots. The perpendicular line represents the volume fraction ϕ of the crossing from acceleration to deceleration.

3.4 Connectivity and local order

We now discuss the evolution of the aggregates morphology (connectivity and local order) during precipitation and, for the two different interaction potentials S1 and S2, we characterize it in terms of the local connectivity of particles, the cluster size distribution during aggregation and the local orientational order.

Having defined a cut off distance r_c as the location of the first minimum of the radial distribution function $g(r)$, we quantify the local connectivity with the fraction of particles $P(n)$ that have n neighbors within a sphere of radius r_c. We compute the number of clusters (per particle) made of s of particles whose relative distance is $r \leq r_c$, that gives the cluster size distribution n_s. The morphology of such clusters is characterized in terms of the gyration radius:

$$R_g^2(s) = \frac{1}{N_s} \sum_{j=1}^{N_s} \left[\frac{1}{s} \sum_{i=1}^{s} (\mathbf{r}_{i,j} - \mathbf{r}_{CM,j})^2 \right] \tag{3.4}$$

where N_s is the total number of cluster of s particles, $r_{i,j}$ is the position of particle i belonging to the cluster j and $\mathbf{r}_{CM,j} = 1/s \sum_{i=1}^{s} \mathbf{r}_{i,j}$ is the position of the center of mass of cluster j. Finally the bond orientational order (BOO) parameters $\bar{q}_{lm}(i)$ enable us to characterize the local packing [105]. The BOO are defined as

$$\bar{q}_{lm}(i) = \frac{1}{N_{b_i}} \sum_{j=1}^{N_{b_i}} Y_{lm}(\hat{\mathbf{r}}_{ij}) \tag{3.5}$$

where N_{b_i} is the number of the bonded neighbors of particle i (using the cut off distance r_c). The unit vector $\hat{r}_{ij}$ specifies the orientation of the bond between particle i and j. The $Y_{lm}(\hat{r}_{ij})$ are the corresponding spherical harmonics. The second-order rotational invariants

$$q_l(i) = \left[\frac{4\pi}{2l+1} \sum_{m=-l}^{l} |\bar{q}_{lm}(i)|^2 \right]^{1/2} \tag{3.6}$$

and the normalized third-order invariants

$$\hat{w}_l(i) = w_l(i) / \left[\sum_{m=-l}^{l} |\bar{q}_{lm}(i)|^2 \right]^{3/2} \tag{3.7}$$

with

$$w_l(i) = \sum_{\substack{m_1,m_2,m_3 \\ m_1+m_2+m_3=0}} \begin{pmatrix} l & l & l \\ m_1 & m_2 & m_3 \end{pmatrix} \bar{q}_{lm_1}(i) \bar{q}_{lm_2}(i) \bar{q}_{lm_3}(i) \tag{3.8}$$

(where the coefficients in the sum are the Wigner 3-j coefficients), can be used to identify specific orientational order. In fact the first non zero $\bar{q}_{lm}(i)$ (apart from

$l = m = 0$) are found in cubically symmetric systems for $l = 4$ and in systems with icosahedral symmetry for $l = 6$. The BOO parameters $(q_4, q_6, \hat{w}_4, \hat{w}_6)$ are generally sufficient to characterize orientational order typical of crystalline solids, colloidal gels and glasses. Table 3.1 shows the values of these two BOO parameters in ideal

Table 3.1 Values of q_4, q_6, $\hat{w}_4$ and $\hat{w}_6$ in perfectly symmetric configurations. The fcc and hcp lattice have twelve neighbors each and the Bernal spiral has six neighbors.

Geometry	q_4	q_6	$\hat{w}_4$	$\hat{w}_6$
fcc	0.190	0.575	-0.159	-0.0132
hcp	0.097	0.484	0.134	-0.0125
Bernal spiral	0.224	0.654	0.08	-0.148
dimers	1	1	0.13	-0.09

situations. For example, dimers have a peak at $q_6 = 1$ whereas the BOO parameter $\hat{w}_6$ allows to distinguish between face sharing tetrahedra that form Bernal spirals and the fcc or hcp crystals [106].

We plot the distributions of cluster sizes n_s in Fig. 3.5, the fraction of n-coordinated particles $P(n)$ in Fig. 3.6, the histograms of q_6 and $\hat{w}_6$ in Fig. 3.7 and 3.8 with the gyration radii of the clusters, for both potentials S1 and S2 and at different volume fractions obtained with the lower kinetic rate $R = 0.2$.

For S1, upon increasing ϕ, the cluster size distribution shown in the top panel of Fig. 3.5 indicates a preferential cluster size of around 7-8 particles, that does not significantly change upon increasing the volume fraction (as also shown by the first moment of the distribution in the inset). This feature is typical of systems with competing short range attraction and long range repulsion, where the competition introduces a well defined modulation length for density fluctuations and hence an optimal linear size for aggregates at different volume fractions [83, 107–109]. A qualitatively similar feature is also observed in numerical studies with the same or similar systems performed at fixed volume fraction, i.e., without precipitation [73, 82, 110, 111] (see Chapter 4). Upon increasing ϕ the distribution extends to clusters of larger size and for $\phi \simeq 0.125$, the majority of the particles belong to one percolated cluster. Nevertheless, we do not observe a power law tail as expected for a random percolation phenomenon [112] and as observed also for S1 in the standard MD simulations performed at fixed volume fraction [73, 110] (see Chapter 4). $P(n)$, the fraction of particles with n neighbors, is shown in Fig. 3.6 (upper panel), as the densification proceeds. The data indicate that the majority of the particles go from having around three-four to six neighbors. This is consistent with the type of local packing also observed in colloidal suspensions with similar interparticle interactions at equilibrium, where particles are arranged on vertices of face-sharing tetrahedra as in Bernal spirals and form elongated aggregates [73, 78, 110]. This is confirmed when we

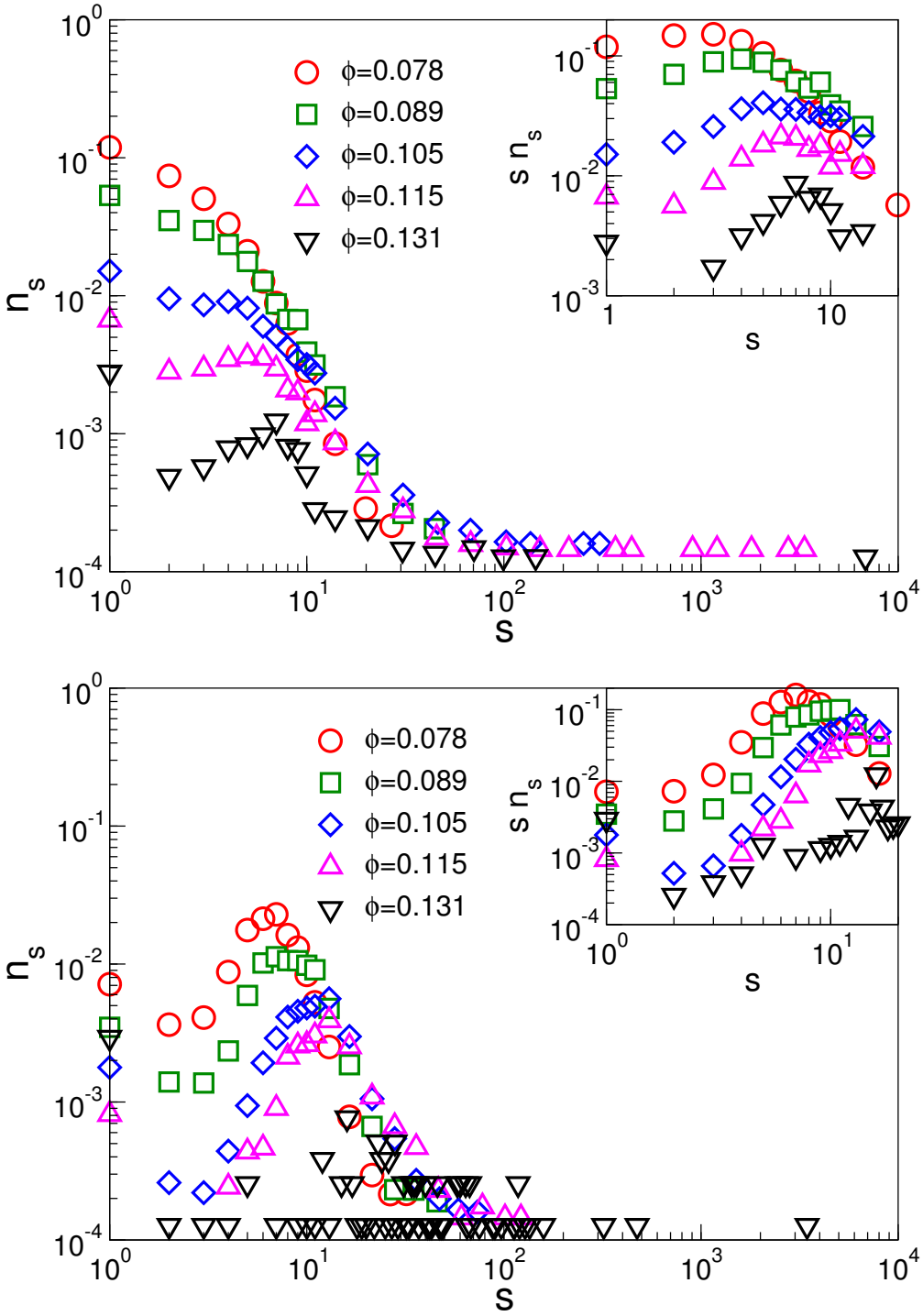

Fig. 3.5 Cluster size distributions n_s for different volume fractions ϕ for S1 (top) and S2 (bottom). In the insets, the first moment of the distribution is shown. The precipitation rate is $R = 0.2$.

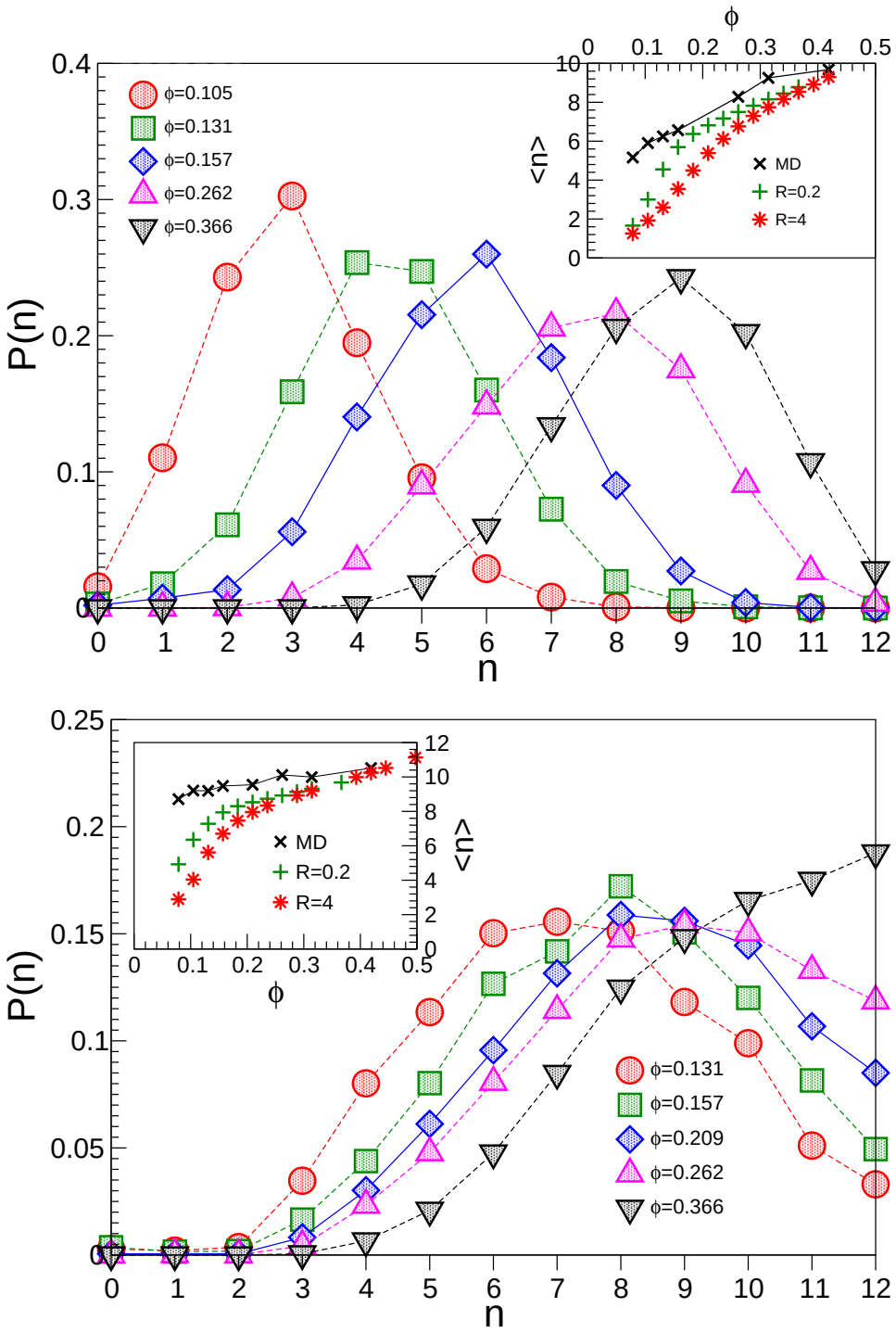

Fig. 3.6 Number of neighbors distribution of volume fractions ϕ for S1 (top) and S2 (bottom). The precipitation rate is $R = 0.2$. The inset shows the average number of neighbors $\langle n \rangle$ as a function of volume fraction ϕ for high ($R = 4$), low ($R = 0.2$) precipitation rate and standard MD simulations at fixed ϕ.

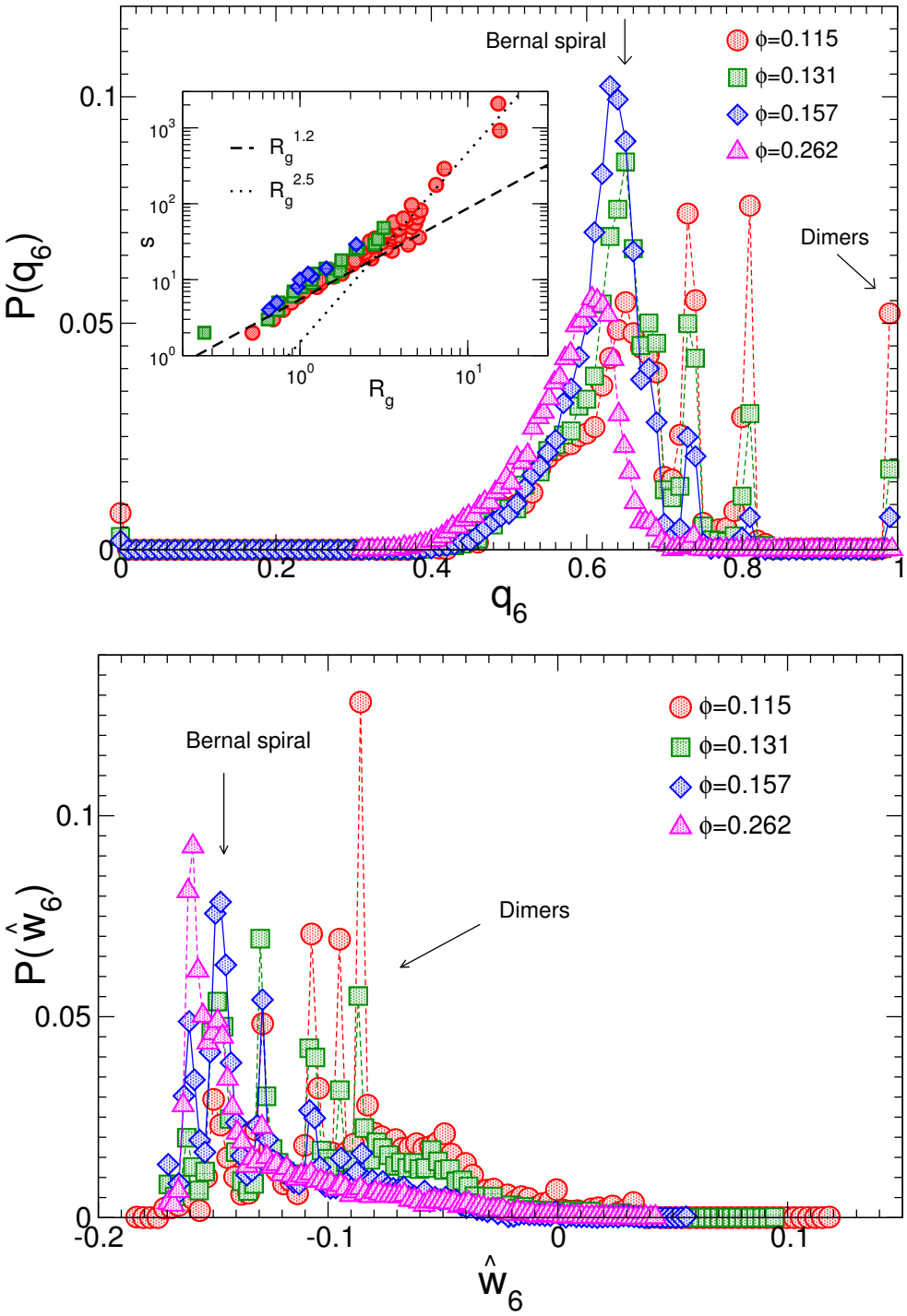

Fig. 3.7 BOO parameters of volume fractions ϕ for S1 potential and low precipitation rate $R = 0.2$, $P(q_6)$ (top) and $P(\hat{w}_6)$ (bottom). Arrows indicate the ideal Bernal spiral values and dimers. The inset shows the cluster size s as a function of the radius of gyration R_g.

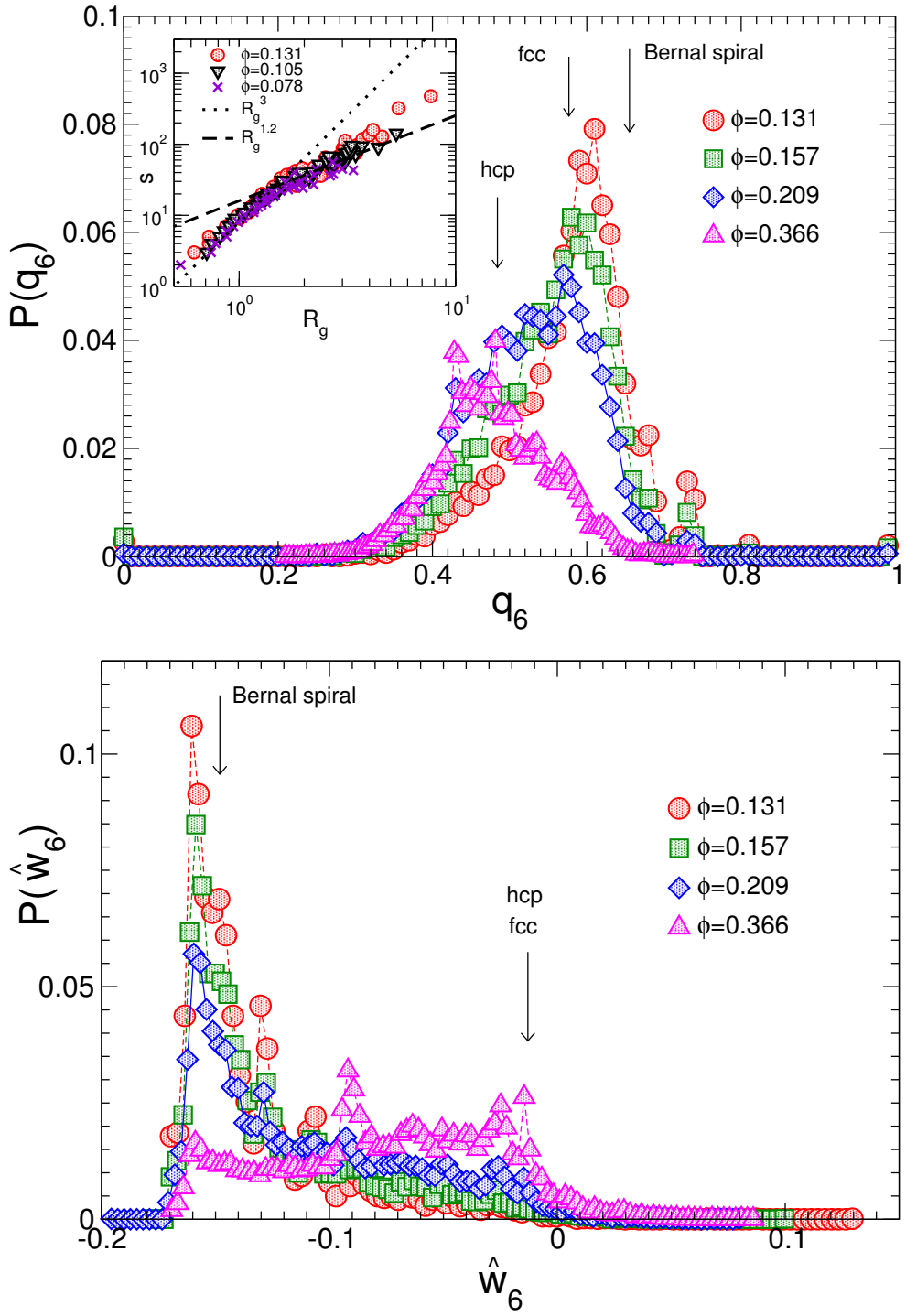

Fig. 3.8 BOO parameters of volume fractions ϕ for S2 potential and low precipitation rate $R = 0.2$, $P(q_6)$ (top) and $P(\hat{w}_6)$ (bottom). Arrows indicate the ideal fcc hcp lattice and Bernal spiral values. The inset shows the cluster size s as a function of the radius of gyration R_g.

analyze the structure obtained at different volume fraction in terms of the BOO parameters. In Fig. 3.7, we plot the distributions of q_6 and $\hat{w}_6$: the data show that, upon increasing ϕ, the amount of particles in dimers and small clusters decreases (i.e., the peak at $q_6 = 1$ disappear for $\phi \geq 0.15$) and the local packing corresponding to face-sharing tetrahedra becomes dominant for volume fractions $0.15 \leq \phi < 0.25$ (see Table 3.1). These findings indicate that ϕ_{peak}, i.e., the position of the maximum of the precipitation rate in Fig. 3.3, corresponds to the volume fraction at which face sharing tetrahedra start to dominate the aggregation and elongated structures (akin to Bernal spirals) can grow. We have also computed the energy per particle of clusters of increasing size s and we found that once the clusters become linear the cluster energy increases linearly with the cluster size, resulting in a flat s-dependence of the energy per particle. The inset of Fig. 3.7 (top) shows the relation between the size s of clusters (in terms of number of particles) and their linear size given by the gyration radius: the slope $\simeq 1.2$ in the log-log plot supports the picture of elongated aggregates growing during the acceleration regime, and finally branching or impinging to form a percolating network (as suggested by the change of slope towards $\simeq 2.5$ upon increasing s and ϕ) [112, 113].

Finally, at $\phi \geq 0.2$ $P(n)$ the number of neighbors increases to eight-nine and the distributions of q_6 parameters display peaks typical of fcc and hcp packing, indicating that Bernal spirals are substituted by fcc or hcp layered structures. These features have a direct correspondence with the different stable phases in the equilibrium phase diagrams [73, 110] (see Chapter 4). In the inset of Fig. 3.6 (upper panel) the average coordination number $\langle n \rangle$ (as computed from $P(n)$) is shown as a function of ϕ. The data refer to GCMC+MD simulations performed with different precipitation rates ($R = 0.2$ and $R = 4$) and to standard MD simulations, performed at fixed volume fraction. They indicate that in the range of volume fractions corresponding to the acceleration regime the evolution of the local packing is indeed significantly affected by precipitation and in particular it is strongly dependent on the kinetic rate R, as suggested by Fig. 3.4: the higher R, the stronger the dependence of $\langle n \rangle$ on ϕ. Increasing R increases the amount of defects and the gel formed at the early stages of the hydration is probably mechanically much weaker [62].

The aggregation and evolution of the morphology of the aggregates upon densification obtained with a kinetic rate $R = 0.2$ in S2 is shown in Figs. 3.5 (lower panel), 3.6 (lower panel) and 3.8. In this case the cluster size distribution displays a well defined peak around $\simeq 10$ particles at low ϕ, but this preferred cluster size moves towards larger values with increasing ϕ (inset of Fig. 3.5). On the other hand, the large clusters remains fairly compact and do not percolate at volume fractions for which in S1 one can clearly observe that all particles belong to a unique cluster spanning the whole system. The fraction of n-coordinated

particles $P(n)$, plotted in Fig. 3.6 (lower panel), shows indeed that upon increasing ϕ the large majority of the particles change from six-seven neighbors to twelve neighbors. The BOO parameters shown in Fig. 3.8 indicate that, for S2, dimers are basically absent at low volume fractions and q_6 and w_6 show the peaks distinctive of face-sharing tetrahedra (in spite of the fact that these are not present in the equilibrium phase diagram in this case, see inset of bottom Fig. 3.6) and of hcp (probably corresponding to icosahedral type of clusters of around ten-thirteen particles) at low ϕ, somewhat similar to S1. Nevertheless, upon increasing ϕ the face-sharing tetrahedra progressively disappear and, around $\phi \simeq 0.28$, hcp and fcc packing become dominant: we observe that clusters coalesce into large crystalline domains (small deviations from the BOO values indicated in the Table 3.1 can be ascribed to defects due to non-equilibrium conditions and finite box size). The inset of Fig. 3.8 (top) showing the size of clusters s as a function of their gyration radius confirms that small clusters are more compact (with respect to S1) and that aggregates grow in an elongated fashion at the beginning of the acceleration regime. The emerging picture is that precipitation drives the systems far from equilibrium but for both S1 and S2 precipitation becomes most successful (and hence the rate of added particles reaches its maximum) at volume fractions at which ordered extended structures can grow and this requires to develop a precise local packing, determined by the specific effective interactions and the underlying thermodynamics. Whereas for S1 the face sharing tetrahedra can arrange into growing elongated aggregates, for S2 the local packing that favors the growth of the aggregates is characterized by twelve neighbors (i.e., hcp and fcc packing). The equilibrium MD configurations for the two potentials S1 and S2 confirm indeed that in S1 for the temperature chosen here $\phi \simeq 0.15$ correspond to the formation of a stable meso-phase, where face-sharing tetrahedra are the building blocks of worm-like aggregates and $\phi \simeq 0.28$ correspond to the appearance of an fcc or hcp crystalline phase in S2.

This picture is consistent with the one proposed by Gartner in Ref. [27]: the acceleration regime results by the nucleation and growth of elongated structures that are locally crystalline or semicrystalline. Precipitation favors defects in the growth of these elongated aggregates, that may branch and/or impinge and percolate into a gel network, progressively filling the space and slowing down the precipitation kinetics. In the case of S2, the acceleration regime proceeds until volume fractions where hcp or fcc packings can grow, corresponding to a gel with thicker branches, i.e., locally denser.

To summarize these results in Fig. 3.10 we show snapshots of S1 (Fig. 9) and S2 (Fig. 10) obtained when $\phi \simeq 0.13$ is reached in the acceleration regime with kinetic rate $R = 0.2$ (top) and $R = 4$ (bottom). We show only bonds between particles to better identify the structure of the gel. Particles with coordination number below six are shown in grey, whereas blue indicates six to nine neighbors

and red is higher than nine neighbors. For S1, for low R most of the particles have around six bonds and they form Bernal spirals branched into a gel network, where branching points can be due to defects (such as impingements) that produce locally higher coordination (i.e., particles with more than nine bonds). In S2 for low R (i.e., slow precipitation) the gel is still made of elongated branched aggregates: the branches of the network are thicker, with nearly hcp or fcc coordinated particles in the inside (red, more than nine bonds) and particles with less bonds (blue) on the surface. In both cases, the branches of the gel become much thinner upon increasing R. Another probably significant insight obtained here is that when the deceleration regime kicks in due to the progressive space filling of the gel hindering precipitation, the underlying thermodynamics favors a different and more compact local packing at the corresponding volume fractions. As a consequence, the densification of the gel steadily proceeds. This might be a key mechanism to reach efficiently the high densities needed to develop the high mechanical strength of C–S–H, in spite of the complex out-of-equilibrium process that drives its assembly [114].

3.5 Conclusions

We have proposed a simple nano-scale model and computational approach for C–S–H precipitation and gelation that allows us to study the evolution of C–S–H gel microstructure under different chemical conditions. The experimental chemical conditions and more specifically the lime concentration determine the effective interactions at the level of the C–S–H hydrate and we have considered two cases corresponding to high and low lime concentration, that can be representative of the early stages of cement hydration. The effect of the hydrate production kinetics is included in the model in terms of the kinetic rate R, which allows us to investigate how the properties of the gels depend on how fast it is formed during precipitation.

The densification curves of the gels obtained in the simulations display the characteristic sigmoid law observed indeed in experiments measuring the degree of hydration over times, characterized by an acceleration and a deceleration regime [4, 32]. While trying to qualitatively compare the results of the model with the macroscopic experiments, we find that also in our simple model a low lime concentration (S1) entails an earlier acceleration and deceleration of C–S–H precipitation, whereas a high lime concentration correspond to a delayed acceleration and a more dramatic deceleration. By analyzing the local packing and aggregation, we find that the acceleration can be directly related to the formation of an optimal local packing that allows for large aggregates to grow and that is controlled by the underlying thermodynamics [73, 110] (see Chapter 4), whereas the deceleration seems to be controlled by the kinetic rate: the faster the kinetics controlling the formation of C–S–H hydrates, the faster the densification and the more dramatic the deceleration in the precipitation process. Due to the effective interactions between hydrates, the growth of the gel happens via the

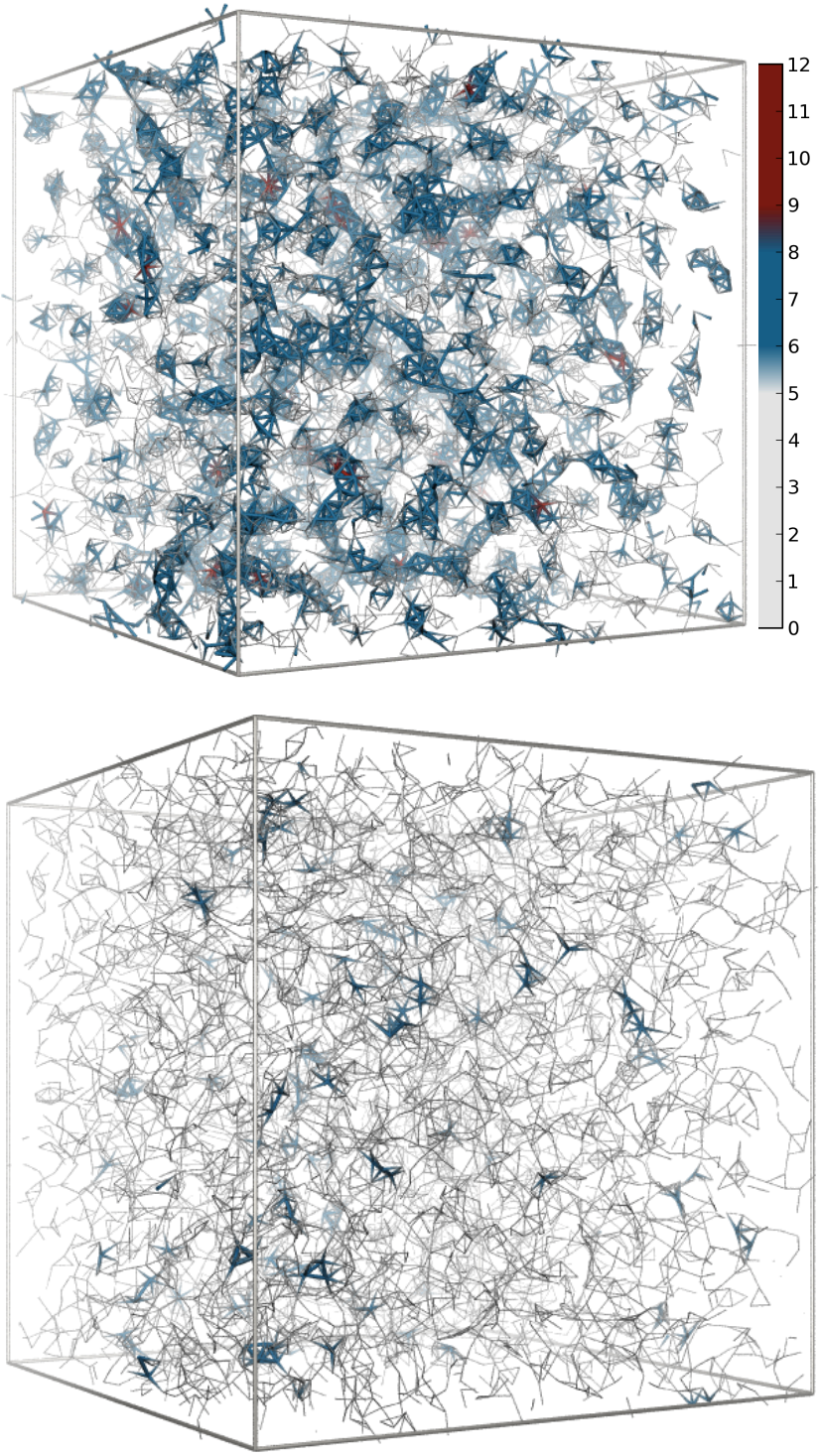

Fig. 3.9 Bond representation of the network obtained respectively at low R (top) and high R (bottom) at $\phi = 0.13$ for S1. The color code corresponds to particle coordination number.

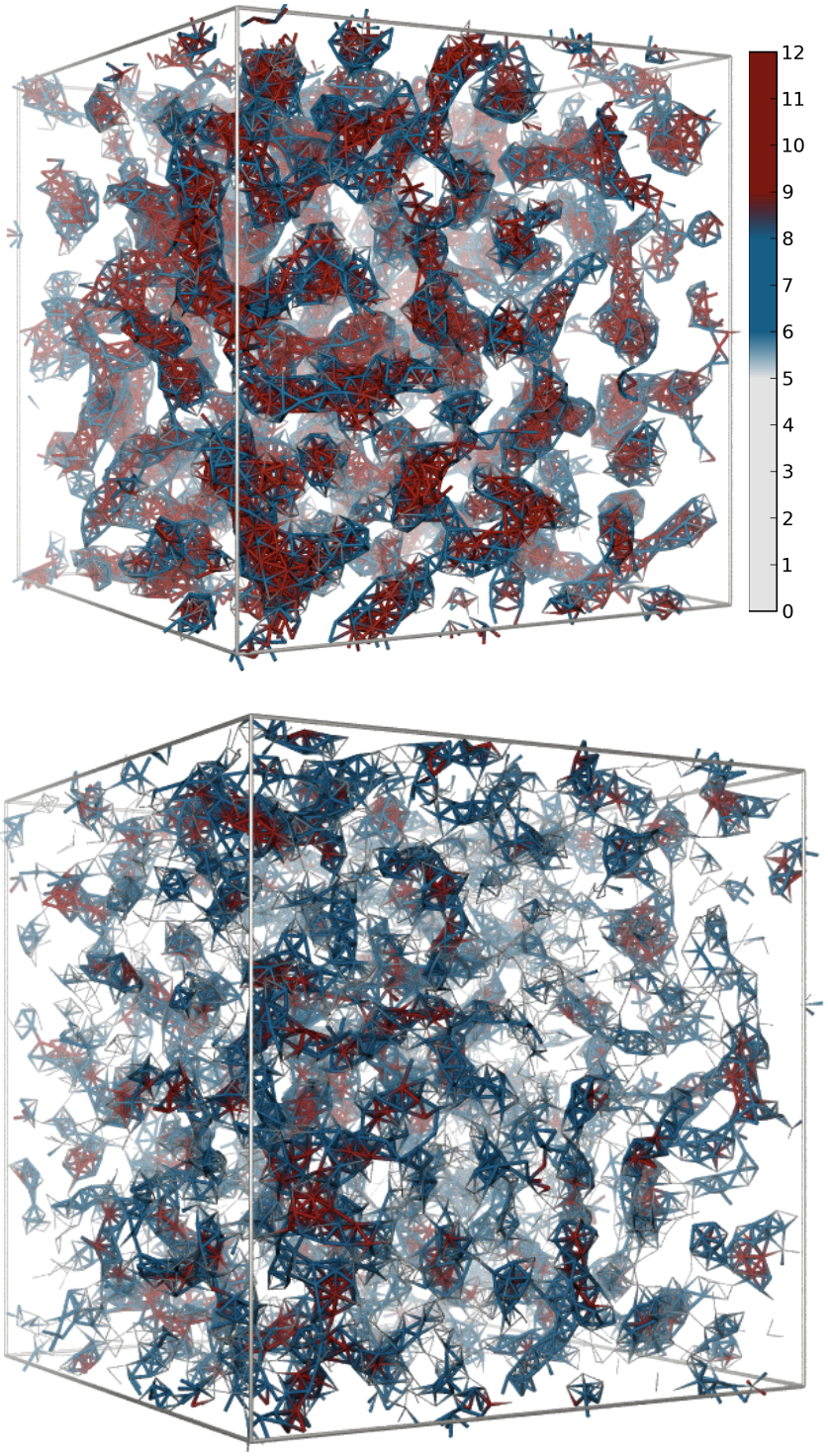

Fig. 3.10 Bond representation of the network obtained respectively at low R (top) and high R (bottom) at $\phi = 0.13$ for S2. The color code corresponds to particle coordination number.

growth of elongated aggregates that are locally crystalline or semi-crystalline and branch (or impinge) as precipitation proceeds. The emerging picture, although the model is based on colloidal units, is consistent with the model proposed in [27]. Furthermore, we find that in the deceleration regime, the system may reach volume fractions where a more compact local packing is thermodynamically favoured and this is key to allow for further and efficient densification of the gel. We also find that upon increasing the lime concentration, the effective interactions change such that the local crystalline packing corresponds to higher local coordination (i.e., fcc or hcp) leading to stronger gels with thicker branches. We identify a range of volume fractions during the acceleration regime where the local packing, the average coordination depends significantly on the kinetic rate: increasing the hydrate production rate in this range of ϕ leads to gels have a local packing that is less compatible with the one dictated by the underlying thermodynamics and this may lead eventually to weaker structures at later times of the hydration.

Developments of this work will include anisotropy of the colloidal units and size polydispersity. This should allow for a more quantitative comparison with experiments, although we do not expect these features to change the qualitative picture obtained here. It is worth noting that the gel structures obtained here display a few main qualitative features in agreement with scattering experiments, SEM/TEM imaging and NMR analysis [10, 22, 34, 96, 97] ranging from the upturn of the scattering intensity at low wave vector, that develops due to the branching of the gel network and remains significant upon increasing the volume fraction to the presence of semi-crystalline anisotropic domains. In Chapter 5 we present and discuss the scattering intensities of the simulated C–S–H gels.

Overall, we propose that the approach developed captures a few basic fundamental mechanisms controlling the development of physical properties in C–S–H gels during cement hydration. It allows to clarify the connection between the hydration kinetics and the changes of the gel morphology. Moreover it allows us to identify specific conditions that can be tuned to control the gel properties under the complex interplay of equilibrium and non-equilibrium conditions that characterize cement hydration. This may suggest new ways to design structural and mechanical features of C–S–H gels or novel more sustainable compounds. Finally our model and approach could be developed further to include heterogeneous nucleation and spatial chemical gradients during precipitation (e.g. due to the cement grain surface) as well as to investigate the aging the gel structure and its effect on the non-linear mechanical response of the material [115].

Chapter 4

Equilibrium and kinetically arrested states by varying short-range attractive and long-range repulsive interactions

The results discussed in the previous chapter have shown that a number of features in the kinetics are affected by the underlying thermodynamics and by different stable phases favoured by the specific effective interactions. We have therefore extensively studied the equilibrium phases and kinetically arrested states for the class of potentials of interest here and in this chapter we discuss the results of this study.

4.1 Introduction

Attractive colloidal suspensions have predictable equilibrium phases but when concentrated or cooled rapidly they form a disordered arrested solid, a gel, able to support weak external stresses. Gel formation under non equilibrium conditions exhibit complex structures and plays an important role in material science as well as in biology, however in many cases the gelation mechanism remains far from understood. When weak long-ranged repulsions are present experiments and simulations have revealed a phase of stable, freely diffusing clusters of particles, and connected solid networks with high degree of orientational ordering [78, 84, 116]. In these cases the long-range repulsion may provide a stabilizing mechanism against bulk phase separation and induce a characteristic modulation length in the gel [82, 117]. The kinetic arrest occurs via the percolation of elongated clusters that grow and branch or impinge into each other [118].

We have seen that the combination of out-of-equilibrium conditions dictated by the chemical environment and of effective interactions as the ones arising from

ion-correlation forces measured in experiments can explain several fundamental features of C–S–H formation during cement hydration. Many features of the gelation described in Chapter 3 arise from the effective interactions combining short-range attraction and long-range repulsion. In the attempt to further elucidate those features, we investigate how the interplay of attraction and repulsion influences the aggregation process as well as the structure of gels in absence of particle precipitation.

More in general, small amount of repulsion can exist in many experimental systems as residual charges onto colloidal particles (or proteins) in suspension. Higher repulsion strengths can instead arise due to ion-ion correlation forces when the particles surfaces are highly charged and the ions are divalent as in the case of C–S–H. Also for clays, as discussed in Section 1.4, the strength of the attracto-repulsive interactions varies with the chemical conditions of formation. Hence, understanding how the interplay between the repulsion and attraction changes the equilibrium and non-equilibrium states at fixed density can be useful to rationalize the behavior of a wide range of systems.

We have performed Molecular Dynamics (MD) and Monte Carlo (MC) simulations of particles, interacting with a short-range attraction and a long-range repulsion, with different strengths repulsion and attraction at various volume fractions. In the following we focus on three cases and analyse the morphology and local packing of the structures.

4.2 Effective Interactions

As discussed in Section 3.2, we consider monodisperse, spherical particles interacting via a short-range attraction and a long-range repulsion. For the effective interactions, we use a simple form based on a generalized Lennard-Jones attractive well (AW) and a Yukawa repulsion as in Eq. 3.2. We chose three different pairs of values for A and ϵ such that in all three cases

$$V_{r_{min}} = -1 k_B T/\epsilon \quad \text{and} \quad V_{r_{max}} \leq -0.5 V_{r_{min}} \tag{4.1}$$

With this choice the attraction well is the same for all cases whereas the height of the repulsive shoulder varies. We have fixed the LJ exponent to $\gamma = 12$ and the screening length to $\kappa^{-1} = 0.5\sigma$ such that the attraction is short-ranged. The three choices for the potential are shown in Fig. 4.1: the black dotted line (LS-lower shoulder) has parameters $A = 4$ and $\epsilon = 1.5$, the green dashed line (MS-middle shoulder) $A = 5.8$ and $\epsilon = 1.7$ and the red solid line (HS-high shoulder) to $A = 12$ and $\epsilon = 2.4$. The HS, MS and LS potentials are truncated and shifted to zero at 4σ. The potentials HS and LS correspond to S1 and S2 potentials of Chapter 3 respectively (see Fig. 4.1 and Fig. 3.1). For comparison we also plotted in Fig. 4.1

the pure attractive well (AW) [119] with the same γ and the interaction potential used in Ref. [84] (HR-highest repulsion).

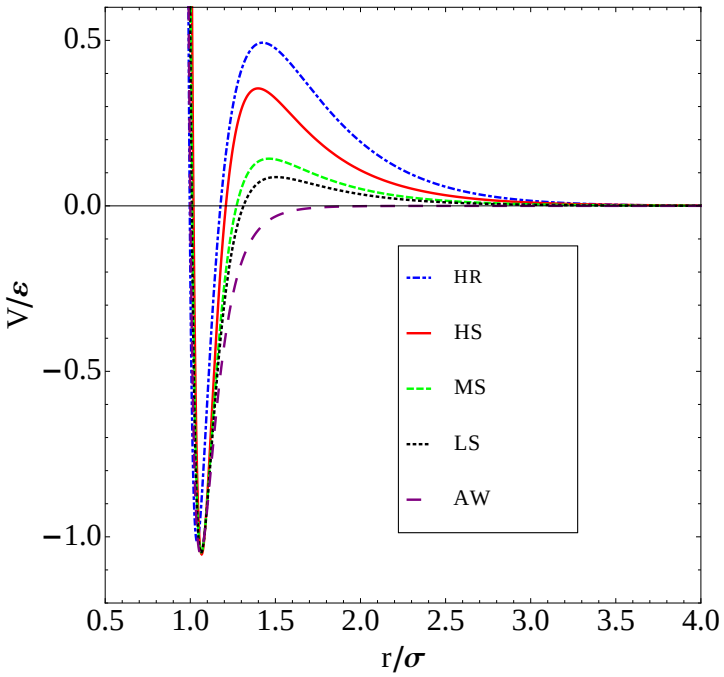

Fig. 4.1 Interparticle potentials with increasing repulsive shoulder. AW corresponds to a generalized Lennard-Jones with exponent $\gamma = 12$. LS corresponds to $A = 4$ and $\epsilon = 1.5$, MS to $A = 5.8$ and $\epsilon = 1.7$, and HS to $A = 12$ and $\epsilon = 2.4$. HR corresponds to the potential of Ref. [84].

As already noted in Section 3.2, for the chosen κ, A and ϵ values, that satisfy Eq. 4.1, the minimum of the potential (Eq. 3.2) is strongly dictated by the attractive LJ term and is at $r_{min} = 2^{1/\gamma}\sigma$. The width of the attraction range increases as the repulsion decreases (e.g. from roughly 0.1σ for the potential HR of Ref. [84] to 0.3σ for the attractive well (AW)). For all cases the attraction is short-ranged. The height of the repulsive shoulders is $\simeq 0.3k_BT$ for the HS, $\simeq 0.15k_BT$ for the MS, $\simeq 0.07k_BT$ for the LS and $\simeq 0.5k_BT$ for the potential HR of Ref. [84]. In the next sections, we show the effect of the increase of the repulsive shoulder of the potential on the microstucture of the equilibrium phases and kinetically arrested states at low volume fraction.

4.3 Numerical Simulations

4.3.1 Molecular Dynamics and Monte Carlo simulations

We have investigated the three potentials (LS, MS, HS) by MD simulations in the microcanonical (NVE) and canonical (NVT) ensemble, using a Nosé-Hoover thermostat [76]. Initial configurations of 2048 and 6912 particles were prepared at different fixed volume fractions by varying the simulation box size (from $L_{box} = 13.679\sigma$ to $L_{box} = 51.706\sigma$), at high relatively temperature ($T = 1$), and slowly cooled to carefully equilibrate them at $T = 0.15$. For the largest volume fractions we have used up to 10^7 MD steps for thermalization. For all potentials we used a time step $\delta t = 0.0025$. All the results presented from the MD simulations are averaged over 5 independent samples. From the particle number density ρ we estimate the fraction ϕ of the total volume occupied by particles as approximately $\phi \simeq \rho\pi/6\sigma^3$. Most of the simulations were performed with LAMMPS [104]. We have monitored internal energy, kinetic energy and different time correlation functions, that did not show any significant aging up to $\phi \simeq 0.15$. In all cases for $\phi \gtrsim 0.15$ the thermalization requires increasingly longer times and in the simulations we obtained arrested states that depend on the thermalization protocol and on the system size.

In order to sample more efficiently the equilibrium states, we have performed parallel tempering Monte Carlo (MC) simulations [120]. We simulated $M = 40$ replicas of the same system at different temperatures $T_1, \ldots, T_M$. The replicas' temperatures range from $T_1 = 0.15$ to $T_M = 0.7$ in such a way that the two adjacent temperatures differ by a factor of $T_{i+1}/T_i = 1.04$. Replicas are either randomly initialized or initialized from the MD configurations equilibrated at the corresponding temperatures. For each replica we perform the same number of MC steps at a given temperature using MC moves of individual particles as well as cluster moves, i.e., translational moves of all the particles that belong to the same cluster. Cluster moves that result in cluster fusion are rejected.

We attempt to swap particle configurations between two adjacent replicas i and $i + 1$ with the prescribed Metropolis-based probability [120],

$$P = \min\left\{1, \exp\left[(T_i^{-1} - T_{i+1}^{-1})(U_i - U_{i+1})\right]\right\}, \tag{4.2}$$

where T_i and T_{i+1} are the temperatures and U_i and U_{i+1} are the total potential energies of the two replicas. In order to achieve sufficient swapping acceptance between replicas, the average energy difference between the adjacent replicas $U_i - U_{i+1}$ need to be comparable to energy fluctuations. Since expected energy U_i scales linearly with the number of particles N, whereas the corresponding fluctuations as $\sqrt{N}$, the larger the number of particles the smaller the temperature difference between the adjacent replicas needed to be, i.e., more replicas are needed to cover the desired temperature range. Therefore, for MC we have used a smaller

number of particles ($N = 500$). This enables for a successful replica swapping with acceptance probabilities of around 0.10–0.3, which is considered as an optimal choice [121]. For MC simulations at between 20–80 $\times 10^6$ steps, the first half was used for equilibration and the second half for sampling.

4.3.2 Free energy calculations

Having detected fcc or hcp crystalline order in the MD simulations, we have computed the free energy of these crystalline phases by thermodynamic integration. We have used a reversible path between the solid obtained in the simulations and an ideal Einstein crystal with the same structure [122, 123]. The ideal Einstein crystal consists of particles attached to their lattice positions via harmonic springs of constant Λ_E, and its free energy $A_0(T, \rho)$ can be analytically evaluated. The free energy difference, $\Delta A_1(T, \rho)$, between the ideal Einstein crystal and the interacting Einstein crystal (in which particles interact through the interparticle potential used in the simulations) can be expressed as

$$\Delta A_1(T, \rho) = U_{\text{lattice}} - N k_B T \log\langle \exp[-\beta(U_s - U_{\text{lattice}})]\rangle, \tag{4.3}$$

where U_{lattice} is the potential energy of the perfect lattice and U_s the potential energy of the solid obtained in the simulations with the given interparticle interactions. The free energy difference between the interacting Einstein crystal and this solid $\Delta A_2(T, \rho)$ can be computed as

$$\Delta A_2(T, \rho) = -\int_0^{\Lambda_E} \left\langle \sum_i^N (r_i - r_{i,0})^2 \right\rangle d\Lambda'_E, \tag{4.4}$$

where the integrand is the mean square displacement of particles from their lattice positions. To calculate $\Delta A_1(T, \rho)$ and $\Delta A_2(T, \rho)$, we performed canonical (NPT) MD simulations of 2048 particles at zero pressure and different temperatures using LAMMPS [104, 124]. From $\Delta A_1(T, \rho)$ and $\Delta A_2(T, \rho)$, we get the free energy of the solid obtained in the simulations as

$$A_s(T, \rho) = A_0(T, \rho) + \Delta A_1(T, \rho) + \Delta A_2(T, \rho). \tag{4.5}$$

Additional thermodynamic information has been obtained by measuring the chemical potential using the Widom insertion method [125]. The total chemical potential μ of interacting particles is composed of two parts,

$$\mu = k_{\text{B}} T \log \Lambda^3 \rho + \mu_{\text{exc}}, \tag{4.6}$$

with the first term corresponding to an ideal gas contribution of density ρ, and μ_{exc} is the excess part due to the presence of particle-particle interactions. For the

purpose of test particle insertions, we used particle configurations obtained by the MC simulations. From the resulting potential energies U_i of the inserted particle at random positions (2×10^6 per sampled snapshot), the excess chemical potential can be evaluated from

$$\mathrm{e}^{-\beta\mu_{\mathrm{exc}}} = \langle \mathrm{e}^{-\beta U_i} \rangle, \tag{4.7}$$

where $\langle \ldots \rangle$ denotes the average over all particle positions over the whole sampled trajectories.

4.3.3 Grand Canonical simulations

As already mentioned, in cases of low ϕ we obtain persistent clusters whose nature, stable or metastable, is difficult to discriminate. To elucidate this point we have also evaluated the cluster size distribution by free energy calculation using Grand Canonical Monte-Carlo (GCMC) simulations. We followed the same procedure introduced to investigate micelle formation in Refs [126, 127].

In an approximation of a dilute gas of clusters, such that interactions between the clusters are negligible, we can decompose the total partition function of the system into contributions of individual clusters

$$Q = \prod_{s=1}^{\infty} \frac{Q_s^{N_s}}{N_s!} = \prod_{s=1}^{\infty} \frac{(V/\Lambda^3)^{N_s}}{N_s!} \Big(\frac{Q_s}{Q_1}\Big)^{N_s}, \tag{4.8}$$

where N_s is the number of clusters with size s, V is the volume of the system, Q_s is the single cluster (of size s) partition function, and Λ the de Broglie length. Upon minimizing the total free energy $-k_B T \log Q$ with respect to cluster size N_s, with the constraint of total number of particles $\sum_{s=1}^{\infty} sN_s = N$, one obtains the number of clusters of size s in equilibrium,

$$\frac{N_s}{V}\Lambda^3 = \Big(\frac{N_1}{V}\Lambda^3\Big)^s \frac{Q_s}{Q_1}. \tag{4.9}$$

The related cluster size distribution is therefore $n_s = N_s/N_{\mathrm{cl}}$, where $N_{\mathrm{cl}} = \sum_{s=1}^{\infty} N_s$ corresponds to the total number of clusters in the system. This yields

$$n_s = p_1 \, \mathrm{e}^{\beta\tilde{\mu}(s-1)} \frac{Q_s}{Q_1}, \quad \text{where} \quad \mathrm{e}^{\beta\tilde{\mu}} \equiv \Lambda^3 \rho \frac{N_1}{N}, \tag{4.10}$$

with $\rho = N/V$ being the particle number density. The parameter $\tilde{\mu}$ plays the role of the chemical potential in a diluted system with $\beta = 1/k_{\mathrm{B}}T$ and the parameters $p_1 = N_1/N_{cl}$ and $\tilde{\mu}$ are fixed by the two constraints

$$\sum_{s=1}^{\infty} n_s = 1, \quad \text{and} \quad N_{\mathrm{cl}} \sum_{s=1}^{\infty} s n_s = N. \tag{4.11}$$

The ratio of partition functions Q_s/Q_1 is computed in the GCMC simulations. As in the MC simulations, we implemented a parallel tempering scheme, but limited the simulations to one single cluster size by rejecting all the moves that would break the cluster. That is, besides particle translation moves as in usual MC, we also performed insertions and deletions of particles according to the standard GCMC scheme with the restriction to preserve a single cluster size in the system, i.e.,only insertions within the attractive wells of particle interactions were attempted. Hence, the volume in the standard GCMC acceptance rule for the particle insertion here is the total volume of all attractive wells. In order to preserve detailed balance, in case of overlap of k attractive wells of neighboring particles at the location of an insertion attempt, the standard insertion acceptance probability needs to be corrected (multiplied) by a factor $1/k$. During the simulation, we were sampling the probability distribution of the single cluster size $P(s)$, which is related to the ratio of the partition functions as

$$\frac{Q_s}{Q_1} = \frac{P(s)}{P(1)} \, \mathrm{e}^{-\beta \mu_{\mathrm{GC}}(s-1)}, \tag{4.12}$$

where μ_{GC} is an arbitrary value used in the simulations for the chemical potential, which does not affect the ratio Q_s/Q_1 but it influences the sampling efficiency. The chemical potential μ_{GC} used in GCMC should not be confused with $\tilde{\mu}$ in Eq. (4.10). In order to further increase sampling efficiency, we have implemented the standard Umbrella Sampling scheme where we sample at once a cluster of only two possible sizes, s and $s+1$. The results for all cluster sizes are obtained by stitching together the simulations results of different cluster sizes [127].

The parallel tempering MC simulations, the free energy calculations and the grand canonical simulations were performed in collaboration with Dr. Matej Kanduc (Freie-Universitaet Berlin), Ms Lunna Li, Dr. Jure Dobnikar and Prof. Daan Frenkel (University of Cambridge).

4.4 Aggregation at low volume fraction

For the three different interaction potentials LS, MS and HS, we have characterized the aggregates morphology in terms of the cluster size distribution, the radius of gyration, the asphericity, the pair distribution function and the local bond orientational order. In the following we define the different quantities and discuss the results obtained.

4.4.1 Definitions

The radial distribution function $g(r)$ describes the spatial correlations in the particle density as a function of the relative distance

$$g(r) = \frac{1}{4\pi r^2 N\rho} \left\langle \sum_i \sum_{j\neq i} \delta(r - r_{ij}) \right\rangle, \tag{4.13}$$

where N is the number of particles and ρ the number density. Particles that are mutually separated by $r \leq r_c$, where r_c is distance of the minimum followed by the first peak in $g(r)$, form a cluster. As the aggregation proceeds, we sample the cluster size distribution in terms of the number of clusters n_s (per particle) composed of s particles. To characterize the morphology of such clusters, we determine the gyration tensor

$$S_{ab}(s) = \frac{1}{N_s} \sum_{j=1}^{N_s} \left[\frac{1}{s} \sum_{i=1}^{s} (r_a^i - r_{a,CM})(r_b^i - r_{b,CM}) \right] \tag{4.14}$$

where N_s is the total number of cluster of s particles, r_a^i is the a_{th} coordinate of the position vector $\mathbf{r^i}$ of the i_{th} particle belonging to the cluster j and $r_{a,CM} = 1/s \sum_{i=1}^{s} r_a^i$ is the a_{th} coordinate of the position of the center of mass of cluster j. The gyration radius is defined as the sum of the eigenvalues of the gyration tensor:

$$R_g^2(s) = \text{Tr } S_{ab}(s) = \lambda_1 + \lambda_2 + \lambda_3 \tag{4.15}$$

where the eigenvalues of $S_{ab}(s)$ are sorted in descending order, i.e., $\lambda_1 \geq \lambda_2 \geq \lambda_3$. This definition of gyration radius is equivalent to Eq. 3.4. In addition, the asphericity parameter

$$b = \lambda_1 - \frac{1}{2}(\lambda_2 + \lambda_3). \tag{4.16}$$

measures the deviation of the cluster shape from the spherical symmetry ($b = 0$).

Finally the bond orientational order (BOO) parameters $\bar{q}_{lm}(i)$ [105], defined in Section 3.4, enable us to characterize the local packing.

4.4.2 Clusters morphology and local packing at low volume fraction

We compare the morphology and local packing of the clusters detected in the MD and MC simulations upon decreasing the strength of the repulsive shoulder, i.e. changing the particle interactions from HS to MS and LS. The cluster morphology is investigated by the cluster size distribution n_s, the normalized asphericity b/R_g^2 and the gyration radius R_g, and the local packing by the pair distribution function

$g(r)$ and the bond orientational parameters BOO ($\hat{w}_6$, $\hat{w}_4$).

In Fig. 4.2, the distributions of cluster sizes n_s as obtained from the single-cluster GCMC simulations described in Section 4.3.2 for cluster sizes up to $s = 70$ are shown for HS, MS and LS potentials at $T = 0.25$. The inset of Fig. 4.2 displays the cluster-size distribution n_s from the MD simulations at larger systems at $\phi = 0.052$ and same temperature. For HS, the distribution n_s displays a peak indicating that there is a well defined characteristic cluster size, corresponding to $s \sim 7$ and larger clusters are much less probable. The cluster size distribution for MS displays the same behavior but the peak is of $s \sim 18$ and for $s > 40$ the probability of finding larger clusters starts to increase again. The n_s of LS, instead, has no distinct peak and the probability increases with the cluster size showing that the most probable cluster size is only limited by the system size. The size distributions in the inset show more clearly the characteristic peaks of HS and MS and confirm the absence of a characteristic cluster size for LS. The cluster size distribution of LS in the inset is quite flat for $10 \lesssim s \lesssim 100$. In the case of HS, the equilibrium phase of clusters with a well defined typical size is consistent with the idea, associated to microphase separation, that the competition between attractive and repulsive interaction induces a typical modulation length [117, 128, 129], as mentioned in Section 2.2. By decreasing the repulsive shoulder, moving from HS to MS and finally to LS, the scenario of microphase separation seems to disappear.

We have also analyzed the shape of clusters at low ϕ, by extracting the normalized asphericity parameter b/R_g^2, that quantifies the deviation from a spherical shape, from the gyration tensor. b/R_g^2 is plotted as a function of s for HS, MS and LS at $\phi = 0.052$ and $T = 0.15$ in Fig. 4.3. At this volume fraction we have used $N = 2048$ and $L_{box} = 27.35\sigma$. For HS, the clusters start to grow in a non-spherical way for $s \gtrsim 10$, as it is shown by the steep increase of the asphericity parameter. The same occurs for MS, however the asphericity parameter increases rapidly only for $s \gtrsim 20$ and overall the clusters are much larger than in the HS case. In all cases $R_g \ll L_{box}$ hence these finding are not an effect of the system size. Overall for HS and MS, the larger the clusters the less compact they are. The increase of b/R_g^2 seems to saturate around $s \gtrsim 30$, but this is probably due to the fact that the linear size of the simulation box at $\phi = 0.052$ is $L_{box} = 27.35\sigma$. The clusters obtained with LS are, instead, larger and more compact and only for $s \gtrsim 100$ there is a tendency for less compact clusters. Overall, we can conclude that the size for which the clusters start to display a significant asphericity increases, and becomes controlled by the size of the simulation box, by decreasing the repulsion strength with respect to attraction.

Upon increasing ϕ, the morphology of the clusters changes significantly for the three interaction potentials. In Fig. 4.4 we plot the cluster size s as a function of the gyration radius R_g at $T = 0.15$ for HS (top) and LS (bottom). The data

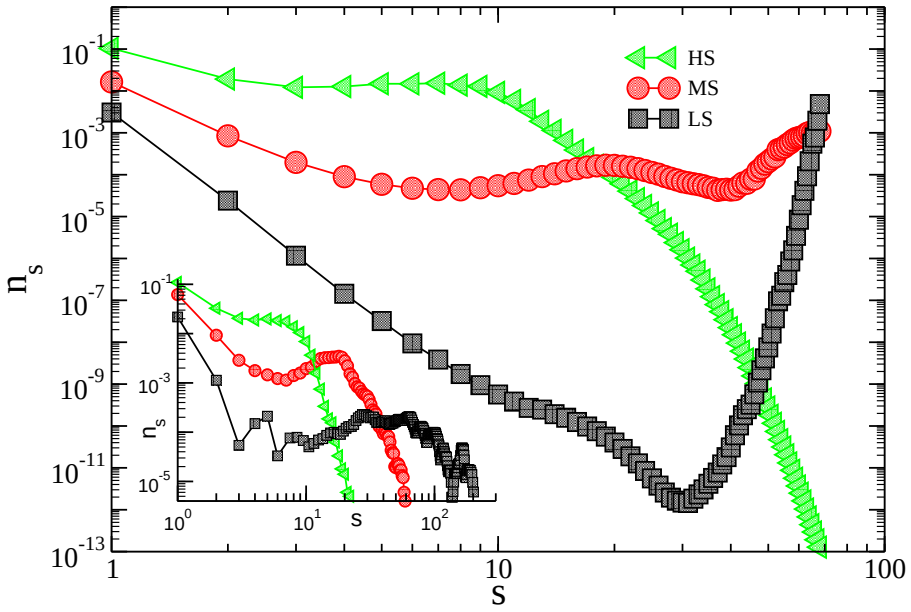

Fig. 4.2 Cluster size distribution n_s as found from the GCMC free energy calculation of the single clusters (Eq. 4.12) at $T = 0.25$ for HS (triangles), MS (circles) and LS (squares). The inset displays the cluster size distribution the same T for $\phi = 0.052$ as computed from the MD simulations of larger systems (6912 particles). Solid lines are a guide to the eye.

for HS indicate that, at low ϕ, $s \propto R_g^3$ for small clusters (i.e. $s \lesssim 10$), whereas $s \propto R_g^{1.25}$ for larger clusters. This suggest that, at low volume fraction, compact stable clusters of typical size $s \simeq 10$ form. This finding is consistent with the observation of a peak at $s \simeq 10$ in n_s in Fig. 4.2 and with the corresponding value of the gyration radius $R_g \simeq 1$. Upon increasing the volume fraction the clusters grow into elongated structures (i.e. $s \propto R_g^{1.2}$ indicates linear growth) up to a size $s \approx 50$, consistent with the results obtained from the asphericity parameter shown in Fig. 4.3. The inset in Fig. 4.4 (top) shows a snapshot of the MD simulations with the HS potential at $\phi = 0.079$ and $T = 0.15$. For the MS potential, the dependence of the cluster size on the gyration radius is quite similar to the one obtained with HS. Initially spherical clusters grow in an elongated shape as ϕ increases. However, as the repulsion strength decreases, from HS to MS, the crossover from the spherical to the elongated growth occurs at larger cluster sizes. Upon decreasing further the repulsion, in the LS case, the clusters remain compact for even larger sizes. For $s > 100$, the LS clusters are somewhat elongated and the crossover size between spherical and elongated cluster is now much less pronounced, suggesting that for LS the elongated clusters are the result of kinetics rather than being thermodynamically favoured. This is shown in Fig. 4.4 (bottom) where the cluster size s as a function of R_g is plotted for LS. The inset of Fig. 4.4 (bottom) shows elongated crystalline clusters obtained in the MD simulations with LS at the same ϕ and T as for HS (top). HS and LS clusters both grow in a linear

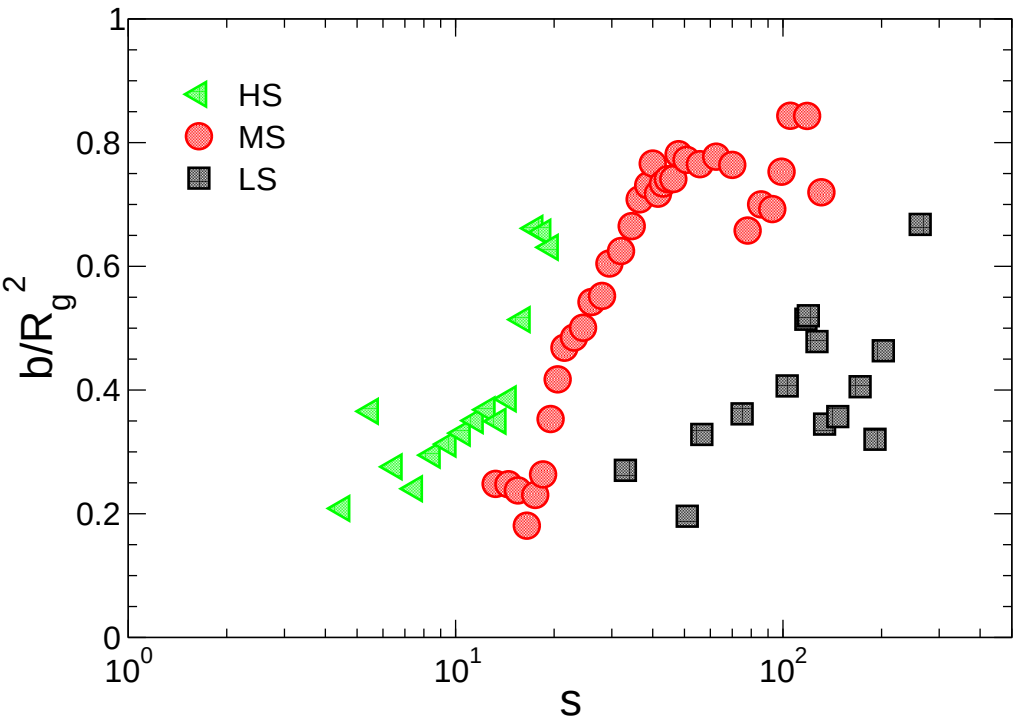

Fig. 4.3 Normalized asphericity b/R_g^2 as a function of the cluster size s for $\phi = 0.052$ at $T = 0.15$ for HS, MS and LS.

fashion at the same ϕ and T. HS develops many, small and thin fibrils whereas LS few, large and bulky ones.

By reducing the strength of the repulsion with respect to the attraction in the interaction potential, not only the cluster size and shape but also the particle packing inside the aggregates changes. To quantitatively analyze this effect, we plot the radial distribution function in Fig. 4.5 for HS, MS and LS at $\phi = 0.079$ and $T = 0.15$. The peaks of $g(r)$ give quite precise indications of the changes in the local packing. HS and MS show similar peaks, whereas for LS the second peak is at shorter distances and the third peak is split as it is typical for fcc and hcp crystals, indicating that the clusters formed with LS display significant local crystalline order even at such low volume fraction.

We have further characterized the local order in terms of different BOO parameters. In Fig. 4.6, we plot the contour plots of ($\hat{w}_6$, $\hat{w}_4$) obtained from the distributions $P(\hat{w}_6)$ and $P(\hat{w}_4)$, computed at volume fraction $\phi = 0.079$ (top) and $\phi = 0.052$ (bottom) and $T = 0.15$ for HS (left) and LS (right). The color code indicates the density of particles displaying the corresponding values of $\hat{w}_6$ and $\hat{w}_4$. These contour plots allow us to distinguish between the fcc, hcp crystals and the Bernal spiral (BS). For the HS, the clusters have local packing similar to the Bernal spiral, which is consistent with the results reported in other studies [84, 130]. LS

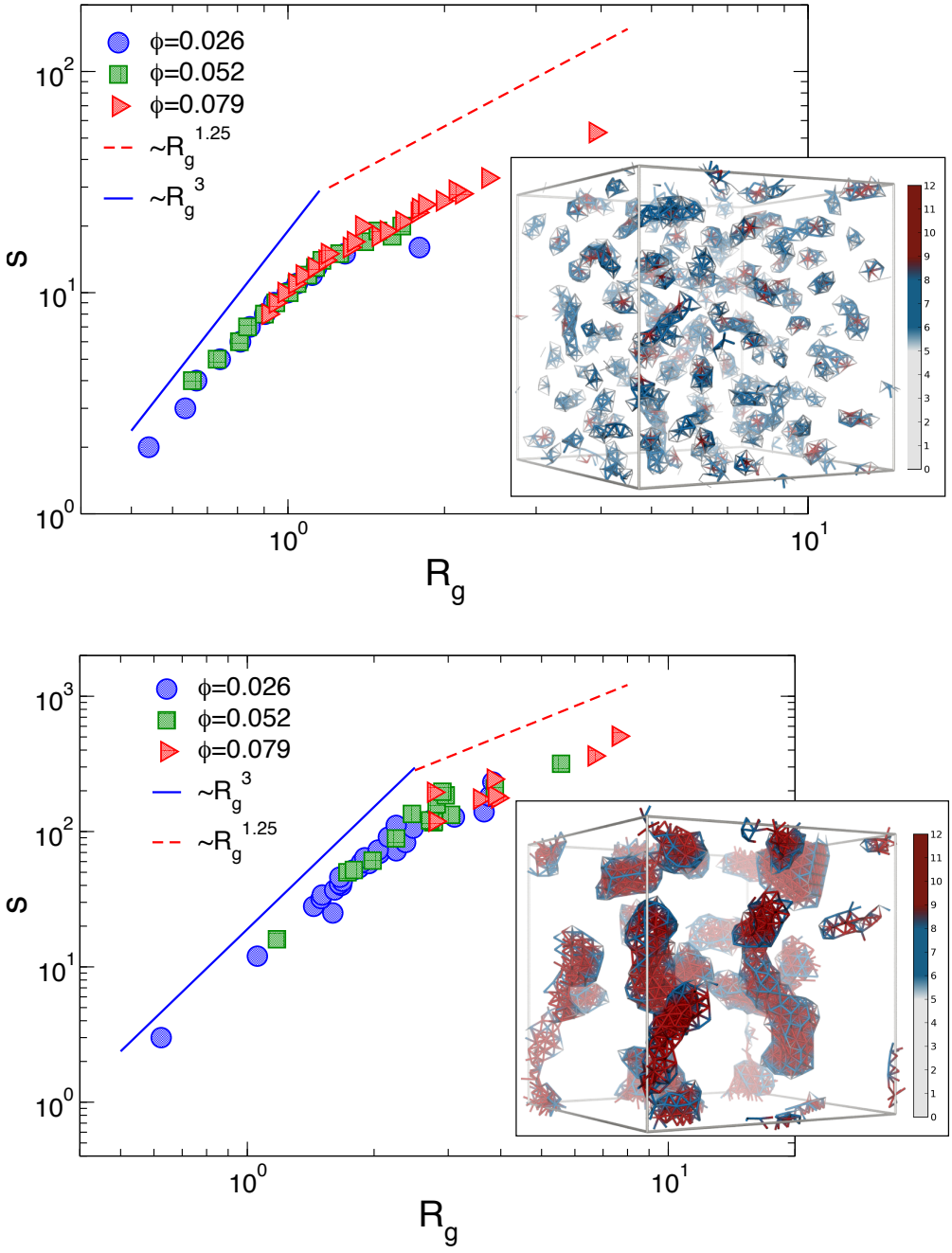

Fig. 4.4 Cluster size s vs radius of gyration R_g at $T = 0.15$ of HS (top) and LS (bottom). The solid and dashed lines show the expected behaviours for spherical and linear growth, as discussed in the text. The snapshot displays the bond representation of the cluster states obtained at $\phi = 0.079$ and $T = 0.15$ for HS (top) and LS (bottom) in the linear growth regime. The bonds in grey correspond to coordination number below six, in blue from six to nine and in red to higher than nine.

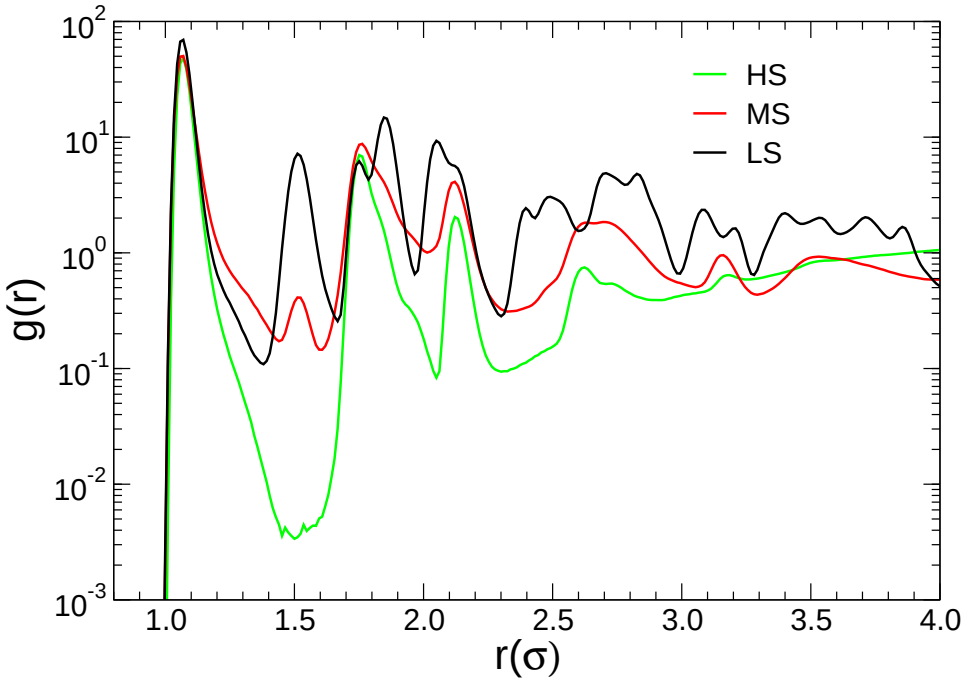

Fig. 4.5 Pair distribution functions $g(r)$ of HS, MS, LS at $\phi = 0.079$ and $T = 0.15$.

shows instead a strong signal of crystalline order (in particular of both hcp and fcc) already at very low volume fraction, $\phi = 0.052$ (see Fig. 4.6 (bottom)). The same analysis performed for MS confirms the similarity with HS at low ϕ. Overall, at low ϕ, by decreasing the repulsive shoulder from HS to MS to LS, thin fibrillar clusters become larger, thicker and crystalline.

4.5 Thermodynamic characterization

We would like to clarify now the stable or metastable nature of aggregates discussed in the previous section. For this purpose we have computed the isochoric specific heat C_V/k_B, the excess chemical potential μ_{exc}/ϵ at the same volume fractions and the free energy of fcc and hcp crystals for HS and LS.

In Fig. 4.7, the specific heat computed from the energy fluctuations of MC simulations, is plotteed as a function of the temperature. C_V/k_B has a peak at $k_BT/\epsilon \sim 0.25$ for HS and $k_BT/\epsilon \sim 0.33$ for LS. By increasing the repulsion, from LS to HS, the peak position moves to a lower temperature. LS has a peak, similar to typical gas liquid thermodynamic transition. HS instead has a very small peak that is reminiscent of a micellization process as also found and discussed in Refs [84, 127].

Further insight can be gained form the free energies and the excess chemical

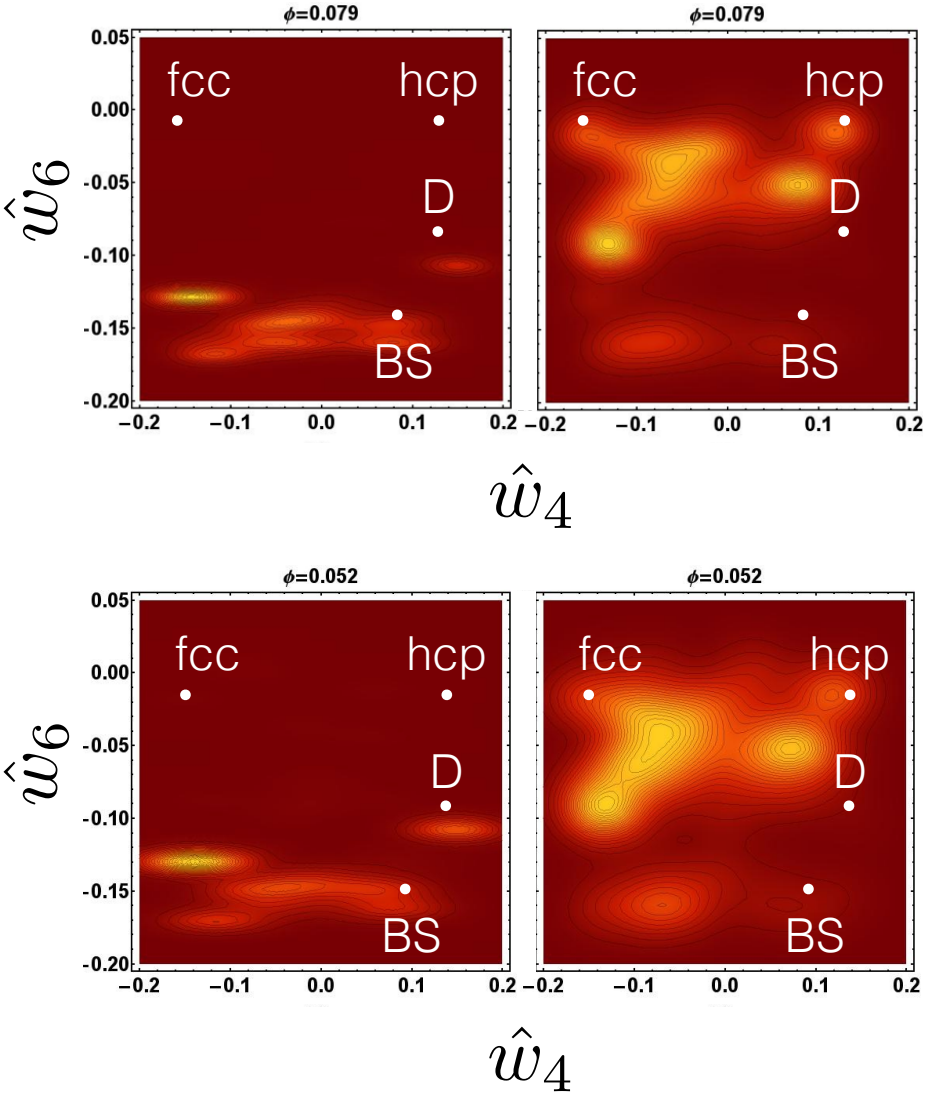

Fig. 4.6 Contour plots of ($\hat{w}_6$, $\hat{w}_4$) BOO parameters at $\phi = 0.079$ (top) and $\phi = 0.052$ (bottom) and $T = 0.15$ for HS (left) and LS (right). The dots represent the different local packings: fcc, hcp, Bernal spirals (BS) and dimers (D).

potential at different volume fractions and densities. Using the Einstein crystal method (see Section 4.3.2), we have estimated the values for the free energy A/Nk_BT and the chemical potential μ_{exc}/ϵ of fcc and hcp crystals at equilibrium densities ρ_{equil} at $k_BT/\epsilon = 0.15$ and $k_BT/\epsilon = 0.3$, which are shown in Table 4.1. Due to the lower repulsion, LS crystals have much lower free energy than the HS ones [1]. In Fig. 4.8, we plot the excess chemical potential computed for HS using the Widom insertion method. The opaque temperature region corresponds to

[1]The free energy of the fcc and hcp crystal are the same within the error bar of our calculation, so we cannot distinguish which crystal is more stable.

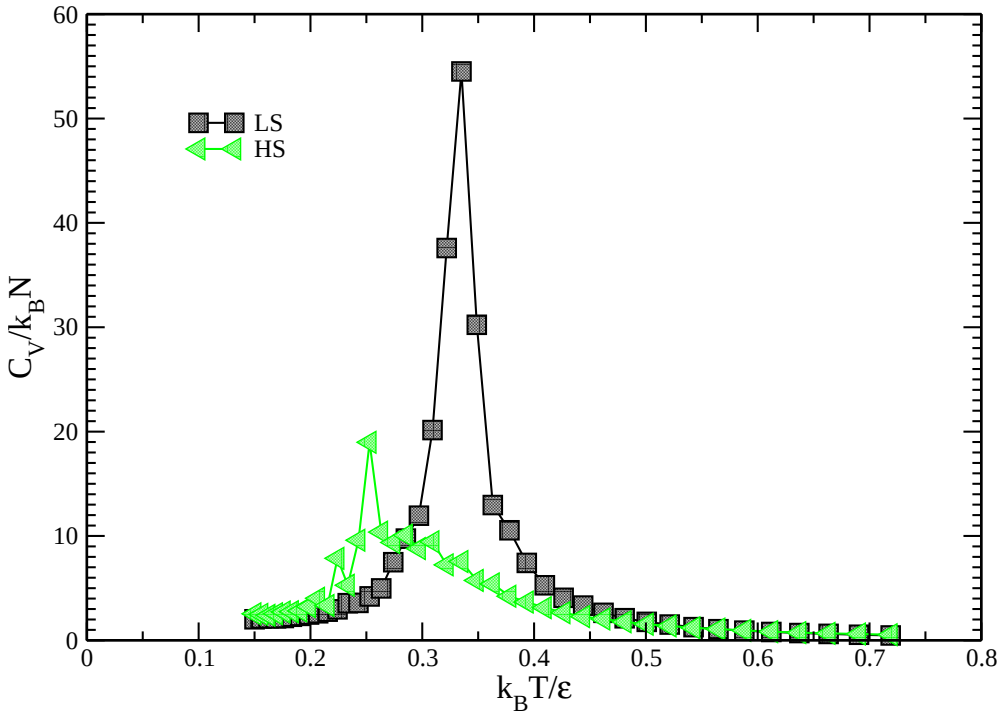

Fig. 4.7 Specific heat C_V/k_B as function of the temperature T for HS and LS for $\phi = 0.052$. The error bars are of the order of the symbol.

clusters with a characteristic size s, resembling density fluctuations, as they form and dissolve during the MD simulations. The pressure in these simulations is ~ 0 and we can compare these results to the values shown in Table 4.1. We notice that for HS the corresponding fcc and hcp crystals (star) have higher μ_{exc}/ϵ than the clusters. For HS, this confirms the scenario of microphase separation with a low ϕ equilibrium cluster phase.

Table 4.1 Values of free energy A/Nk_BT and chemical potential μ_{exc}/ϵ for both fcc and hcp crystals of LS and HS potentials at ρ_{equil}. The measured values of A/Nk_BT and μ_{exc}/ϵ are the same within the statistical error for fcc and hcp crystals.

Crystal	k_BT/ϵ	ρ_{equil}	A/Nk_BT	μ_{exc}/ϵ
fcc/hcp HS	0.15	1.13	-1.34	-0.21
fcc/hcp HS	0.30	1.11	3.55	3.18
fcc/hcp LS	0.15	1.15	-21.82	-3.27
fcc/hcp LS	0.30	1.13	-6.81	-2.04

In Fig. 4.9 we plot the μ_{exc}/ϵ obtained by Widom insertion for LS in the gas phase. By comparing the data to the one in Fig. 4.8 we notice that in the gas phase, the excess chemical potential for both HS and LS decreases as T increases, indicating a corresponding increase of the average volume available to insert new

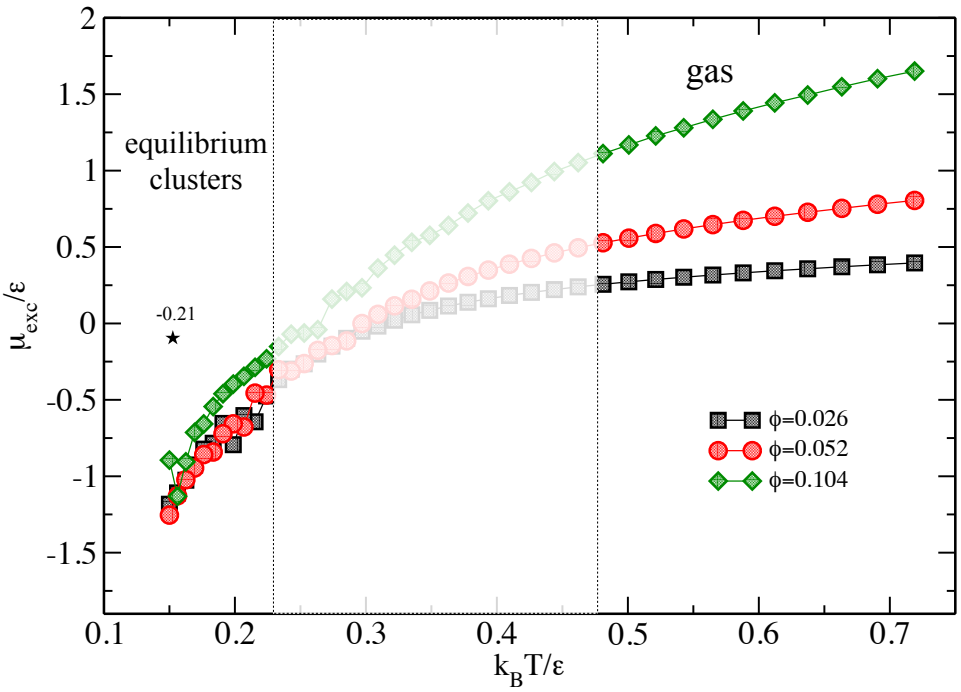

Fig. 4.8 Chemical potential μ_{exc}/ϵ as function of the temperature T for the HS, computed using the Widom insertion method. Clusters of a typical size form and dissolve in the opaque region. At lower T, equilibrium clusters are detected. The star indicate the μ_{exc}/ϵ for both fcc and hcp crystals from Table 4.1.

particles in the system because of the cluster formation. For HS, the gas phase is purely repulsive as $\mu_{exc}/\epsilon > 0$, whereas for LS and $k_BT/\epsilon \lesssim 0.55$ the gas phase becomes attractive. Moreover, for LS the trend of the different volume fractions reverses, that is in the attractive regime the higher the ϕ the lower the μ_{exc}/ϵ, hence the higher the volume fraction the easier to insert particles. HS only becomes attractive at the end of the opaque region of Fig. 4.8 and around this temperature the clusters begin to persist. If we use the position of the peak in the specific heat shown in Fig. 4.7 for LS to locate the gas liquid transition, we can recognise that in the MD simulations the liquid states of LS are characterized by crystalline clusters that do not coalescence or grow within the simulation time window. Nevertheless, we do observe breaking and merging of the crystalline clusters, suggesting that a high energy barrier associated to aligning the crystalline surfaces prevents them from forming one bulk crystal within our simulation time window. In the Widom insertion simulations performed at sufficiently low T for small systems, instead, the full system crystallizes and the corresponding value of μ_{exc}/ϵ is consistent with the value in Table 4.1 for LS at $T = 0.15$.

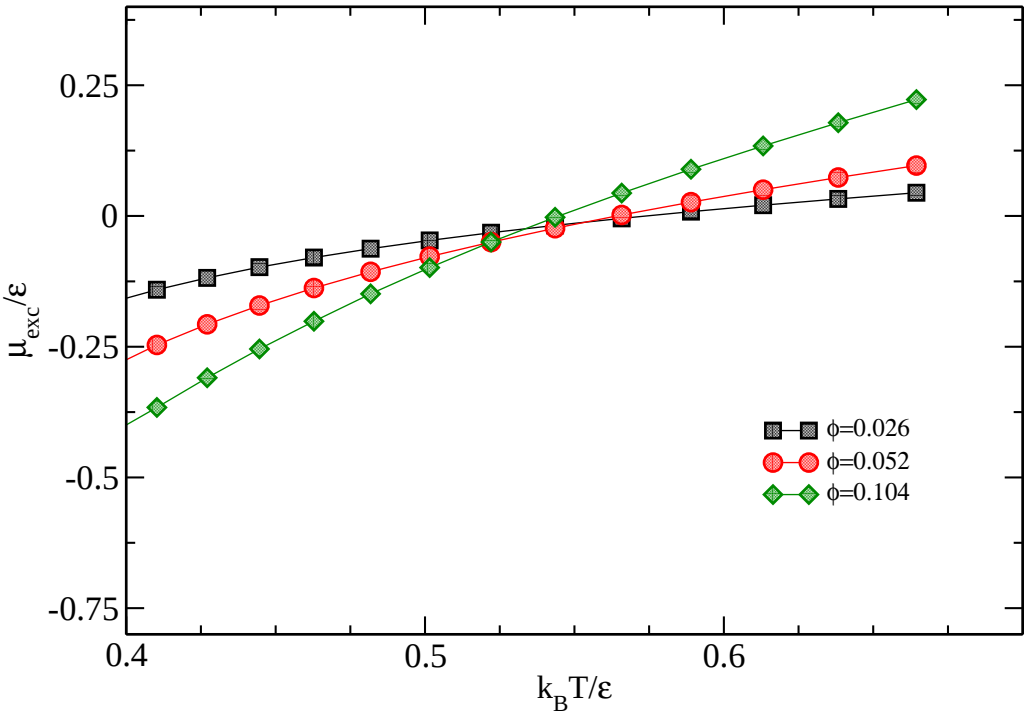

Fig. 4.9 Chemical potential μ_{exc}/ϵ as function of the temperature T for LS computed using the Widom insertion method at high T.

4.6 Morphology and local packing of arrested states

In this section we discuss the morphology and local packing of the aggregates obtained with HS, MS and LS at higher volume fraction. In all these cases the aggregates linear size becomes comparable to the simulation box and their features may strongly depend on the cooling protocol and on the finite system size. Nevertheless, here we focus on changes in the gel morphology that are consequence of changing the interaction potential. Hence, we expect that the emerging qualitative picture to hold, to a certain extent, also for experimental systems and conditions. Examples of the networks formed upon kinetic arrest in the MD simulations are shown in Fig. 4.10, at $\phi = 0.157$ and $k_BT/\epsilon = 0.15$ (left) for HS and at $\phi = 0.209$ and same T (right) for LS. In the snapshots only the bonds among the particle are depicted and the color code corresponds to the amount of nearest neighbors. Again, as in Section 4.4.2, we use the cluster size distribution n_s, the pair distribution function $g(r)$ and the bond orientational parameters BOO ($\hat{w}_6$, $\hat{w}_4$) to characterize the structure of the arrested states.

In Fig. 4.11 we plot n_s upon increasing ϕ for HS. Here, we plot n_s at $k_BT/\epsilon = 0.25$ because the features of the clusters that correspond to the equilibrium conditions can be seen clearly at higher temperatures, where the effect of

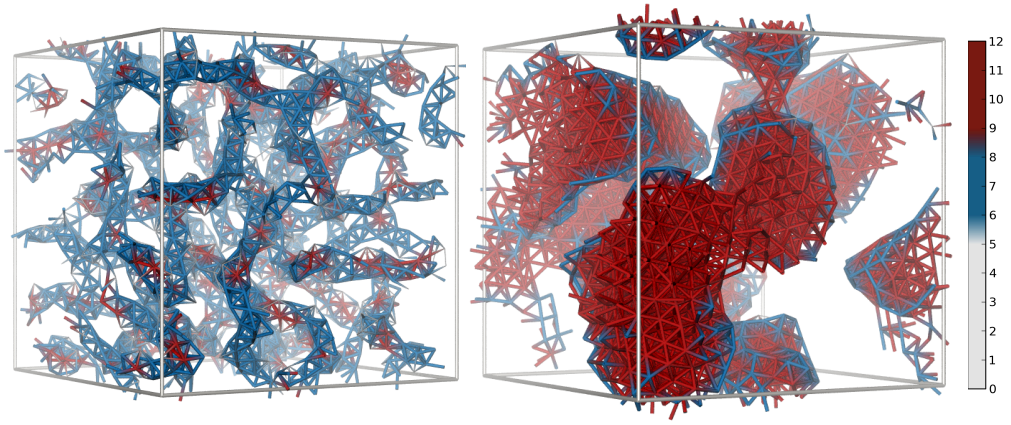

Fig. 4.10 Snapshots of the bond representation of the arrested networks. The left one is for HS obtained at $\phi = 0.157$ and right to LS at $\phi = 0.209$ both at $k_BT/\epsilon = 0.15$. The bonds in grey correspond to coordination number below six, in blue from six to nine and in red to higher than nine.

kinetics is less important. The cluster size distributions have a characteristic peak which increases slightly upon increasing ϕ, from $s = 9$ for $\phi = 0.026$ to $s = 15$ for $\phi = 0.157$. Upon further increasing ϕ the distribution develops a power-law tail, consistent with an exponent $n_s \propto s^{2.2}$ that indicates random percolation of the clusters. The data indicate that the percolation threshold can be located in the range $0.131 \lesssim \phi \lesssim 0.157$. These findings confirm the formation of a space spanning network starting from the clusters. For the MS potential we obtain a similar cluster size distribution, however in this case the random percolation occurs at a lower volume fraction $\phi \approx 0.079$. Upon decreasing the repulsion strength (in the case of LS), instead, no percolation is observed even at this relatively higher temperature.

The percolation thresholds just reported depend on the temperature and also on the cooling protocol used for the systems at different T and ϕ. They have been evaluated for a fixed system size, hence they are not intended to be exact by any means, since this would require a finite-size scaling analysis. As already mentioned above, the arrested states discussed here depend of course on the specific kinetic path selected by the MD simulations, i.e., they are specific of the NVE or NVT MD simulations performed and of the cooling protocol chosen. We have verified that, for sufficiently slow cooling, the gel morphology and properties discussed here are not significantly affected by the cooling rate. They could change if MD simulations were performed at constant pressure (rather than at constant volume), although we have monitored the pressure in our simulations and we could not detect any steep or abrupt change in pressure upon gel formation. On this basis, we do not expect too large differences. With respect to experimental conditions, one could expect colloidal gelation to result into the development of tensile internal stresses [131, 132], due to the net attractive interactions that drive the gelation

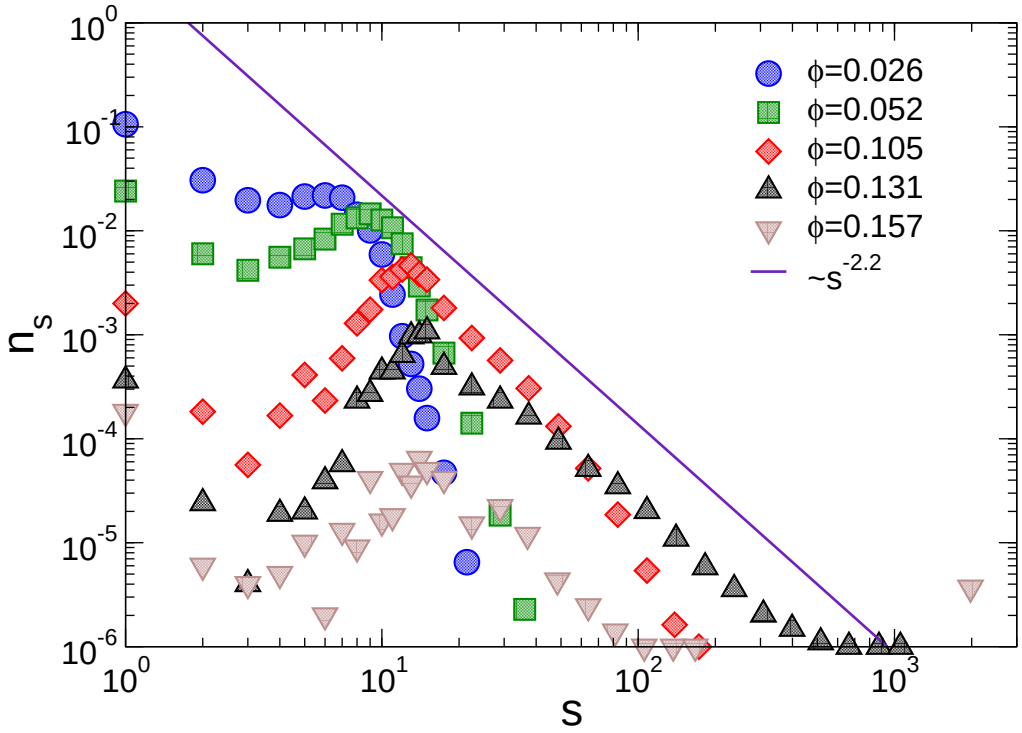

Fig. 4.11 Cluster size distribution n_s at $T = 0.25$ for HS. The power law of the line corresponds to the random percolation.

and to the formation of a poorly connected structure. Therefore, the periodic boundary conditions and the imposed fixed volume could be compatible with the experimental conditions under which the gels are forming.

We have already mentioned in Section 4.4.2 that by reducing the strength of the repulsion with respect to the attraction in the interaction potential the particle packing in the clusters qualitatively changes. As in Section 4.4.2, we plot the $g(r)$ in Fig. 4.12 for HS, MS and LS at $\phi = 0.314$ and $k_BT/\epsilon = 0.15$. In contrast to low ϕ, at high ϕ, the data for MS display peaks very similar to the ones for LS, indicating crystalline local packing. LS local crystalline order does not change much upon increasing ϕ. At $\phi = 0.314$ HS has not developed a second peak in the g(r) yet, however for $\phi \geq 0.4$ it does and in addition all three potentials have similar peaks, corresponding to the formation of similar crystals. Fig. 4.13 displays the contour plots of ($\hat{w}_6$, $\hat{w}_4$) computed at two different volume fractions $\phi = 0.131$ and $\phi = 0.419$ for HS (top) and LS (bottom) and at $k_BT/\epsilon = 0.15$. For HS, by increasing ϕ, the signal of Bernal spiral of the clusters becomes very clear at $\phi = 0.131$ (just before the percolation threshold at this temperature). This is consistent with the results reported in other studies [84, 130]. At higher volume fraction, there is still a strong signal corresponding to the Bernal spiral local order and only for $\phi > 0.4$, $\hat{w}_6$ and $\hat{w}_4$ tend to change towards the values typical of a hcp crystal. For LS, upon increasing ϕ, the crystalline order is clearly predominant and the signal

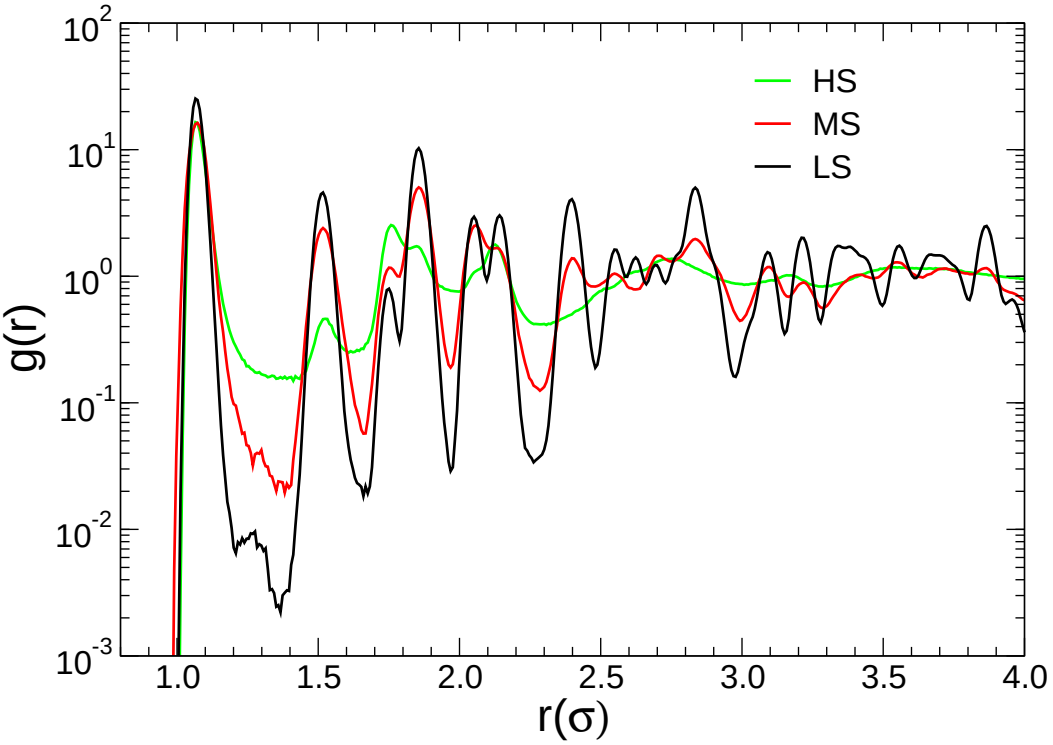

Fig. 4.12 Pair distribution functions $g(r)$ of HS, MS, LS at $\phi = 0.314$ and $k_BT/\epsilon = 0.15$.

corresponding to the hcp crystal is more pronounced than the fcc one. The same analysis performed for MS confirms the similarity with HS at low ϕ (up to the percolation of the elongated aggregates) and a stronger similarity to LS instead at higher ϕ, with a local order that closely resembles the high density crystalline phase.

In the diagrams of Fig. 4.14 and Fig. 4.15, we summarize the results of the previous sections for HS and LS, respectively. The state points obtained with MC or MD simulations are shown using different symbols and correspond to either equilibrium phases or arrested states.

For HS, the circles in Fig. 4.14 stand for the gas, the squares for the clusters, the triangles for the gel states and the diamond for the crystal. The opaque region corresponds to the opaque region of Fig. 4.8 where clusters of a typical size form and dissolve. The dashed line denotes the peaks of the specific heat (see Fig. 4.7) at different ϕ and indicates the region of equilibrium clusters. At very low volume fraction the system forms persistent disconnected clusters of characteristic cluster size and at higher volume fraction, the clusters become elongated, grow and aggregate. This type of aggregation is strongly reminiscent of micellization in solutions of surfactants or diblock copolymers [129, 133]. The formation of these colloidal micelles seem to prevent the gas liquid phase separation at low ϕ, but can

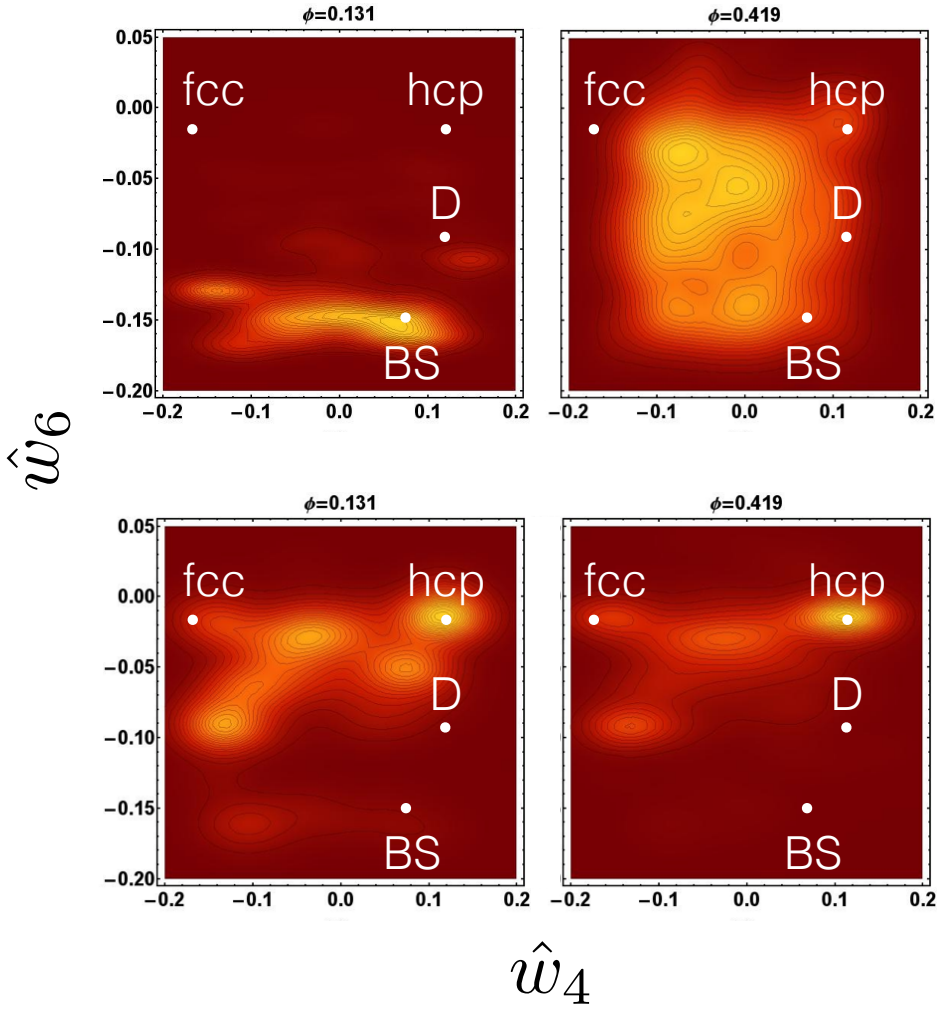

Fig. 4.13 Contour plots of ($\hat{w}_6$, $\hat{w}_4$) BOO parameters at $\phi = 0.131$ and $\phi = 0.419$ at $k_BT/\epsilon = 0.15$. Upper panels for HS and lower for LS. The dots represent the different local packings: fcc, hcp, Bernal spirals (BS) and dimers (D).

be detected in the specific heat that shows a small peak (see Fig. 4.7 and dashed line in Fig. 4.14). The elongated clusters, that start to form around $\phi \sim 0.1$, are characterized by a local packing that is very similar to the one of Bernal spirals. This type of local packing has already been observed in simulations [84, 110] and in experiments [78] and can be also explained in terms of the competing interactions. The elongated clusters (or micelles) eventually branch and form the gel network in the MD simulations with HS (and MS). The solid line in Fig. 4.14 indicates the percolation of such networks. The diagram for MS is qualitatively similar to HS.

For LS, the circles in Fig. 4.15 stand for the gas, the squares for the disconnected crystalline clusters observed in the MD simulations, the triangles for spanning gel networks and the diamonds for the crystal. The solid line indicates the gas liquid

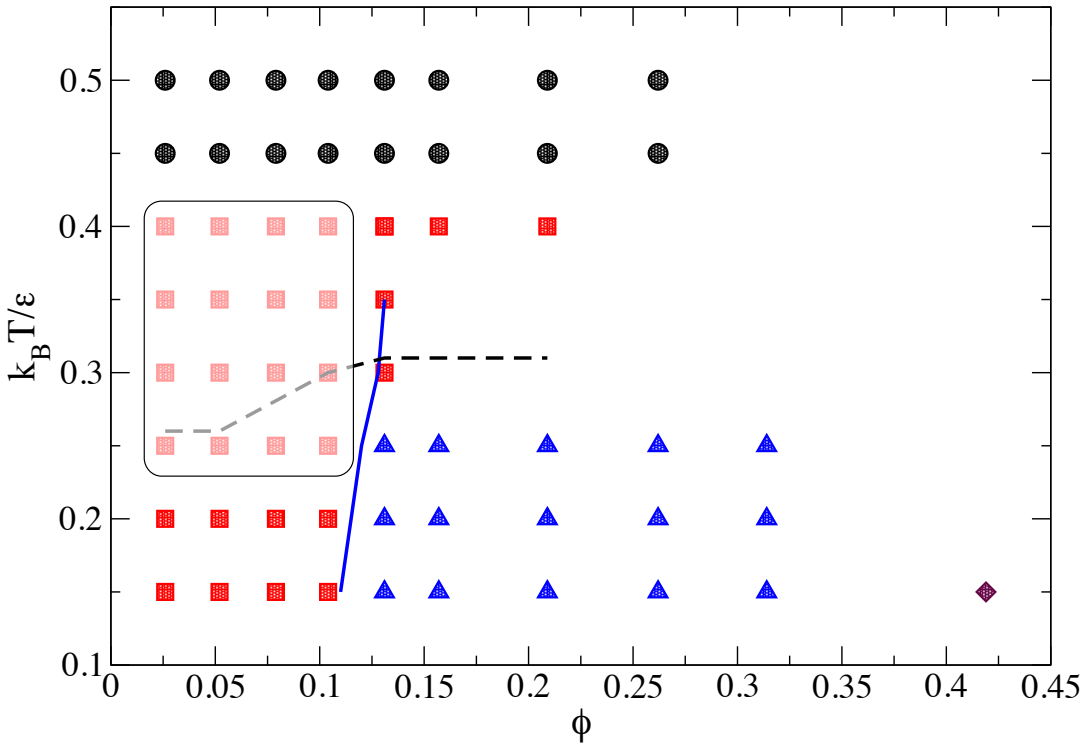

Fig. 4.14 Diagram of equilibrium and arrested states obtained in the simulations with HS potential. The squares represent clusters and the triangles the micellar gel. At low T and high volume fraction $\phi \leq 0.340$ the crystal is the stable phase (diamond). The dashed line indicates the region of equilibrium micellar clusters and the opaque rectangular corresponds to short-living clusters. The solid line is the percolation line deduced from the cluster size distributions, e.g. Fig. 4.11.

transition line as detected from the peak in the dependence, on temperature, of the specific heat at different ϕ. At $k_BT/\epsilon \gtrsim 0.2$, we observe in the simulations that the cluster and gel states coexist with monomers. The gel states correspond to the clusters merging and impinging to form a network-like structure with thick crystalline branches (see right snapshot of Fig. 4.10). Independently from the presence of gels, we have found that the clusters for LS are always metastable with respect to the bulk crystalline states.

4.7 Conclusions

Analysing the equilibrium and kinetically arrested states at fixed density in presence of repulsive interactions of fixed screening length and of short-range attraction has been useful to elucidate a number of issues. We have investigated

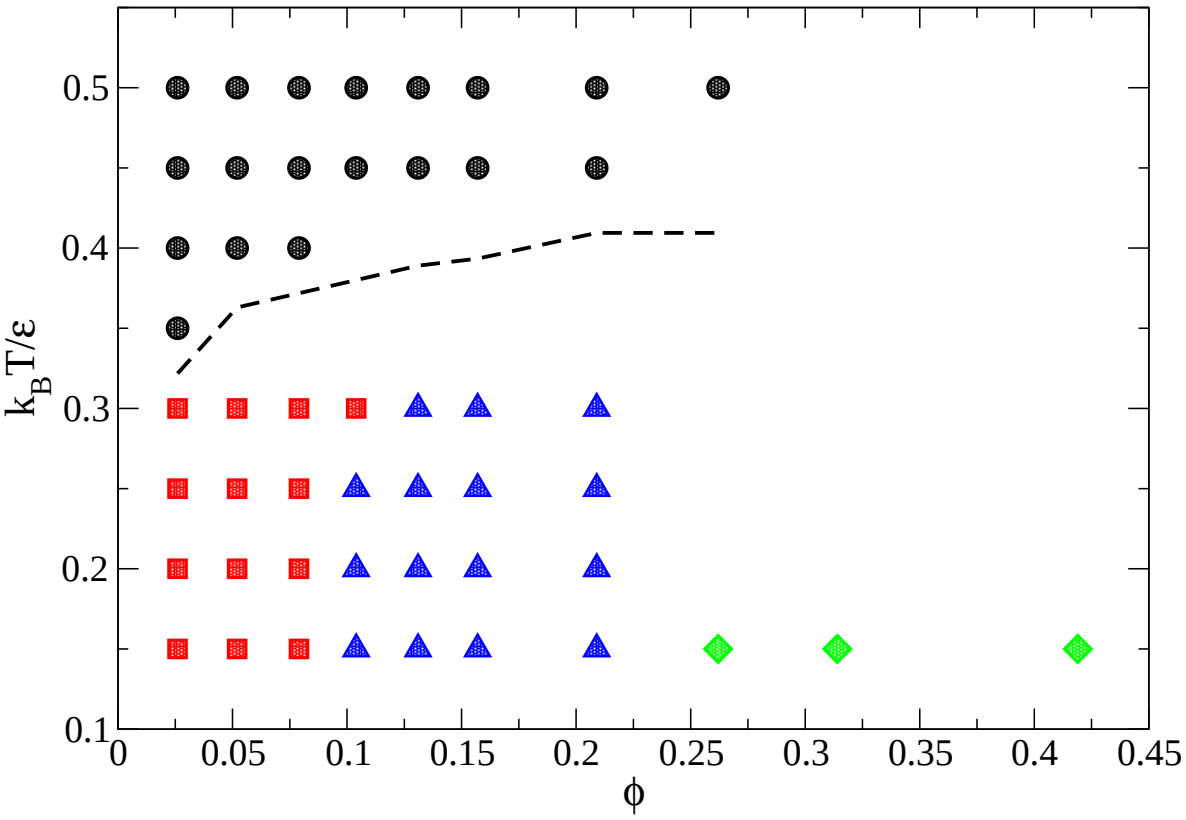

Fig. 4.15 Diagram of equilibrium and arrested states obtained in the simulations with LS potential. The circles correspond to the gas phase, the triangles to crystalline gel states, the squares to isolated crystalline clusters and the diamonds to the crystal phase. The solid line represents the gas liquid transition.

how the equilibrium phases *and* the metastable states change in the presence of a repulsive interaction of fixed screening length and a short range attraction, upon changing their relative strength. We have seen how these changes affect the local packing, the mesoscale organization and the gelation route.

When the repulsion is small, as in the case of LS potential, the crystal becomes stable at lower volume fractions and large disconnected crystalline clusters, that are metastable, tend to form. These clusters do not easily coalesce until relatively high volume fractions. The pronounced metastability of such aggregates could be due to a significant free energy barrier for coalescence: only surfaces that come together with the correct relative orientation may coalesce and any mismatch due to the irregular shape might enhance this effect. The percolation of the aggregates and hence the formation of gels is limited to relatively high volume fractions. We have found that the local structure in the metastable states is the same as the underlying stable crystalline structure, which is not necessarily generally true. A somewhat different scenario has been observerd for crystal nucleation in a binary suspension

of oppositely charged colloids [134] where they observed nucleation of metastable clusters with different crystalline symmetry from the stable state. However, we must stress that in our case the two crystalline symmetries (fcc and hcp) could hardly be differentiated due to the fact that the free energy per particle is very similar in both states.

Upon increasing the repulsion strength in the effective interactions, the phase diagram changes towards a microphase separation characterized by an equilibrium cluster phase. At low volume fractions, the clusters are small and compact but upon increasing ϕ they grow into elongated shapes. Further increase of ϕ leads to the formation of space-spanning network of such elongated clusters, i.e. a gel. This type of gel has a local structure which is again very close to the one of the equilibrium (it is the same as in the equilibrium elongated clusters – very similar to Bernal spirals) and is stabilized by the long range repulsion. As ϕ increases, the local packing eventually shifts towards the fcc/hcp crystal.

The cartoon shown in Fig. 4.16 summarizes our results on the basis of the contour plots of ($\hat{w}_6$, $\hat{w}_4$) discussed in Section 4.4.2 and 4.6. The direction of the arrows correspond to the increase of the volume fraction. In the HS case, the local packing changes from BS towards fcc upon increasing ϕ, while for LS the BS packing is not observed and compact crystalline packing is predominant at all volume fractions ϕ.

In conclusion, the strength of the repulsion with respect to attraction of the interaction potentials of interest here changes both the equilibrium phases and the metastable states, influencing the local packing, the mesoscale organization and the gelation route. We have seen in the previous chapter that the out-of-equilibrium conditions under which the C–S–H gels form interplay with the equilibrium phases and metastable states that we have discussed in this chapter. We can now clearly recognize that a few features of the equilibrium and arrested states discussed in this chapter survive when the aggregation and gelation occur during precipitation and have therefore a significant role also in determining the properties of C–S–H gels. These findings have further implications on the onset of gelation and the rigidity of the formed gels as we will see in the next chapter.

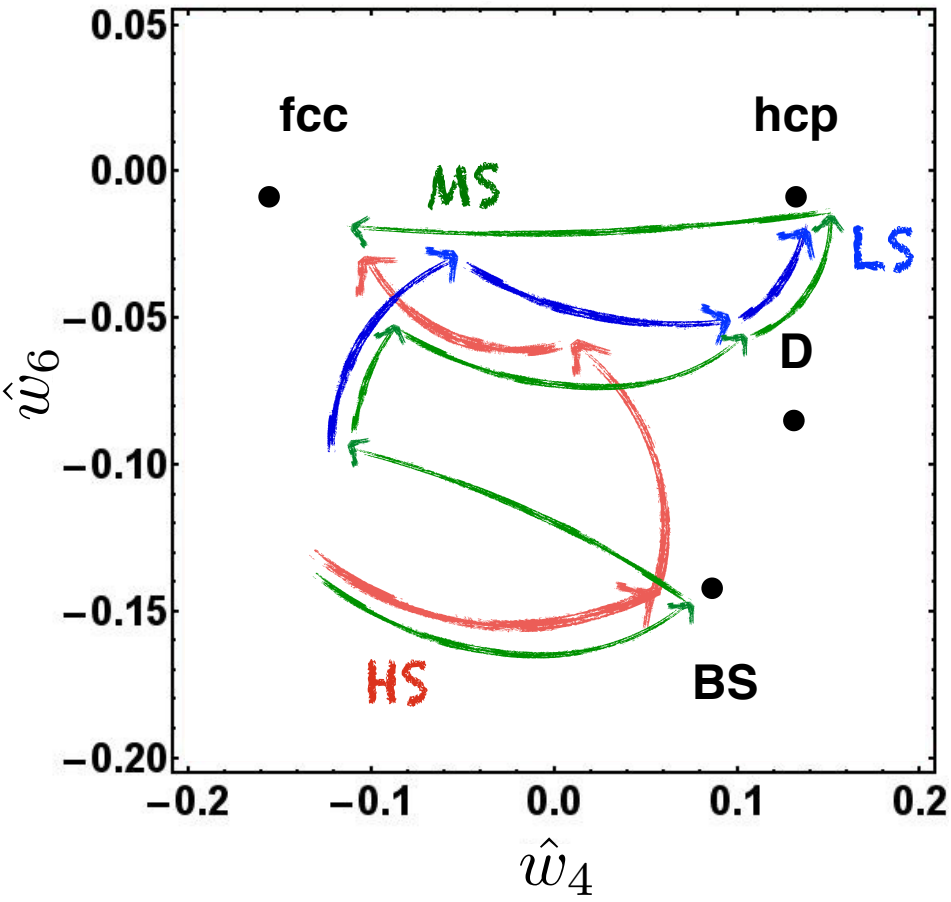

Fig. 4.16 Schematic representation of the evolution of the local packing (BOO) upon increasing volume fraction for LS, MS and HS. The direction of the arrows indicates the increase of the volume fraction. The blue color corresponds to LS, the green to MS and the red to HS. Upon increasing the repulsion strength with respect to attraction (from LS, to MS, and to HS) at low volume fraction the local packing of the particles changes from crystalline (fcc) to BS and at high volume fraction changes from hcp to fcc.

Chapter 5

Structure and mechanics of C-S-H

In the previous chapters we have presented a new approach for investigating the formation of C–S–H gels and the development of their morphology during cement hydration. We have shown how this approach, based on statistical mechanics and on soft and condensed matter physics, does capture a few features of cement hydration and allowed us to gain new insight into the fundamental physical mechanisms that may govern it. By analysing the structure of the model C–S–H gels, we suggested also an interpretation for the different hydration regimes based on the underlying equilibrium phases. We would like now to attempt a qualitative and quantitative comparison of the structure and mechanical properties of the gels obtained in the simulations with different experimental observations and, on this basis, try to rationalize the experimental findings. In particular, here we discuss the pore size distribution and the scattering intensity and the evolution of the shear modulus and the nanoindentation modulus of the gels obtained in the simulations.

5.1 Introduction

The model described in Chapter 3 is a first attempt to a coarse-grain model that can use input from atomistic simulations or experiments of smaller length scale and can provide the missing step between the atomistic structure and macroscale behavior of the material. Such step requires fundamental understanding of the interplay between effective interactions between the basic C–S–H units, chemical conditions (supersaturation of the solution, concentration gradient) and the resulting mesoscale morphology.

It is clearly non trivial to connect the outcomes of our simulations to the experimental observations, as already discussed, for example, in Chapter 3. Most experiments in fact give macroscopic information that involves all type of phases of cement, whereas the model we presented refers only to C–S–H. In addition, most of the experiments are also performed on the hardened cement paste rather than at

the early stages of hydration. In spite of these considerations, it still makes sense to attempt the comparison, because it has been proved at several levels that the features developed during the early stages of hydration largely determine the material properties of the hardened paste. Although there is still very limited nanoscale experimental information available on the early stages of hydration, most of the experimental efforts are now focusing in this direction, hence we are confident that in the next few years our connection with experiments can be made more direct and quantitative. In the following, we will make the reader aware of the limitations of the comparison with the experiments and in some cases we will complement it with new results obtained in recent studies.

5.2 Porosity

NMR experiments have the advantage of measuring the porosity of cement without destroying the structure of C–S–H gel, hence they provide the typical sizes of pores in hydrated cement as a function of the degree of hydration and water to cement ratio of the cement paste. They typically suggest two distinct populations of pores, the capillary pores and the gel pores. As the hydration proceeds the capillary pore size and the corresponding pore volume decrease. The experiments show that during the first days of hydration the amount and size of large capillary pores decrease rapidly with a typical size of $25 - 35nm$, whereas the typical gel pores size is $3 - 5nm$ and relatively constant [22, 135]. In this section, we evaluate the pore size distribution of the configurations that were generated with the model described in Chapter 3 and compare them with the experimental results.

The pore size distribution of the gels obtained in the simulations can be determined using probe particles and a geometric analysis. At each point $\mathbf{x}$ of the sample not belonging to the particle matrix, the pore size is defined as the largest sphere that contains the given point without overlapping with the boundary of the particle matrix. The diameter s of such a sphere is then the pore size at point $\mathbf{x}$. The pore size distribution is found by constructing a finite grid and evaluating the largest sphere diameter s at each grid point. In this way and using the probability $h(s)$ that a point in the void space is in a pore with size greater than or equal to s, a cumulative histogram can be computed. Finally, the pore size distribution is $p(s) = -dh(s)/ds$.

A common approach to find the largest diameter s at a point $\mathbf{x}$ is to create a database of spheres centered at each grid point, with the largest possible diameter that do not overlap with the boundary particles, search through the database in the neighboring grid points of $\mathbf{x}$ and select the largest sphere that contains also $\mathbf{x}$. Here this problem has been treated as a constrained nonlinear optimization problem and it is solved by using SOLVOPT, a nonlinear algorithm which can handle discontinuous objective functions [136, 137]. The

main advantages of this choice is that a grid is not needed, because the algorithm chooses random points through the continuum. Moreover, it converges faster due to efficient searching schemes instead of probing each grid point. The accuracy of the pore size distribution depends on the number of the sampled points.

In Fig. 5.1 and 5.2, the pore size distributions of the S1 and S2 are shown respectively, for low (top) and high (bottom) kinetic rate. The pore size distributions obtained from the model C–S–H gels show overall the same trend as the experimental data presented in Ref. [135] and are in agreement with Ref. [22]: the capillary (large) pores size decreases as the hydration proceeds (i.e. upon increasing ϕ) and the gel pores sizes are relatively constant. Upon densification of S1 at a low kinetic rate ($R = 0.2$), initially only capillary pores are observed of size $\sim 23nm$ and, as the volume fraction increases, these larger pores reduce their typical size to $\sim 15nm$. For $\phi > 0.11$ the gel pores of size $\sim 3nm$ arise and remain relatively constant upon densification. This suggests that the typical size of the gel pores must be related to the onset of the optimal local packing that develops as the aggregation proceeds, as discussed in Chapter 3 and 4. This could explain why the characteristic gel pore size does not significantly change as the hydration proceeds further. For high kinetic rate $R = 4$, the pore sizes have the same trend indicating that the pore size distribution of S1 is mainly dictated by the interparticle potential as we would expect on the basis of the results discussed in Chapter 3. For high volume fractions $\phi > 0.419$, the amount and size of capillary pores decreases and a slightly larger typical size for the gel pores ($\sim 5nm$) appears.

Upon densification of S2 at low kinetic rate ($R = 0.2$), the capillary pores tend to be larger than the ones in S1, with a typical size of $\sim 32nm$, that as the volume fraction increases, decreases to $\sim 21nm$. The gel pores are of the same size as S1 $\sim 3nm$ and remain relatively constant upon densification. The gel pores typical size increases toward $5nm$ for volume fractions $\phi > 0.2$. For high kinetic rate $R = 4$, upon increasing volume fraction the capillary pores reduce their typical size more dramatically and the $5nm$ pores appear at much higher volume fraction than at low R. Hence the kinetic rate has a stronger effect on the organization of the gel. For high volume fraction $\phi > 0.4$, the larger pores completely disappear.

Overall, the type of effective interactions that we used for the C–S–H model and the resulting non-equilibrium structures can capture the bimodal pore size distribution typically suggested by experiments. In our model the two length scales are clearly induced by the fact that the gel forms in presence of short-range attractive and long-range repulsive interactions. In a real macroscopic sample of cement paste, most probably, regions of few hundreds nanometers with different volume fractions of C–S–H coexist [43]. Therefore we would expect to have a mixture of different local volume fractions contributing to the experimental results. Hence, what we present here would correspond to the evolution of one of those regions of

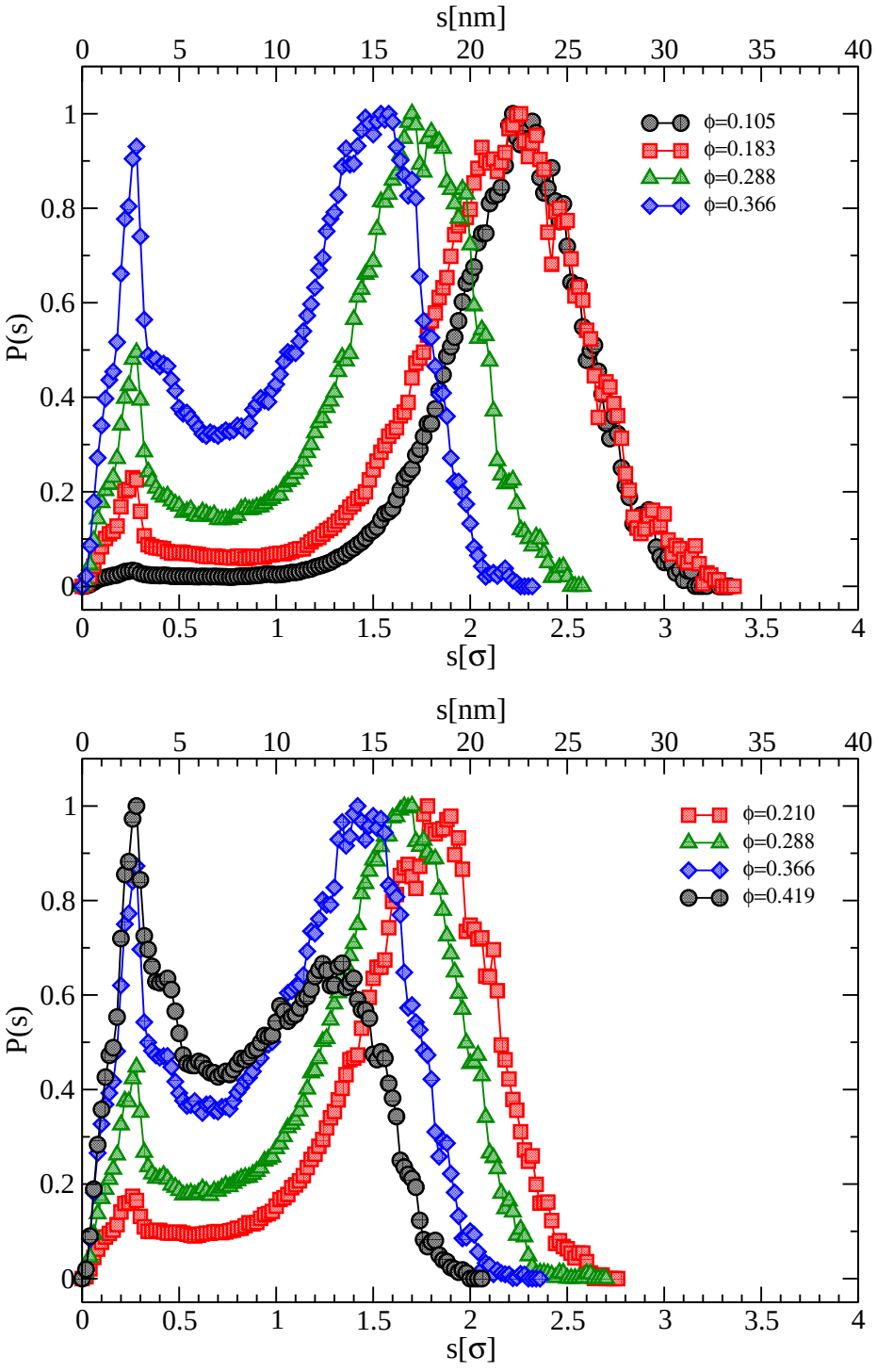

Fig. 5.1 Pore size distribution of S1 potential at low kinetic rate $R = 0.2$ (top) and high kinetic rate $R = 4$ (bottom) upon increasing volume fraction ϕ during the precipitation. The upper x-axis show the diameter of the pores in nm assuming that the particle diameter is $\sigma \sim 10nm$.

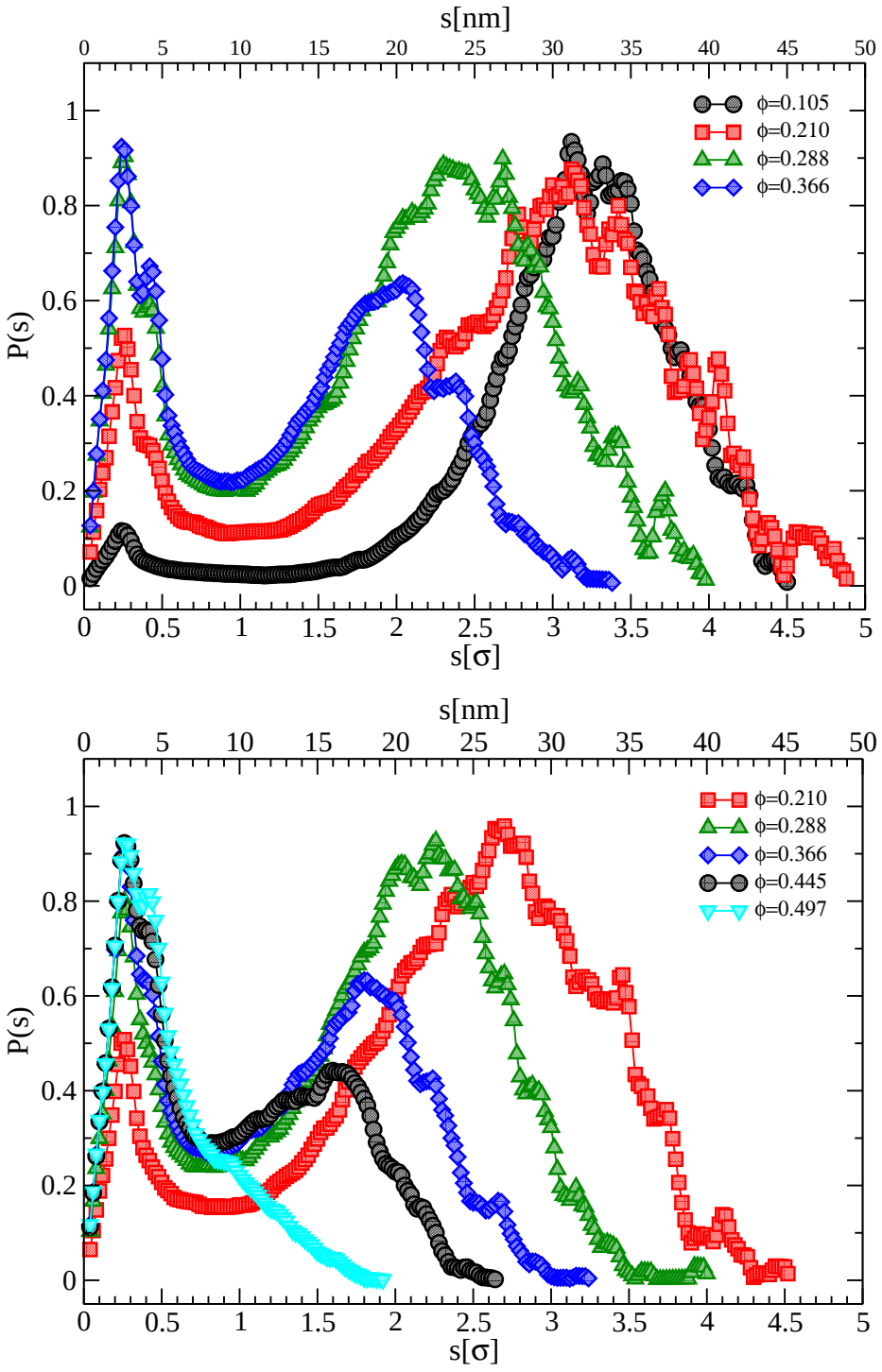

Fig. 5.2 Pore size distribution of S2 potential at low kinetic rate $R = 0.2$ (top) and high kinetic rate $R = 4$ (bottom) upon increasing volume fraction ϕ during the precipitation. The upper x-axis show the diameter of the pores in nm assuming that the particle diameter is $\sigma \sim 10nm$.

few hundreds nanometers.

5.3 Scattering intensity

To compare our model gels to the experimental outcomes of small angle neutron scattering (SANS) we computed the scattering intensity as

$$I(q) = \phi V^2 \Delta\rho^2 P(q) S(q) \tag{5.1}$$

where $q = 2\pi/r$ is the modulus of the scattering vector, ϕ is the volume fraction, V is the volume of a particle, $\Delta\rho$ is the scattering contrast, $P(q)$ is the form factor of the particles (monodisperse spheres of diameter σ) and $S(q)$ is the structure factor. $S(q)$ is the Fourier transform of $g(r)$ (Eq. 4.13) and can be computed directly from the particle configurations $\mathbf{r_i}$

$$S(q) = \left\langle \frac{1}{N} \sum_{i,j} e^{-i\mathbf{q}(\mathbf{r_i}-\mathbf{r_j})} \right\rangle \tag{5.2}$$

where N is the number of particles [138]. To comply with the periodic boundary conditions used in the simulation the $\mathbf{q}$ vectors are chosen as: $\mathbf{q} = \{n_x 2\pi/L_x, n_y 2\pi/L_y, n_z 2\pi/L_z\}$, where n_x, n_y, and n_z are integers > 0 and L_x, L_y, and L_z are the sizes of the rectangular simulation box. Assuming that the system is isotropic, we perform an average over all $\mathbf{q}$ vectors with same modulus q. The form factor P(q) accounts for the contribution to the scattering intensity of a single particle, which is basically determined by its size and shape. For spherical particles the form factor is:

$$P(q) = \left[3 \frac{\sin(qR) - qR\cos(qR)}{(qR)^3} \right]^2 . \tag{5.3}$$

As mentioned in Chapter 3, we consider that the particles have diameter $\sigma \simeq 10$nm and that the scattering contrast between the C–S–H particles and the water surrounding them is $3.1 \cdot 10^{-4}\,\mathrm{nm}^{-2}\mathrm{sr}^{-1}$ [42].

The scattering intensity detected at a given q is directly related to the spatial correlations in density fluctuations over length scales $\simeq 2\pi/q$. For large enough q the interface between two media is being probed. If the interface is smooth, the scattering intensity should decrease with increasing q as q^{-4} (Porod regime [139]). At intermediate q, $I(q)$ is dominated by the size and shape of the particles through $P(q)$. At low q the main contribution should come from the structure factor that quantifies long range correlations across the structure.

The SANS experimental curve in Fig. 5.3 [42] displays the typical features that characterize the microstructure of cement over length scales between the nanometer and the micrometer. A Porod regime, $\propto q^{-4}$, is observed at high q,

i.e. $q > 1nm^{-1}$. At intermediate scattering vectors, $0.4nm^{-1} < q < 1nm^{-1}$, $I(q)$ follows $\propto q^{-2}$ dependence. This regime is typically ascribed to fractal-like features of the C–S–H gel and can be reproduced by a number of different models, ranging from very dilute fractal aggregates to dense Apollonian packings or dense random packing of oblate disks [34, 140]. At lower q, i.e. $q < 0.4nm^{-1}$ the data show a different dependence $I(q) \propto q^{-3}$. This regime is still not understood. It is not observed in synthetic C–S–H samples and the related intensity increases if the cement sample is cured at high temperatures or if calcium chloride is added, hence it should be related to features of the C–S–H structures that can be modified under theses conditions. It has been suggested that it might be related to the presence of relatively rough interfaces between different phases or to correlations present in the spatial distribution of the gel pores [141].

In Fig. 5.3 the scattering intensities for S1(top) and S2 (bottom) are shown for a high and a low volume fraction attained during the precipitation with low kinetic rate $R = 0.2$, together with the experimental scattering intensity of Ref. [42]. At high q ($q > 0.8nm^{-1}$) both S1 and S2 display a Porod regime signalled by a dependence q^{-4}. However, the Porod regime of the experimental curve is smooth and does not display the oscillations as in the $I(q)$ obtained from the simulations. This due to the fact that in the simulations the interface between the gel matrix and the void (that should correspond to the interface between the C–S–H gel and water in the experiments) is composed of spherical particles, monodisperse in size, which is certainly not true in reality. The oscillations are immediately smoothed if one includes size polydispersity. At lower q, $0.1nm^{-1} < q < 0.7nm^{-1}$, the scattering intensity of S2 indicates significant long range correlations. This is due to the mesoscale large pores. At intermediate scale the S1 has also a peak around $q \sim 0.2nm^{-1}$ which corresponds to domains of size $30nm$ (i.e. 3σ) which is of the order of the modulation length due to the effective interactions. At even lower q, $I(q)$ is roughly constant for S2, whereas for S1 it decreases drastically indicating a significant loss of correlations. Real C–S–H probably consists of domains of different local densities that form during hydration due to the many possible sources of spatial (chemical and physical) heterogeneities, hence a direct comparison of simulations with experiments has clearly strong limitations. Nevertheless, our results indicate that the model C–S–H gels obtained in the simulations have a few features that can be related to the experiments: the different regimes in the q-dependence of the scattering intensity and the presence of long range spatial correlations at relatively high density indeed capture two important aspects that govern the scattering intensity of real C–S–H samples.

From a more quantitative point of view, the $I(q)$ obtained in simulations is one order of magnitude higher than the experimental one. This is probably because we use the same scattering contrast $\Delta\rho$ between water and C–S–H everywhere in the gel, while the contact area among particles is likely to give a smaller scattering

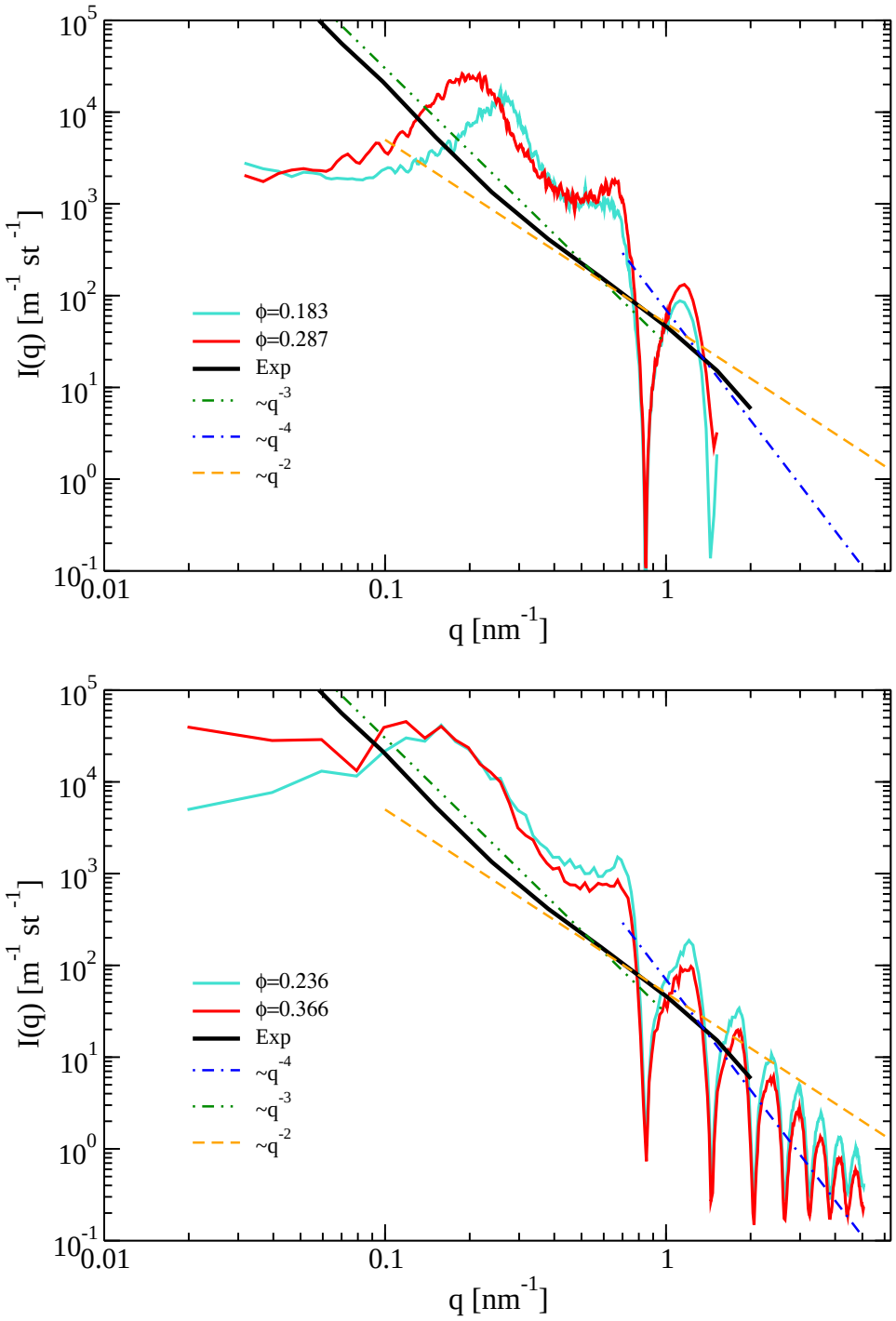

Fig. 5.3 Scattering intensity $I(q)$ for S1 (top) and (S2) (bottom). Two different volume fractions are shown from the C–S–H gel structures obtained from the simulations together with the experimental curve of Ref. [42]. The dashed and dotted dashed lines are the power low regimes of the experimental one.

intensity. Moreover, $I(q)$ measured in experiments is a signal averaged over a macroscopic sample, where larger pores (i.e. of typical size $\sim 100nm$) may be present and reduce significantly the scattering intensity. The scattering intensities obtained from the simulations arise from structures of fixed ϕ, while different C–S–H gel structures may contribute to the experimental results.

5.4 Mechanical tests

In this section, we analyse the mechanical properties of the C–S–H gels produced in the simulations and discuss them also in the context of the experimental results in hardened pastes. At present, there are no direct mechanical test performed during the early stages of the hydration and only a few rheological studies of the whole paste in these conditions are available [12, 142].

We have performed shear tests on the particle configurations of S1 and S2 at different stages of the hydration, obtained by stopping the rate dependent densification at different volume fractions. The samples were sheared in the xz plane with a constant shear rate $\dot{\gamma}$ up to a final strain $\gamma_{xz} = 30\%$, and the shear stress σ_{xz} was computed. The tests were performed using SLLOD equations of motion [143], coupled to Nosé-Hoover thermostat and Lees-Edwards boundary conditions. We extracted the elastic moduli G from the linear regime of the stress-strain curves, having explored a set of shear rates $\dot{\gamma}$ between 10^{-3} and 10^{-2} in reduced units. All the data shown in the following refer to a shear rate such that the variation of G with decreasing further $\dot{\gamma}$ is smaller than the error bar obtained by averaging over 5 independently generated samples. The simulations were performed with LAMMPS [104].

We also computed the indentation modulus of the particle configurations of S1 and S2, which is defined as:

$$M = 4G\frac{3K + G}{3K + 4G} \tag{5.4}$$

where G and K are the shear and bulk moduli for these conditions. G and K are computed from the components of the tensor of elasticity C_{ij} using the Voigt formulae [144]. The elasticity tensor C_{ij} is computed keeping fixed the simulation box after equilibration to zero stress, and using the stress fluctuation method [145], where the tensor of elasticity is decomposed into a configurational contribution related to the second derivatives of the interaction potentials, and a stress fluctuation component that includes the temperature. The particle configurations are relaxed to zero stress using the isotension isothermal NtT ensemble via MD and MC simulations [146, 147]. The NtT relaxation provides unstressed configurations where all the six components of the stress tensor are relaxed individually to approximately zero. The nanoindentation computations

were performed in collaboration with Dr. Enrico Masoero (Newcastle University)

5.4.1 Mechanics: Shear Modulus

We first discuss the results of the shear tests on the MD simulations without precipitation that we investigated in Chapter 4. In Fig. 5.4, the shear moduli are shown for S1 (top) and S2 (bottom) (black circles MD) for particle configurations without precipitation. The differences in the local packing, the mesoscale organization and the formation of the gels due to change of the repulsion strength with respect to the attraction influence the shear moduli. S1 displays an elastic response at lower volume fractions with respect to S2. This can be related to the presence of a spanning network structure in S1. From the inset of Fig. 3.6, we can see that the particles in S1 have lower coordination numbers, for the same volume fraction, i.e. they tend to form open structures that result in a gel at lower ϕ.

The changes in the gel morphology when it is formed under precipitation of the hydrates (see Section 3.4), induce changes in the mechanical properties at these early stages of cement hydration. The shear moduli of gels obtained in S1 and S2 with different kinetic rates R and at fixed volume fractions are plotted as a function of ϕ in Fig. 5.4 (respectively top and bottom panel). If we consider that $\sigma \simeq 10nm$ at room temperature $T = 298K$ we obtain elastic moduli ranging up to $\simeq 10^6 Pa$, which are reasonable values for C–S–H gels in the early stages of hydration [11, 13]. In both cases, one can see from the insets of Fig. 3.6 that the $\phi-$dependence of the average coordination number cannot account alone for the volume fraction dependence of the gel moduli, indicating that the mesoscale organization of the network plays an important role for the gel strength over the whole range of volume fractions investigated here. The data for S1 indicate that the gels formed upon precipitation start to display a finite modulus at slightly lower volume fraction, confirming that precipitation does favor branching and percolation of the elongated growing aggregates. Overall the dependence on R of the modulus is very weak, basically negligible, although one might argue that there is a slight trend in the deceleration regime (i.e. $\phi > 0.15$): the faster the precipitation, the lower the modulus. This is consistent with the finding that precipitation favors defects and less well locally packed structures, as also indicated in the inset of Fig. 3.6 and shown in the snapshots in Fig. 3.10.

In the case of S2 (Fig. 5.4, lower panel), i.e. upon increasing the lime concentration, we find that the effect of the kinetic rate R is somewhat stronger. The gels formed upon precipitation have a finite modulus at significantly lower volume fractions, well before the deceleration regime starts. Within this range of volume fractions, the modulus displays a significant variation upon changing R. In this case at low volume fractions the gels formed upon precipitation have clearly better mechanical properties, whereas, once deceleration sets in (i.e., at

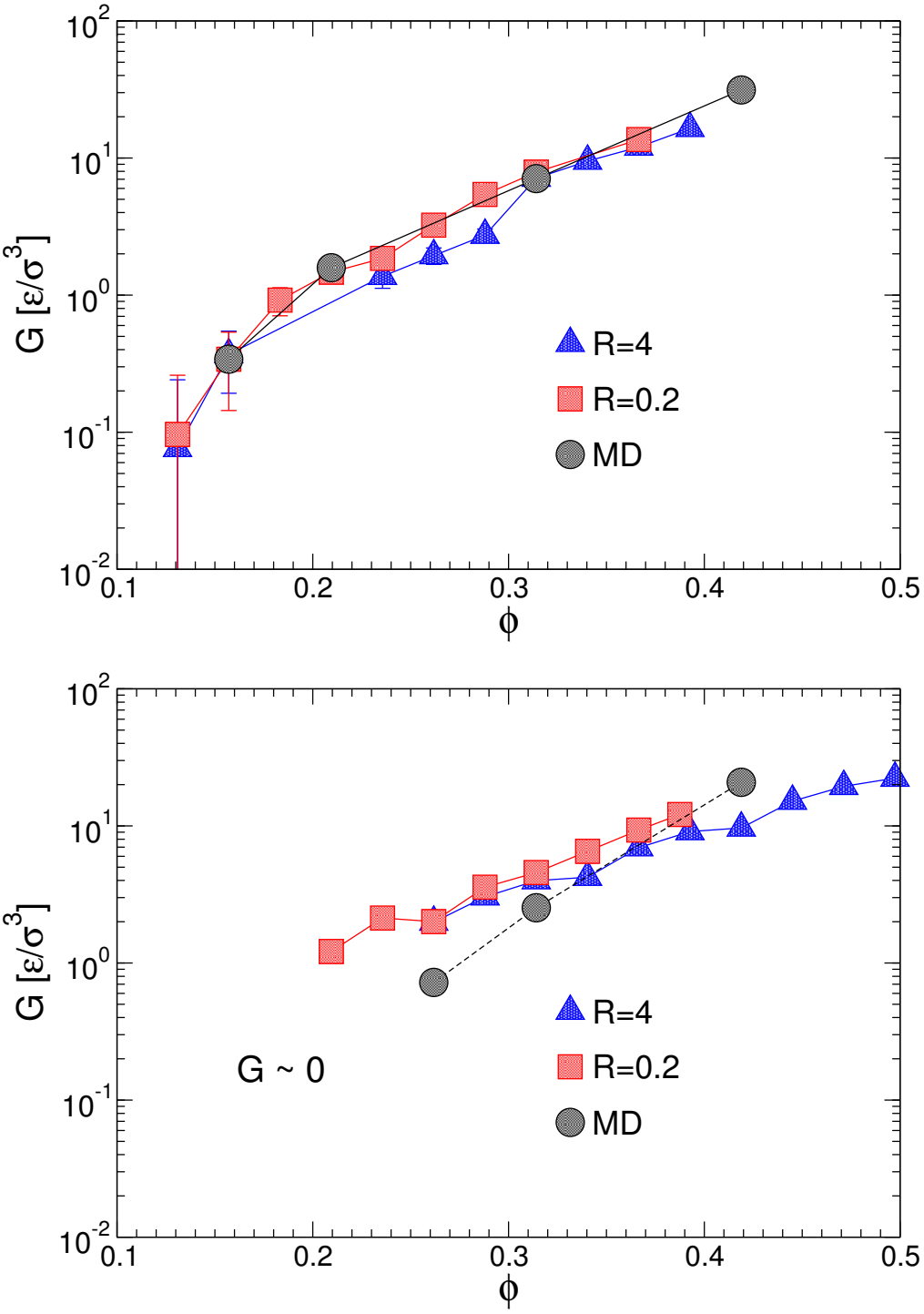

Fig. 5.4 Shear modulus as function of the volume fraction for S1 (top) and S2 (bottom). G^{S1}_{MD} for $\phi < 0.15$, G^{S2}_{MD} for $\phi < 0.25$, $G^{S2}_{R=4}$ for $\phi < 0.25$ and $G^{S2}_{R=0.2}$ for $\phi < 0.2$ are not detectable.

$\phi \leq 0.3$) they tend to be comparatively weaker upon increasing ϕ. This suggests that at low ϕ the mechanical properties are controlled by the percolation of the gel structure that is actually favored through precipitation, whereas the large amounts of defects in the local packing produced in the precipitation leads to mechanically weaker gels at later stages of the densification. These results cannot be compared with experiments, as already explained. Nevertheless, the results just discussed may give new interesting indications on how to control the mechanics of C–S–H gels via their microstructure when exploring different chemical composition that may change the effective interactions.

We have also investigated the evolution of the shear modulus with time for S1 and S2 (for a high and low kinetic rate). In Fig. 5.5 we plot the shear modulus vs the simulation time (in reduced units) in the lower x-axis and vs the real time computed using the argument in Section 3.3 and used for the comparison with hydration experiments (upper x-axis). We also plot the experimental data of Ref. [11] of the evolution of the shear modulus during hydration. The right y-axis corresponds to the range of the experimental shear modulus. As we mentioned before for $\sigma \simeq 10nm$ and room temperature $T = 298K$ we obtain elastic moduli ranging up to $\simeq 10^6 Pa$, which is three orders of magnitude lower than the experimental ones. We should notice again that we attempt to compare the simulated modulus that refers to samples of few hundred nm to macroscopic experimental data. Nevertheless, we can see that our data in terms of time (x-axis) roughly correspond to the second increase of the experimental $G(t)$ after the plateau around $10^7 Pa$. This is a very encouraging result because it is known that the first plateau of the experimental curve of Fig. 5.5 is mainly due to the cohesion of the unhydrated clinker whereas the second increase is expected to be mainly due to C–S–H. We note that y-axis are arbitrarily rescaled as the modulus computed from the simulations is much weaker than the one measured in the experiments. This discrepancy could be justified by considering that the simulations give an estimate of the contribution of the C–S–H gel without the underlying network of unhydrated clinker particles. We notice that for both potentials the evolution of the modulus with time has qualitatively the same behavior as the experimental curve. In particular in the case of S1 the modulus increases over two orders of magnitudes.

5.4.2 Nanoindentation

Nanoindentation experiments have been used in the last few years to measure locally the mechanical properties of the C–S–H gel in cement. The experiments probe the stiffness and hardness of C–S–H at the micrometer scale. The indentation modulus is proportional to the stiffness at contact, i.e. the slope during the unloading of the load-penetration curve obtained from the indentation tests [115, 148]. From the indentation modulus M and stiffness H one can estimate local densities using the Self Consistent scheme (SCS) or the Mori-Tanaka scheme (MTS). These two schemes provide $M(\phi)$ and $H(\phi)$ relations, once the asymptotic maximum value of

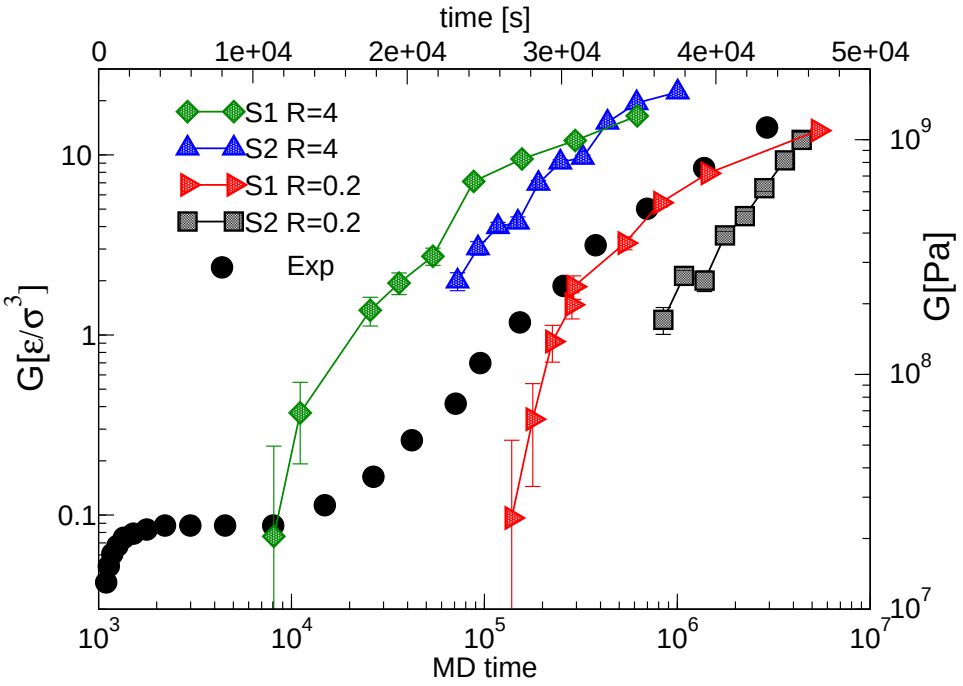

Fig. 5.5 Shear modulus as function of time for S1, S2 and a high and low kinetic rate R. The experimental data, depicted by black circles, are from Ref. [11] and were also discussed in Subsection 1.2.2

H and M at $\phi = 1$ are fixed. The SCS is based on a granular description of the material, predicting a linear $M(\phi)$ and zero M and H when $\phi < 0.5$. The MTS assumes instead that the material has a porous bicontinuous matrix and therefore M and H are zero only at $\phi = 0$ and in addition the dependence of M on ϕ is nonlinear.

Here, we computed the indentation moduli at rest after all the stresses of the configurations are relaxed to zero using the isostress ensemble and energy minimization. In Fig. 5.6 we plot the indentation moduli computed for our gel configurations as a function of their volume fractions and we compare them with the experimental measurements of M in hardened paste by instrumented nanoindentation [43]. For comparison we convert the indentation moduli M of the simulated configurations to real units of mature C–S–H, by using the unit pressure of $\epsilon/\sigma^3 = 0.148$ [149], whereas the interaction strength used in our simulations refer to C–S–H at very early stages and are much weaker compared to those of mature C–S–H. Here the comparison only tells us which would be the indentation modulus of the C–S–H gel if its structure would not be further densified in the later stages of hydration. The black triangles (Sim 1) correspond to the results of our simulations and the blue squares to experimental results on white cement paste of Ref. [43]. The volume fraction ϕ of the experimental indentation moduli M was calculated using the SCS. The predictions of the SCS and MTS are also shown in red solid and black dashed lines respectively. We also included in the

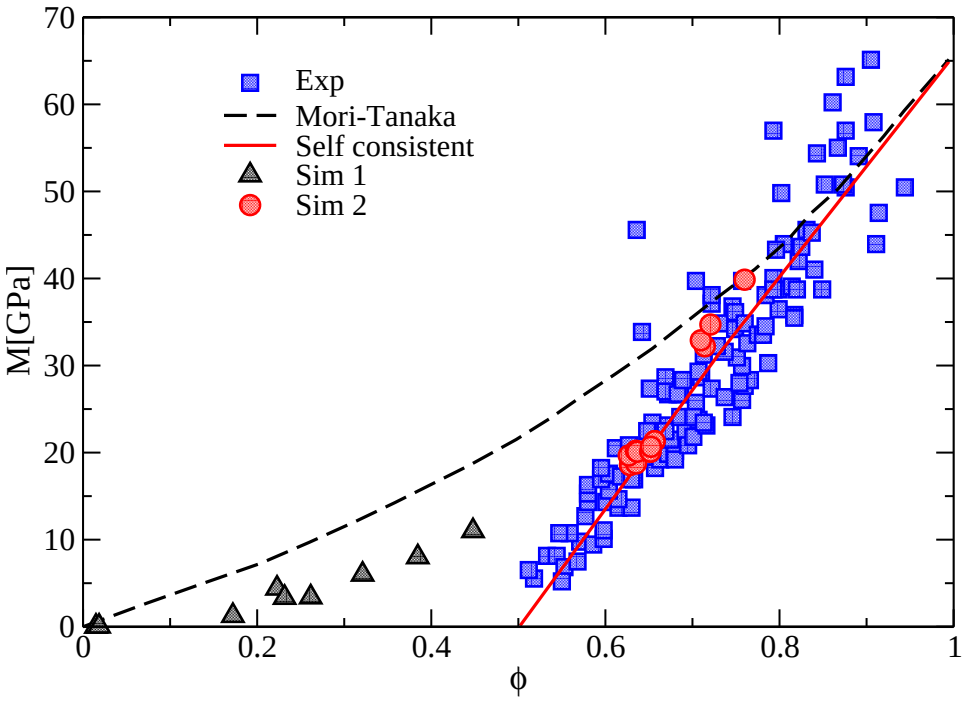

Fig. 5.6 Indentation modulus M as function of volume fraction ϕ. Experimental results on white cement paste of Ref. [43] are shown in blue squares. Their volume fraction ϕ was calculated using the SCS. The predictions of the SCS and MTS are shown in red solid and black dashed lines respectively. Results of our C–S–H gel configurations (Sim 1) are shown in black triangles and show agreement with the MTS. Simulation results of Ref. [149] (Sim 2) are shown with red circles.

figure the simulation results (red circles) of a nanoscale colloidal model for C–S–H in the hardened paste that used a space filling algorithm for polydisperse particles to obtain dense structures of C–S–H gels, with volume fraction $\phi > 0.6$ [114]. The nanoparticles considered in that study were spherical and polydisperse in size and interacted via a generalized LJ potential. The final volume fraction depends in this case only on the size polydispersity. The results of our simulations that correspond to $\phi < 0.5$ and to early hydration stages seem to follow the MTS prediction for the experimental data with a percolation threshold (obtained by imposing $M = 0$) around $\phi = 0.15$. For $\phi > 0.5$, the experimental results are well consistent with the results of Masoero et al. [149] (Sim 2). The comparison with our rescaled data suggests that the presence of parts of the structure where larger pores are still present and the densification did not proceed further might lead to a stronger dependence of M on ϕ, close to the one predicted by the MTS.

5.5 Conclusions

Although a direct, quantitative comparison between the results of our simulations and experiments is not straight forward and for many aspects not possible, in this last chapter we attempted a discussion in this direction. The structure of the C–S–H gels obtained from the simulations captures features reported in the experimental observations of cement paste like the pore size distribution and the SANS intensity. In terms of mechanical properties, the gels obtained in the simulations can capture the time evolution of the elastic modulus during the early stages of hydration, however the comparison with the mechanical properties in the hardened paste is not possible as suggested by the comparison with the nanoindentation experiments. Despite the limitations of our model (e.g. the use of monodisperse, spherical particles nanoscale units or of constant interaction strengths throughout the hydration), the fact that such a minimal model can reproduce qualitatively and in some cases even quantitatively the structure and mechanics of real cement is remarkable. Apart from the particle interaction, that have been motivated by experimental measurements of Ref. [45], our model does not contain any pre-imposed structure, but gel formation is the result of the interplay between the free energy minimization and the non-equilibrium environmental conditions. The results presented here and in Chapter 3 support the idea that we are able to capture a few fundamental physical mechanisms that govern the formation of C–S–H gels during cement hydration.

Concluding remarks and outlook

In this work we have dealt with the problem of the formation and evolution of C–S–H microstructure, the main binding phase of cement, at the level of few hundreds nm. A source of complexity in cement, and more specifically in C–S–H, is that the structure is amorphous and develops over several length scales under out-of-equilibrium conditions. This issue has major implications in the mechanical properties of cement and hence in the stability and durability of buildings. In order to tackle this complexity we have proposed a simple coarse-grained nanoscale model and computation approach for the C–S–H gel formation during the early stages of cement hydration. The use of a coarse-grained model makes this investigation possible by reducing the degrees of freedom of the system and maintaining only the minimal essential constituents. The main characteristics of our model are: it consists of particles of few nm representing the main units of the C–S–H gel, the particles interact with effective forces arising from atomistic interactions, the formation and evolution of the gel microstructure is determined by the combination of Statistical Mechanics laws with the out-of-equilibrium conditions stemming from the complex chemical hydration reactions. This type of model can provide the time evolution of the C–S–H gel microstructure which can be analyzed and used for computing directly its mechanical properties.

We have investigated the densification of C–S–H gels under particle precipitation. During cement hydration new C–S–H units (particles) are produced, due to the ongoing reactions, they interact with the existing ones, stick together and form aggregates that eventually create a stress-bearing network, a gel. We have used a grand-canonical Monte Carlo scheme together with Molecular Dynamics to account for the particle precipitation, the dynamics of the formed structures and the out-of-equilibrium conditions. The first result is the time evolution of the C–S–H gel densification which displays the same features as the experiments: an initial accelerating regime followed by a decelerating one. Using a time rescaling argument, a real time scale could be assigned to the simulated time evolution of the gels. The structural analysis of the C–S–H gels formed under precipitation showed that the different densification regimes can be directly related to the aggregation process that is controlled by the underlying thermodynamics. The local packing of the aggregates changes upon increasing the density such that when the system is dilute there are large elongated clusters which quickly form a gel, whereas when

the system is dense compact crystalline domains are formed. Furthermore tuning the out-of-equilibrium conditions changes the time evolution of the C–S–H gels and the degree of order in the system. This approach allowed to clarify the connection between hydration kinetics and changes in C–S–H gel morphology.

We have also explored further the influence of the underlying thermodynamics in the formation of the precipitated C–S–H gels by computing the phase diagrams corresponding to the effective interactions. The typical interactions in C–S–H are characterized by short-range attraction and long-range repulsion and the specific form depends on the chemical conditions. The results of this study suggest that varying the repulsion strength with respect to attraction changes both the equilibrium phases and the metastable states, influences the local packing, the mesoscale organization and the gelation. Few features of the equilibrium phases and metastable states persist even in the out-of-equilibrium conditions of precipitation and play a significant role in determining the properties of C–S–H gels. These findings have also implications on the mechanical properties of the C–S–H gels, e.g. the onset of rigidity of the precipitated gels occurs at low density. Furthermore, we could compare qualitatively and in some cases quantitatively our results with the experimental findings on the pore size distribution, the SANS intensity and the evolution of the elastic modulus during hydration. The results suggest that our approach and minimal model for C–S–H gels are able to capture many features reported in the experimental observations of real cement paste.

The results discussed in this manuscript have risen several new questions and possible research directions to investigate in future work. Effective interactions play a major role in our approach, hence we will explore two possible modifications. The first, which we have already started to investigate, is the effect of higher attraction strength, as suggested by a more quantitative tuning with different experimental results. We expect that this could account for the discrepancy of the moduli and help to achieve a better quantitative agreement with the experiments. The second is based on the fact that in cement formed under environmental conditions the chemical modifications vary with time, therefore varying the effective interaction during precipitation could result in even more realistic C–S–H microstructure. Another aspect is the shape of the C-S-H nanoscale units that, according to experiments, are platelet-like, whereas in our simulations are spherical. In future investigation we would like to study the effect of particle anisotropy on the local packing and mesoscale organization of C–S–H gels. Finally, a possible improvement towards more realistic C–S–H structures may arise by considering a preferentially initial surface of C–S–H in the simulation box where nucleation of C–S–H occurs. This idea is suggested by several experimental observations and we would like to explore how the preferred nucleation on the surface could affect kinetics and gel morphology.

References

[1] P. Barnes and J. Bensted. *Structure and Performance of Cements*. Spon Press, 2002.

[2] H. Taylor. *Cement Chemistry*. Thomas Telford Publishing, 1997.

[3] K. L. Scrivener and A. Nonat. Hydration of cementitious materials, present and future. *Cement and Concrete Research*, 41(7):651–665, 2011.

[4] J. W. Bullard, H. M. Jennings, R. A. Livingston, A. Nonat, G. W. Scherer, J. S. Schweitzer, K. L. Scrivener, and J. J. Thomas. Mechanisms of cement hydration. *Cement and Concrete Research*, 41(12):1208–1223, 2011.

[5] L. Nicoleau, A. Nonat, and D. Perrey. The di- and tricalcium silicate dissolutions. *Cement and Concrete Research*, 47:14–30, 2013.

[6] L. Nicoleau. New Calcium Silicate Hydrate Network. *Transportation Research Record: Journal of the Transportation Research Board*, 2142:42–51, 2010.

[7] J. J. Thomas, H. M. Jennings, and J. J. Chen. Influence of Nucleation Seeding on the Hydration Mechanisms of Tricalcium Silicate and Cement. *Journal of Physical Chemistry C*, 113(11):4327–4334, 2009.

[8] K. Mori, T. Sato, T. Fukunaga, K. Oishi, K. Kimura, K. Iwase, M. Sugiyama, K. Itoh, F. Shikanai, T. Wuernisha, M. Yonemura, D. Sulistyanintyas, I. Tsukushi, S. Takata, T. Otomo, T. Kamiyma, and M. Kawai. Observation of microstructure of hydrated Ca3SiO5. *Physica B: Condensed Matter*, 385-386:517–519, 2006.

[9] J. J. Thomas, J. J. Biernacki, J. W. Bullard, S. Bishnoi, J. S. Dolado, G. W. Scherer, and A. Luttge. Modeling and simulation of cement hydration kinetics and microstructure development. *Cement and Concrete Research*, 41(12):1257–1278, 2011.

[10] S. Garrault, E. Finot, E. Lesniewska, and A. Nonat. Study of C-S-H growth on C3S surface during its early hydration. *Materials and Structures*, 38(4):435–442, 2005.

[11] D. Lootens, P. Hébraud, E. Lécolier, and H. Van Damme. Coagulation, rhéofluidification et rhéoépaississement dans les coulis de ciment. *Oil Gas Science and Technology*, 59(1):31–40, 2004.

[12] A. Nonat. Du gâchage à l'état durci, ce sont les mêmes liaisons qui sont à l'œuvre. *Revue Française de Génie Civil*, 2(7):759–765, 1998.

[13] L. Nachbaur, J. C. Mutin, A. Nonat, and L. Choplin. Dynamic mode rheology of cement and tricalcium silicate pastes from mixing to setting. *Cement and Concrete Research*, 31(2):183–192, 2001.

[14] J. W. Bullard and R. J. Flatt. New insights into the effect of calcium hydroxide precipitation on the kinetics of tricalcium silicate hydration. *Journal of the American Ceramic Society*, 93:1894–1903, 2010.

[15] I. G. Richardson. The nature of C-S-H in hardened cements. *Cement and Concrete Research*, 29:1131–1147, 1999.

[16] E. Henderson and J. E. Bailey. The compositional and molecular character of the calcium silicate hydrates formed in the paste hydration of 3CaOSiO2. *Journal of Materials Science*, 28(13):3681–3691, 1993.

[17] P. C. Fonseca and H. M. Jennings. The effect of drying on early-age morphology of C–S–H as observed in environmental sem. *Cement and Concrete Research*, 40(12):1673–1680, 2010.

[18] A. Baronnet. Conference presentation in "Microstructure, setting and aging of cement. From soft matter physics to sustainable materials", Monte Verita August 2012.

[19] P. Levitz, J.P. Korb, and D. Petit. Slow dynamics of embedded fluid in mesoscopic confining systems as probed by nmr relaxometry. *The European Physical Journal E*, 12(1):29–33, 2003.

[20] J. P. Korb, L. Monteilhet, P. J. McDonald, and J. Mitchell. Microstructure and texture of hydrated cement-based materials: A proton field cycling relaxometry approach. *Cement and Concrete Research*, 37(3):295–302, 2007.

[21] P. J. McDonald, V. Rodin, and A. Valori. Characterisation of intra- and inter-C–S–H gel pore water in white cement based on an analysis of NMR signal amplitudes as a function of water content. *Cement and Concrete Research*, 40(12):1656–1663, 2010.

[22] A. C. A. Muller, K. L. Scrivener, A. M. Gajewicz, and P. J. McDonald. Densification of C–S–H measured by 1h nmr relaxometry. *Journal of Physical Chemistry C*, 117(1):403–412, 2013.

[23] H. Chemmi, D. Petit, P. Levitz, and J. P. Korb. NMR control of aging and durability of hardened cement pastes. *Comptes Rendus Chimie*, 13(4):405 – 408, 2010.

[24] J. B. d'Espinose, F. Barberon, B. Bresson, P. Fonollosa, H. Zanni, V. E. Fedorov, N. G. Naumov, and Z. Gan. Applicability of natural abundance 33s solid-state NMR to cement chemistry. *Cement and Concrete Research*, 36(9):1781 – 1783, 2006.

[25] R. F. Feldman and P. J. Sereda. A model for hydrated portland cement paste as deduced from sorption-length change and mechanical properties. *Matériaux et Construction*, 1(6):509–520, 1968.

[26] M. Daimon, S. A. Abo-Ee-Enein, G. Rosara, S. Goto, and R. Kondo. Pore structure of calcium silicate hydrate in hydrated tricalcium silicate. *Journal of the American Ceramic Society*, 60(3-4):110–114, 1977.

[27] E. M. Gartner. A proposed mechanism for the growth of C–S–H during the hydration of tricalcium silicate. *Cement and Concrete Research*, 27:665–672, 1997.

[28] T. C. Powers. Structure and physical properties of hardened portland cement paste. *Journal of the American Ceramic Society*, 41(1):1–6, 1958.

[29] A. J. Allen, R. C. Oberthur, D. Pearson, P. Schofield, and C. R. Wilding. Development of the fine porosity and gel structure of hydrating cement systems. *Philosophical Magazine Part B*, 56(3):263–288, 1987.

[30] J. J. Thomas and H. M. Jennings. A colloidal interpretation of chemical aging of the C-S-H gel and its effects on the properties of cement paste. *Cement and Concrete Research*, 36(1):30–38, 2006.

[31] H. M. Jennings. Refinements to colloid model of C-S-H in cement: CM-II. *Cement and Concrete Research*, 38(3):275–289, 2008.

[32] A. Nonat. The structure and stoichiometry of C-S-H. *Cement and Concrete Research*, 34(9):1521–1528, 2004.

[33] S. Lesko, E. Lesniewska, A. Nonat, J. C. Mutin, and J. P. Goudonnet. Investigation by atomic force microscopy of forces at the origin of cement cohesion. *Ultramicroscopy*, 86(1-2):11–21, 2001.

[34] W.-S. Chiang, E. Fratini, P. Baglioni, D. Liu, and S.-H. Chen. Microstructure determination of calcium-silicate-hydrate globules by small-angle neutron scattering. *Journal of Physical Chemistry C*, 116(8):5055–5061, 2012.

[35] F. Ridi, E. Fratini, and P. Baglioni. Cement: a two thousand year old nano-colloid. *Journal of Colloid and Interface Science*, 357(2):255–264, 2011.

[36] J. D. Bernal. The structures of cement hydration compounds. *Proceedings of the 3rd International Symposium on the Chemistry of Cement*, pages 216–36, 1954.

[37] H. F. W. Taylor. Nanostructure of C-S-H: Current status. *Advanced Cement Based Materials*, 1(1):38–46, 1993.

[38] E. Bonaccorsi, S. Merlino, and A. R. Kampf. The Crystal Structure of Tobermorite 14 Å (Plombierite), a C–S–H Phase. *Journal of the American Ceramic Society*, 88(3):505–512, 2005.

[39] X. Cong and R. J. Kirkpatrick. 29Si MAS NMR study of the structure of calcium silicate hydrate. *Advanced Cement Based Materials*, 3(3–4):144 – 156, 1996.

[40] H. F. W. Taylor. Proposed Structure for Calcium Silicate Hydrate Gel. *Journal of the American Ceramic Society*, 69(6):464–467, 1986.

[41] I. G. Richardson and G. W. Groves. Models for the composition and structure of calcium silicate hydrate (C-S-H) gel in hardened tricalcium silicate pastes. *Cement and Concrete Research*, 22:1001–1010, 1992.

[42] A. J. Allen, J. J. Thomas, and H. M. Jennings. Composition and density of nanoscale calcium-silicate-hydrate in cement. *Nature Materials*, 6(4):311–6, 2007.

[43] R. J. M. Pellenq, A. Kushima, R. Shahsavari, K. J. Van Vliet, M. J. Buehler, S. Yip, and F. J. Ulm. A realistic molecular model of cement hydrates. *Proceedings of the National academy of Sciences of the United States of America*, 106(38):16102–7, 2009.

[44] S. Garrault, T. Behr, and A. Nonat. Formation of the C-S-H Layer during early hydration of tricalcium silicate grains with different sizes. *Journal of Physical Chemistry B*, 110(1):270–5, 2006.

[45] C. Plassard, E. Lesniewska, I. Pochard, and A. Nonat. Nanoscale Experimental Investigation of Particle Interactions at the Origin of the Cohesion of Cement. *Langmuir*, 21(16):7263–7270, 2005.

[46] J. N. Israelachvili. *Intermolecular and Surface Forces, Second Edition: With Applications to Colloidal and Biological Systems (Colloid Science)*. Academic Press, 1992.

[47] P. Attard. *Electrolytes and the Electric Double Layer*, pages 1–159. John Wiley & Sons, Inc., 2007.

[48] A. Gmira, M. Zabat, R. J. M. Pellenq, and H. Damme. Microscopic physical basis of the poromechanical behavior of cement-based materials. *Materials and Structures*, 37(1):3–14, 2004.

[49] R. J. M. Pellenq and H. Van Damme. Why does concrete set?: The nature of cohesion forces in hardened cement-based materials. *MRS Bulletin*, 29(5):319–323, 2004.

[50] R. J. M. Pellenq, N. Lequeux, and H. van Damme. Engineering the bonding scheme in C-S-H: The iono-covalent framework. *Cement and Concrete Research*, 38(2):159–174, 2008.

[51] S. V. Churakov. Structure of the interlayer in normal 11 angstrom tobermorite from an ab initio study. *European Journal of Mineralogy*, 21:261–271, 2009.

[52] H. Manzano, E. Masoero, I. Lopez-Arbeloa, and H. M. Jennings. Shear deformations in calcium silicate hydrates. *Soft Matter*, 9:7333–7341, 2013.

[53] B. Jönsson, H. Wennerström, A. Nonat, and B. Cabane. Onset of cohesion in cement paste. *Langmuir*, 20(16):6702–9, 2004.

[54] B. Jönsson, A. Nonat, C. Labbez, B. Cabane, and H. Wennerström. Controlling the cohesion of cement paste. *Langmuir*, 21(20):9211–21, 2005.

[55] I. Pochard, C. Labbez, A. Nonat, H. Vija, and B. Jönsson. Cement and Concrete Research The effect of polycations on early cement paste. *Cement and Concrete Research*, 40(10):1488–1494, 2010.

[56] R. Kondo and S. Ueda. Kinetics of hydration of cements. *Proceedings of the 5th international symposium on chemistry of cement, Tokyo*, pages 203–248, 1968.

[57] M. Avrami. Kinetics of phase change. I General theory. *Journal of Chemical Physics*, 7(12):1103–1112, 1939.

[58] P. W. l. Brown, J. Pommersheim, and G. Frohnsdorff. A kinetic model for the hydration of tricalcium silicate. *Cement and Concrete Research*, 15(1):35–41, 1985.

[59] H. M. Jennings and S. K. Johnson. Simulation of microstructure development during the hydration of a cement compound. *Journal of the American Ceramic Society*, 69(11):790–795, 1986.

[60] P. Meakin. Universality, nonuniversality, and the effects of anisotropy on diffusion-limited aggregation. *Physical Review Applied*, 33:3371–3382, 1986.

[61] D. P. Bentz. Three-dimensional computer simulation of portland cement hydration and microstructure development. *Journal of the American Ceramic Society*, 80(1):3–21, 1997.

[62] S. Bishnoi and K. L. Scrivener. Studying nucleation and growth kinetics of alite hydration using μic. *Cement and Concrete Research*, 39(10):849–860, 2009.

[63] E. J. Garboczi and D. P. Bentz. Computer simulation of the diffusivity of cement-based materials. *Journal of Materials Science*, 27(8):2083–2092, 1992.

[64] J. W. Bullard. Approximate rate constants for nonideal diffusion and their application in a stochastic model. *Journal of Physical Chemistry A*, 111(11):2084–2092, 2007.

[65] J. W. Bullard. A three-dimensional microstructural model of reactions and transport in aqueous mineral systems. *Modelling and Simulation in Materials Science and Engineering*, 15(7):711, 2007.

[66] L. Cipelletti and L. Ramos. Slow dynamics in glassy soft matter. *Journal of Physics: Condensed Matter*, 17(6):R253–R285, 2005.

[67] P. J Lu, E. Zaccarelli, F. Ciulla, A. B. Schofield, F. Sciortino, and D. A. Weitz. Gelation of particles with short-range attraction. *Nature*, 453(7194):499–503, 2008.

[68] V. Trappe, V. Prasad, L. Cipelletti, P. N. Segre, and D. A. Weitz. Jamming phase diagram for attractive particles. *Nature*, 411(6839):772–5, 2001.

[69] K. N. Pham, A. M. Puertas, J. Bergenholtz, S. U. Egelhaaf, A. Moussaid, P. N. Pusey, A. B. Schofield, M. E. Cates, M. Fuchs, and W. C. K. Poon. Multiple glassy states in a simple model system. *Science*, 296(5565):104–106, 2002.

[70] A. Zaccone, D. Gentili, H. Wu, M. Morbidelli, and E. Del Gado. Shear-Driven Solidification of Dilute Colloidal Suspensions. *Physical Review Letters*, 106(13):1–4, 2011.

[71] V. J. Anderson and H. N. W. Lekkerkerker. Insights into phase transition kinetics from colloid science. *Nature*, 416:811–815, 2002.

[72] N. A. M. Verhaegh, D. Asnaghi, H. N.W. Lekkerkerker, M. Giglio, and L. Cipelletti. Transient gelation by spinodal decomposition in colloid-polymer mixtures. *Physica A: Statistical Mechanics and its Applications*, 242(1–2):104–118, 1997.

[73] A. de Candia, E. Del Gado, A. Fierro, N. Sator, M. Tarzia, and A. Coniglio. Columnar and lamellar phases in attractive colloidal systems. *Physical Review E: Statistical, Nonlinear, and Soft Matter Physics*, 74:010403, 2006.

[74] A. Zaccone, H. Wu, and E. Del Gado. Elasticity of arrested short-ranged attractive colloids: Homogeneous and heterogeneous glasses. *Physical Review Letters*, 103:208301, 2009.

[75] P. N. Pusey and W. van Megen. Phase behaviour of concentrated suspensions of nearly hard colloidal spheres. *Nature*, 320:340–342, 1986.

[76] D. Frenkel and B. Smit. *Understanding Molecular Simulation: From Algorithms to Applications*. Computational Science. Elsevier Science, 2001.

[77] R. Larson. *The structure and rheology of complex fluids*. Oxford University Press, 1999.

[78] A. I. Campbell, V. J. Anderson, J. S. van Duijneveldt, and P. Bartlett. Dynamical arrest in attractive colloids: The effect of long-range repulsion. *Physical Review Letters*, 94:208301, 2005.

[79] J. W. Cahn and J. E. Hilliard. Free energy of a nonuniform system I. Interfacial free energy. *Journal of Chemical Physics*, 28:258–267, 1958.

[80] A. Fortini, E. Sanz, and M. Dijkstra. Crystallization and gelation in colloidal systems with short-ranged attractive interactions. *Physical Review E: Statistical, Nonlinear, and Soft Matter Physics*, 78:041402, 2008.

[81] T. Gibaud, A. Zaccone, E. Del Gado, V. Trappe, and P. Schurtenberger. Unexpected decoupling of stretching and bending modes in protein gels. *Physical Review Letters*, 110:058303, 2013.

[82] S. Mossa, F. Sciortino, P. Tartaglia, and E. Zaccarelli. Ground-state clusters for short-range attractive and long-range repulsive potentials. *Langmuir*, 20(24):10756–10763, 2004.

[83] M. Tarzia and A. Coniglio. Lamellar order, microphase structures, and glassy phase in a field theoretic model for charged colloids. *Physical Review E: Statistical, Nonlinear, and Soft Matter Physics*, 75(1):011410, 2007.

[84] A. de Candia, E. Del Gado, A. Fierro, N. Sator, M. Tarzia, and A. Coniglio. Columnar and lamellar phases in attractive colloidal systems. *Physical Review E: Statistical, Nonlinear, and Soft Matter Physics*, 74(1):1–4, 2006.

[85] D. A. Weitz and M. Oliveria. Fractal structures formed by kinetic aggregation of aqueous gold colloids. *Physical Review Letters*, 52:1433–1436, 1984.

[86] P. Meakin. Fractal aggregates. *Advances in Colloid and Interface Science*, 28(0):249 – 331, 1987.

[87] D. A. Weitz, J. S. Huang, M. Y. Lin, and J. Sung. Limits of the fractal dimension for irreversible kinetic aggregation of gold colloids. *Physical Review Letters*, 54:1416–1419, 1985.

[88] A. Liu and S. R. Nagel. Jamming is not just cool any more. *Nature*, 396:21–22, 1958.

[89] S. Alexander. Amorphous solids: their structure, lattice dynamics and elasticity. *Physics Reports*, 296:65–236, 1998.

[90] I.G. Richardson. The calcium silicate hydrates. *Cement and Concrete Research*, 38(2):137–158, 2008.

[91] J. J. Thomas and H. M. Jennings. A colloidal interpretation of chemical aging of the c-s-h gel and its effects on the properties of cement paste. *Cement and Concrete Research*, 36(1):30–38, 2006.

[92] R. J. Flatt, N. Roussel, and C. R. Cheeseman. Concrete: An eco material that needs to be improved. *Journal of the European Ceramic Society*, 32(11):2787–2798, 2012.

[93] K. Van Vliet, R. J. M. Pellenq, M. J. Buehler, J. C. Grossman, H. Jennings, F.-J. Ulm, and S. Yip. Set in stone? A perspective on the concrete sustainability challenge. *MRS Bulletin*, 37(4):395–402, 2012.

[94] H. M. Jennings. A model for the microstructure of calcium silicate hydrate in cement paste. *Cement and Concrete Research*, 30(1):101–116, 2000.

[95] L. B. Skinner, S. R. Chae, C. J. Benmore, H. R. Wenk, and P. J. M. Monteiro. Nanostructure of Calcium Silicate Hydrates in Cements. *Physical Review Letters*, 104(19):195502, 2010.

[96] S. Brisard, R. S. Chae, I. Bihannic, L. Michot, P. Guttmann, J. Thieme, G. Schneider, P. J. M. Monteiro, and P. Levitz. Morphological quantification of hierarchical geomaterials by X-ray nano-CT bridges the gap from nano to micro length scales. *American Mineralogist*, 97(2-3):480–483, 2012.

[97] I. G. Richardson. Tobermorite/jennite- and tobermorite/calcium hydroxide-based models for the structure of c-s-h: applicability to hardened pastes of tricalcium silicate, β-dicalcium silicate, portland cement, and blends of portland cement with blast-furnace slag, metakaolin, or silica fume. *Cement and Concrete Research*, 34(9):1733–1777, 2004.

[98] E. M. Gartner, K. E. Kurtis, and P. J. M. Monteiro. Proposed mechanism of C-S-H growth tested by soft X-ray microscopy. *Cement and Concrete Research*, 30:817–822, 2000.

[99] E. Gallucci, P. Mathur, and K. Scrivener. Microstructural development of early age hydration shells around cement grains. *Cement and Concrete Research*, 40(1):4–13, 2010.

[100] S. Bishnoi. Geometric limitations of nucleation and growth models: Revisiting the impingement assumption. *Cement and Concrete Research*, 46(0):30–40, 2013.

[101] H. Viallis-Terrisse, A. Nonat, and J. C. Petit. Zeta-Potential Study of Calcium Silicate Hydrates Interacting with Alkaline Cations. *Journal of Colloid and Interface Science*, 244(1):58–65, 2001.

[102] Y. S. Jho, R. Brewster, S. A. Safran, and P. A. Pincus. Long-range interaction between heterogeneously charged membranes. *Langmuir*, 27(8):4439–4446, 2011.

[103] M. J. Booth, A. C. Eaton, and A. D. J. Haymet. Electrolytes at charged interfaces: Integral equation theory for 2–2 and 1–1 model electrolytes. *Journal of Chemical Physics*, 103(1):417–431, 1995.

[104] S. Plimpton. Fast parallel algorithms for short-range molecular dynamics. *Journal of Computational Physics*, 117(1):1–19, 1995. see: http://lammps.sandia.gov/.

[105] P. J. Steinhardt, D. R. Nelson, and M. Ronchetti. Bond-orientational order in liquids and glasses. *Physical Review B: Condensed Matter*, 28:784–805, 1983.

[106] J. D. Bernal. The Bakerian Lecture, 1962. The structure of liquids. *Proceedings of the Royal Society A: Mathematical, Physical and Engineering Sciences*, 280(1382):299–322, 1964.

[107] A. J. Archer and N. B. Wilding. Phase behavior of a fluid with competing attractive and repulsive interactions. *Physical Review E: Statistical, Nonlinear, and Soft Matter Physics*, 76:031501, 2007.

[108] R. P. Sear, S. W. Chung, G. Markovich, W. M. Gelbart, and J. R. Heath. Spontaneous patterning of quantum dots at the air-water interface. *Physical Review E: Statistical, Nonlinear, and Soft Matter Physics*, 59:R6255–R6258, 1999.

[109] J. Groenewold and W. K. Kegel. Anomalously large equilibrium clusters of colloids. *Journal of Physical Chemistry B*, 105(47):11702–11709, 2001.

[110] F. Sciortino, P. Tartaglia, and E. Zaccarelli. One-Dimensional Cluster Growth and Branching Gels in Colloidal Systems with Short-Range Depletion Attraction and Screened Electrostatic Repulsion. *Journal of Physical Chemistry B*, 109(46):21942–21953, 2005.

[111] P. Charbonneau and D. R. Reichman. Systematic characterization of thermodynamic and dynamical phase behavior in systems with short-ranged attraction. *Physical Review E: Statistical, Nonlinear, and Soft Matter Physics*, 75:011507, 2007.

[112] D. Stauffer and A. Aharony. *Introduction to percolation theory*. Taylor and Francis, 1994.

[113] A. de Candia, E. Del Gado, A. Fierro, and A. Coniglio. Length scale dependence of the dynamical heterogeneities in colloidal gelation at low volume fraction. *Journal of Statistical Mechanics: Theory and Experiment*, 2009.

[114] E. Masoero, E. Del Gado, R. J. M. Pellenq, F. J. Ulm, and S. Yip. Nanostructure and nanomechanics of cement: Polydisperse colloidal packing. *Physical Review Letters*, 109:155503, 2012.

[115] M. Vandamme and F. J. Ulm. Nanogranular origin of concrete creep. *Proceedings of the National academy of Sciences of the United States of America*, 106(26):10552–10557, 2009.

[116] F. Sciortino, S. Mossa, E. Zaccarelli, and P. Tartaglia. Equilibrium Cluster Phases and Low-Density Arrested Disordered States: The Role of Short-Range Attraction and Long-Range Repulsion. *Physical Review Letters*, 93(5):5–8, 2004.

[117] M. Tarzia and A. Coniglio. Pattern Formation and Glassy Phase in the φ^4 Theory with a Screened Electrostatic Repulsion. *Physical Review Letters*, 96(7):075702, 2006.

[118] A. de Candia, E. Del Gado, A. Fierro, and A. Coniglio. Length scale dependence of the dynamical heterogeneities in colloidal gelation at low volume fraction. *Journal of Statistical Mechanics: Theory and Experiment*, 2009(02):P02052, 2009.

[119] G. A. Vliegenthart, J. F. M. Lodge, and H. N. W. Lekkerkerker. Strong weak and metastable liquids structural and dynamical aspects of the liquid state. *Physica A: Statistical Mechanics and its Applications*, 263(1–4):378–388, 1999.

[120] D. J. Earl and M. W. Deem. Parallel tempering: Theory, applications, and new perspectives. *Physical Chemistry Chemical Physics*, 7:3910–3916, 2005.

[121] N. Rathore, M. Chopra, and J. J. de Pablo. Optimal allocation of replicas in parallel tempering simulations. *Journal of Chemical Physics*, 122:024111, 2005.

[122] D. Frenkel and A. J. C. Ladd. New Monte Carlo method to compute the free energy of arbitrary solids. Application to the fcc and hcp phases of hard spheres. *Journal of Chemical Physics*, 81(7):3188, 1984.

[123] C. Vega, E. Sanz, J. L. F. Abascal, and E. G. Noya. Determination of phase diagrams via computer simulation: methodology and applications to

water, electrolytes and proteins. *Journal of Physics: Condensed Matter*, 20(15):153101, 2008.

[124] J. L. Aragones, C. Valeriani, and C. Vega. Free energy calculations for atomic solids through the einstein crystal/molecule methodology using gromacs and lammps. *The Journal of Chemical Physics*, 137(14):146101, 2012.

[125] B. Widom. Some topics in the theory of fluids. *Journal of Chemical Physics*, 39:2808–2812, 1963.

[126] R. Pool and P. G. Bolhuis. Accurate free energies of micelle formation. *Journal of Physical Chemistry B*, 109(14):6650–6657, 2005. PMID: 16851747.

[127] D. J. Kraft, R. Ni, F. Smallenburg, M. Hermes, K. Yoon, D. A. Weitz, A. van Blaaderen, J. Groenewold, M. Dijkstra, and W. K. Kegel. Surface roughness directed self-assembly of patchy particles into colloidal micelles. *Proceedings of the National academy of Sciences of the United States of America*, 109(27):10787–10792, 2012.

[128] S. Brazovskii. Phase transition of an isotropic system to a nonuniform state. *Journal of Experimental and Theoretical Physics*, 41:85, 1975.

[129] A. Ciach, J. Pekalski, and W. T. Gozdz. Origin of similarity of phase diagrams in amphiphilic and colloidal systems with competing interactions. *Soft Matter*, 9:6301–6308, 2013.

[130] J. C. F. Toledano, F. Sciortino, and E. Zaccarelli. Colloidal systems with competing interactions: from an arrested repulsive cluster phase to a gel. *Soft Matter*, 5:2390–2398, 2009.

[131] G. Brambilla, S. Buzzaccaro, R. Piazza, L. Berthier, and L. Cipelletti. Highly nonlinear dynamics in a slowly sedimenting colloidal gel. *Physical Review Letters*, 106:118302, 2011.

[132] S. Maccarrone, G. Brambilla, O. Pravaz, A. Duri, M. Ciccotti, J. M. Fromental, E. Pashkovski, A. Lips, D. Sessoms, V. Trappe, and L. Cipelletti. Ultra-long range correlations of the dynamics of jammed soft matter. *Soft Matter*, 6(21):5514–5522, 2010.

[133] S.A. Safran. *Statistical Thermodynamics of Surfaces, Interfaces, and Membranes*. Frontiers in physics. Addison-Wesley Pub., 1994.

[134] E. Sanz, C. Valeriani, D. Frenkel, and M. Dijkstra. Evidence for out-of-equilibrium crystal nucleation in suspensions of oppositely charged colloids. *Physical Review Letters*, 99(5):055501, 2007.

[135] W. P. Halperin, J. Y. Jehng, and Y. Q. Song. Application of spin-spin relaxation to measurement of surface area and pore size distributions in a hydrating cement paste. *Magnetic Resonance Imaging*, 12(2):169–173, 1994.

[136] S. Bhattacharya and K. E. Gubbins. Fast method for computing pore size distributions of model materials. *Langmuir*, 22(18):7726–7731, 2006.

[137] F. Kappel and A. V. Kuntsevich. An implementation of shor's r-algorithm. *Computational Optimization and Applications*, 15(2):193–205, 2000.

[138] J.P. Hansen and I.R. McDonald. *Theory of Simple Liquids: with Applications to Soft Matter*. Elsevier Science, 2013.

[139] G. Porod. Die roentgenkleinwinkelstreuung von dichtgepackten kolloiden systemen. *Kolloid-Zeitschrift*, 1951.

[140] S. Brisard and P. Levitz. Small-angle scattering of dense, polydisperse granular porous media: computation free of size effects. *Physical Review E: Statistical, Nonlinear, and Soft Matter Physics*, 87(1):013305, 2013.

[141] P. Levitz. personal communication.

[142] M. Bellotto. Cement paste prior to setting: A rheological approach. *Cement and Concrete Research*, 52(0):161 – 168, 2013.

[143] D. J. Evans and G. P. Morriss. *Statistical Mechanics of Nonequilibrium Liquids*. ANU E Press, 2007.

[144] L. D. Landau and E. M. Lifshitz. *Theory of Elasticity*. Pergamon Presss, 1970.

[145] J. F. Lutsko. Generalized expressions for the calculation of elastic constants by computer simulation. *Journal of Applied Physics*, 65(8):2991–2997, 1989.

[146] R. Najafababi and S. Yip. Observation of finite-temperature bain transformation (fcc→< i> r</i> bcc) in monte carlo simulation of iron. *Scripta Metallurgica*, 17:1199–1204, 1983.

[147] T. Hill. *Statistical Mechanics*. McGraw-Hill, 1956.

[148] G. Constantinides and F. J. Ulm. The nanogranular nature of C–S–H. *Journal of the Mechanics and Physics of Solids*, 55(1):64–90, 2007.

[149] E. Masoero, E. Del Gado, R. J. M. Pellenq, S. Yip, and F. J. Ulm. Nano-scale mechanics of colloidal C-S-H gels. *Soft Matter*, 10:491–499, 2014.